Topologically-Protected Soliton States in Rhombohedrally-Stacked Graphite

James Muten

This thesis is submitted for the degree of

Doctor of Philosophy at Lancaster University

Lancaster University

The Department of Physics

Lancaster University

United Kingdom

August, 2024

Topologically-Protected Soliton States in Rhombohedrally-Stacked Graphite

James Muten

Abstract

We investigate the low-energy electronic properties of rhombohedrally-stacked graphite (RG). Chapter 1 discusses the history of graphene and provides the context for our work. In Chapter 2 we introduce the tight-binding model and demonstrate its application in describing the Hamiltonians and electronic band structures of several graphitic systems. We also present three one-dimensional models describing topological insulators, and show, through dimensional reduction, that these are similar to the graphene systems under investigation. Chapters 3 and 4 describe the original research work in the thesis. Chapter 3 describes stacking faults in thin films of RG. We find that each stacking fault produces two localised low-energy states near the Dirac points. In comparison to the one-dimensional models, such faults are effectively a soliton-antisoliton pair, and it is impossible to realise a single, isolated state on a stacking fault in RG. In Chapter 4 we consider rhombohedrally-stacked systems with alternating onsite energies, and, particularly, the properties of solitons consisting of a change in texture of the onsite energies. We show that, depending on parameter values, a single localised energy band may be isolated within the bulk band gap, in contrast to stacking faults in RG. For both types of faults, in Chapters 3 and 4, we derive low-energy effective Hamiltonians to describe hybridisation of the localised soliton states with localised surface states, and we model the robustness of the properties of these states in the presence of disorder.

Declaration

This thesis describes work carried out between October 2019 and October 2023 in the Condensed Matter Theory Group at the Department of Physics, Lancaster University under the supervision of Prof. E. McCann. The following sections of this thesis are included in work that has been published or accepted to be published:

Chapter 3: J. H. Muten, A. J. Copeland, and E. McCann. "Exchange interaction, disorder, and stacking faults in rhombohedral graphene multilayers". In: *Phys. Rev. B* 104 (3 July 2021), p. 035404

Chapter 4: J. H. Muten, L. H. Frankland, and E. McCann. "Solitons in binary compounds with stacked two-dimensional honeycomb lattices". In: (2023). arXiv: `2312.16949 [cond-mat.mes-hall]`. (accepted Phys. Rev. B)

I declare that this thesis is my own work, and has not been submitted in substantially the same form for the award of a higher degree elsewhere. This thesis does not exceed the word limit of 80000 words.

Acknowledgements

I am extremely grateful to my supervisor Edward McCann for sharing his knowledge and for all of his guidance and patience during my PhD, and would also like to thank the members of the Condensed Matter Theory group at Lancaster University for their many helpful discussions.

I would like to thank my wonderful wife, Beth, for her unending love and support, without which this work would not be possible. Thank you to my parents, Chris and Rose, who have always supported me, and my brother, Joe, for his constant encouragement.

Contents

Chapter 1

Introduction

Graphene is an atomically-thick layer of carbon atoms arranged on a honeycomb lattice [3], shown in figure 1.1. It was first isolated in 2004 by the Manchester University research group led by Andre Geim and Konstantin Novoselov [4], who were awarded the Nobel Prize in Physics 2010 "for groundbreaking experiments regarding the two-dimensional material graphene".

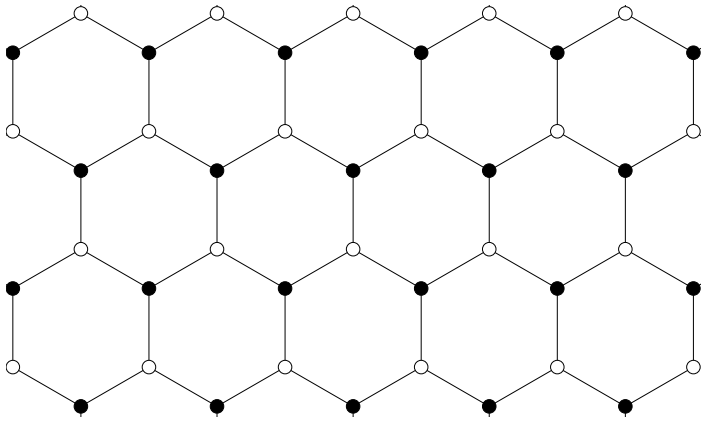

Figure 1.1: Diagram of the graphene honeycomb lattice. Circles represent atoms and lines represent σ bonds. Open and solid circles show atoms on the A and B sublattices, respectively.

Graphene found immediate research interest because it is stable at room temperature, an excellent electrical conductor, and it is easy to tune the carrier density with a back gate. The low-energy effective Hamiltonian of graphene resembles that of the Dirac equation, rather than the usual Schrödinger equation as found for conventional semiconductors.

Graphene was studied theoretically for many years before it was first fabricated

because of the need to build models to understand three-dimensional graphite. The electronic band structure of graphene was described by Wallace in 1947 [5], the Landau level spectrum by McClure in 1956 [6], and the model of graphene has been used as the building block of buckyballs [7] and carbon nanotubes [8]. The material graphite [9] is formed of many layers of graphene which are weakly-coupled together in the out-of-plane direction.

Graphene was initially produced by researchers at Manchester university [4] via mechanical exfoliation (also called the 'Scotch tape' or 'Sticky tape' method). This method can produce high quality samples, but is labour intensive and provides low yields.

Recent improvements in fabrication methods mean that very high-quality samples of ABC graphene can be produced [10–18], and, notably, researchers at Manchester university were able to fabricate up to 50 layers of rhombohedrally-stacked graphite in 2020 [19]. ABC graphene refers to the stacking configuration consisting of three different layer positions, as shown in figure 1.2.

Graphene possesses several interesting physical properties, all of which add to its research interest. It has an intrinsic strength of ~ 130 GPa [20], making it incredibly strong. Graphene is very resistant to compression in the in-plane direction, with a Young's modulus of ~ 1 TPa [20], but is flexible in the out-of-plane direction, with a bending stiffness of ~ 1 eV [21]. Graphene is an excellent electrical conductor, with high-quality samples upon a substrate demonstrating mobilities above $10^5\ \mathrm{cm^2\,V^{-1}\,s^{-1}}$ [22, 23], which means that ballistic transport may be supported for distances exceeding 1 µm at room temperature [24]. Graphene is also an excellent thermal conductor, with thermal conductivity up to $\sim 5000\ \mathrm{W\,m^{-1}\,K^{-1}}$ at room temperature [25].

The honeycomb lattice, figure 1.1, consists of two nonequivalent atomic positions, dubbed A and B. Multilayer graphene can generally form with one of three different stacking types: Bernal (ABA), Rhombohedral (ABC), or AA, these are

shown in figure 1.2. Bernal stacked graphene is the most commonly found stacking type as it is the most energetically favourable of the three. Rhombohedrally-stacked graphene is the next most commonly found stackng type, and AA graphene is far less commonly found, and generally only considered theoretically.

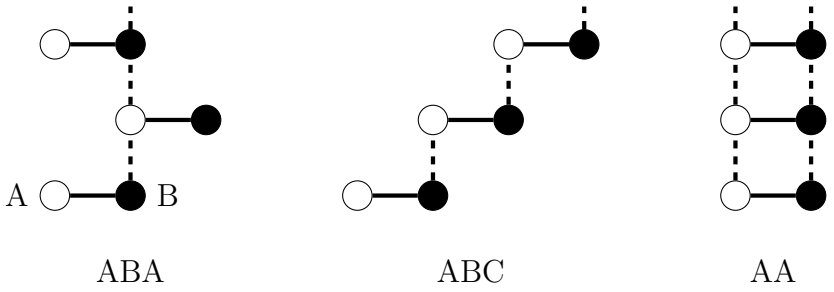

Figure 1.2: Schematic side view of the three graphene stacking types. Open and filled circles represent the atoms on the A and B sublattices, respectively, and each horizontal pair of A, B atoms represents a unit cell of monolayer graphene. Horizontal solid lines represent the intralayer coupling and vertical dashed lines represent the interlayer coupling.

In chapters 3 and 4 we will discuss isolated states that reside within the bulk band gap in graphene-like systems. These low-energy states are partly due to alternating the sign of the onsite potential, but it is not practical to induce this effect in pure graphene systems [2].

However, these results would apply to rhombohedrally-stacked compounds with a honeycomb lattice and consisting of two different atomic species, for example hexagonal boron nitride (h-BN) [26–31]. Boron phosphide [32–34] and silicon carbide [35–37] are two thin films with a honeycomb structure, and both have a direct band gap at the K point. Other similar materials include gallium nitride [38–41], zinc oxide [42–46], transition metal dichalcogenides [36, 47–51], and III-VI semiconductors [52–56]. We expect that these materials will support localised soliton states similar to those discussed in this thesis.

Chapter 2

Theoretical Background

2.1 General Tight-Binding Model in Two Dimensions

We consider a two-dimensional (2D) periodic lattice. A Bravais lattice is an infinite array, $\boldsymbol{R}$, of discrete points generated by primitive lattice vectors $\boldsymbol{a}_1$ and $\boldsymbol{a}_2$,

$$\boldsymbol{R} = m\boldsymbol{a}_1 + n\boldsymbol{a}_2, \tag{2.1.1}$$

where m and n are integers. There are five possible Bravais lattices in 2D [57], but more complicated crystal structures can be represented by the combination of a Bravais lattice and a basis - the arrangement of atomic orbitals surrounding each Bravais lattice point. The positions of the atoms with respect to the lattice point are denoted $\boldsymbol{\tau}_j$ where $j = 1, 2, \ldots$ indexes the different orbitals. The total position vector for each atom within the crystal is then given by $\boldsymbol{R}_j = \boldsymbol{R} + \boldsymbol{\tau}_j$.

A crystal lattice is spanned by tesselating areas called unit cells, and a primitive unit cell is a unit cell that contains only a single lattice point. Each primitive unit cell has the same shape and area, and the primitive unit cells together fully span the crystal lattice. A Wigner-Seitz cell is a type of primitive unit cell containing all points in space that are closer to a particular lattice point than to any other lattice point. This cell may be constucted by drawing the perpendicular bisectors of each lattice vector connecting a lattice point to all of its nearest neighbours. There are many possible choices of unit cell, but only one Wigner-Seitz cell may be found for

a given lattice. The area of the primitive unit cell is always $|\boldsymbol{a}_1 \times \boldsymbol{a}_2|$.

The reciprocal lattice exists in wave vector space (known as reciprocal space or k-space) and its primitive reciprocal lattice vectors $\boldsymbol{b}_1$ and $\boldsymbol{b}_2$ are related to the real (or direct) lattice via the relation

$$\boldsymbol{a}_i \cdot \boldsymbol{b}_j = 2\pi\delta_{i,j}, \tag{2.1.2}$$

where $\delta_{i,j}$ is the Kronecker delta

$$\delta_{i,j} = \begin{cases} 1, & \text{for } i = j \\ 0, & \text{for } i \neq j. \end{cases} \tag{2.1.3}$$

The reciprocal lattice is similarly defined by its primitive lattice vectors

$$\boldsymbol{G} = u\boldsymbol{b}_1 + v\boldsymbol{b}_2, \tag{2.1.4}$$

where u and v are integers. The Wigner-Seitz cell centred on the lattice point at $\boldsymbol{G} = 0$ is called the first Brillouin zone (BZ). The centre of the BZ is labelled $\boldsymbol{\Gamma}$ and points of high symmetry are labelled "$\boldsymbol{L}$", "$\boldsymbol{X}$", "$\boldsymbol{W}$", "$\boldsymbol{K}$", etc.

The placement of atomic sites on the crystal lattice leads to a periodic potential, which means that Bloch's theorem can be applied [57]. This states that energy eigenstates of a single-particle Hamiltonian can be found of the form

$$\Phi(\boldsymbol{r}) = e^{i\boldsymbol{q}\cdot\boldsymbol{r}} u(\boldsymbol{r}), \tag{2.1.5}$$

where u is a function with the same periodicity as the Bravais lattice $u(\boldsymbol{r} + \boldsymbol{R}) = u(\boldsymbol{r})$ and $\boldsymbol{q}$ is the wave vector describing different positions in reciprocal space, the primitive reciprocal lattice vectors $\boldsymbol{b}_1$ and $\boldsymbol{b}_2$ are written in the basis of (q_x, q_y), so $\boldsymbol{q} = 0$ describes the centre of the BZ, $\boldsymbol{G} = 0$, or the $\boldsymbol{\Gamma}$ point.

All physically distinct wave functions are labelled by $\boldsymbol{q}$ within the first BZ, and wave vectors outside of the BZ can always be described with the substitution $\boldsymbol{q}' = \boldsymbol{q} + \boldsymbol{G}$.

2.2 Tight-Binding Hamiltonian

In this section we will derive the tight-binding Hamiltonian [57–59] for a general lattice with two orbitals per unit cell, labelled A and B. This will apply for any number of spatial dimensions, but will be especially relevent for later discussions of the Su-Schreiffer-Heeger (SSH) model 2.6 and graphene 2.4.

The Hamiltonian H is written in terms of the atomic orbitals $|\boldsymbol{R}_A, A\rangle$ and $|\boldsymbol{R}_B, B\rangle$, where $\boldsymbol{R}_A = \boldsymbol{R} + \boldsymbol{\tau}_A$ denotes the position of the A atom in terms of the lattice vector $\boldsymbol{R}$ and the basis vector $\boldsymbol{\tau}_A$, and similarly $\boldsymbol{R}_B = \boldsymbol{R} + \boldsymbol{\tau}_B$. The atomic orbitals are assumed to be localised around their atoms (tightly-bound orbitals) and any overlap between orbitals on different atoms is neglected, giving

$$\langle \boldsymbol{R}_A, A | \boldsymbol{R}'_B, B\rangle = 0, \tag{2.2.1}$$

$$\langle \boldsymbol{R}_A, A | \boldsymbol{R}'_A, A\rangle = \delta_{\boldsymbol{R}_A, \boldsymbol{R}'_A}, \tag{2.2.2}$$

$$\langle \boldsymbol{R}_B, B | \boldsymbol{R}'_B, B\rangle = \delta_{\boldsymbol{R}_B, \boldsymbol{R}'_B}. \tag{2.2.3}$$

To describe the system in reciprocal space, we use the following Fourier transforms

$$|\boldsymbol{q}, A\rangle = \frac{1}{\sqrt{N}} \sum_{\boldsymbol{R}_A} |\boldsymbol{R}_A, A\rangle \, e^{i\boldsymbol{q}\cdot\boldsymbol{R}_A}, \tag{2.2.4}$$

$$|\boldsymbol{R}_A, A\rangle = \frac{1}{\sqrt{N}} \sum_{\boldsymbol{q}} |\boldsymbol{q}, A\rangle \, e^{-i\boldsymbol{q}\cdot\boldsymbol{R}_A}, \tag{2.2.5}$$

$$|\boldsymbol{q}, B\rangle = \frac{1}{\sqrt{N}} \sum_{\boldsymbol{R}_B} |\boldsymbol{R}_B, B\rangle \, e^{i\boldsymbol{q}\cdot\boldsymbol{R}_B}, \tag{2.2.6}$$

$$|\boldsymbol{R}_B, B\rangle = \frac{1}{\sqrt{N}} \sum_{\boldsymbol{q}} |\boldsymbol{q}, B\rangle \, e^{-i\boldsymbol{q}\cdot\boldsymbol{R}_B}. \tag{2.2.7}$$

Here N is the number of unit cells, $N = \prod_i^d N_i$, N_i is the number of primitive unit cells in the direction of lattice vector $\boldsymbol{a}_i$, and d is the number of spatial dimensions. We use periodic boundary conditions (see appendix A) so that $|\boldsymbol{R}_A + N_l \boldsymbol{a}_l, A\rangle = |\boldsymbol{R}_A, A\rangle$, which, applied to equation (2.2.5), gives

$$e^{i\boldsymbol{q}\cdot N_l \boldsymbol{a}_l} = e^{2\pi i m_l}, \tag{2.2.8}$$

$$\boldsymbol{q}\cdot\boldsymbol{a}_l = \frac{2\pi m_l}{N_l}, \tag{2.2.9}$$

where m_l is an integer.

Because the separation of q values decreases with system size, given a large enough system we can replace the summation over q points with a continuous integral

$$\sum_{\boldsymbol{q}} (\ldots) = \left(\frac{L}{2\pi}\right)^d \int d^d\boldsymbol{q}\,(\ldots), \tag{2.2.10}$$

where d is the number of spatial dimensions and L^d is the corresponding volume of the system.

As we have stated, there is no overlap between orbitals on different atomic sites, so

$$\begin{aligned}
\langle \boldsymbol{q}, A|\boldsymbol{q}', A\rangle &= \frac{1}{N}\sum_{\boldsymbol{R}_A,\boldsymbol{R}'_A} \langle \boldsymbol{R}_A, A|\boldsymbol{R}'_A, A\rangle\, e^{i\boldsymbol{q}'\cdot\boldsymbol{R}'_A - i\boldsymbol{q}\cdot\boldsymbol{R}_A}, \\
&= \frac{1}{N}\sum_{\boldsymbol{R}_A,\boldsymbol{R}'_A} \delta_{\boldsymbol{R}_A,\boldsymbol{R}'_A} e^{i\boldsymbol{q}'\cdot\boldsymbol{R}'_A - i\boldsymbol{q}\cdot\boldsymbol{R}_A}, \\
&= \frac{1}{N}\sum_{\boldsymbol{R}_A} e^{i\boldsymbol{R}_A\cdot(\boldsymbol{q}'-\boldsymbol{q})}, \\
&= \delta_{\boldsymbol{q},\boldsymbol{q}'}.
\end{aligned} \tag{2.2.11}$$

Hence

$$\langle \boldsymbol{q}, A|\boldsymbol{q}', B\rangle = 0, \tag{2.2.12}$$

$$\langle \boldsymbol{q}, A|\boldsymbol{q}', A\rangle = \delta_{\boldsymbol{q},\boldsymbol{q}'}, \tag{2.2.13}$$

$$\langle \boldsymbol{q}, B|\boldsymbol{q}', B\rangle = \delta_{\boldsymbol{q},\boldsymbol{q}'}. \tag{2.2.14}$$

The tight-binding Hamiltonian H satisfies

$$H\,|\Phi_{n,\boldsymbol{q}}\rangle = E_n\,(\boldsymbol{q})\,|\Phi_{n,\boldsymbol{q}}\rangle\,, \tag{2.2.15}$$

The energy bands are indexed by integer n, and given the two orbitals in our system there will be two energy bands. We apply Bloch's theorem as we have translational invariance, allowing us to express the eigenstates as linear combinations of the Bloch states

$$|\Phi_{n,\boldsymbol{q}}\rangle = \alpha_n\,(\boldsymbol{q})\,|\boldsymbol{q}, A\rangle + \beta_n\,(\boldsymbol{q})\,|\boldsymbol{q}, B\rangle\,, \tag{2.2.16}$$

where α_n, β_n are expansion coefficients. Note that $|\boldsymbol{q}, A\rangle$ is of the form (2.2.4) and this satisfies Bloch's theorem (2.1.5). By substituting the eigenstate back into the Schrödinger equation (2.2.15) we get

$$\alpha_n H |\boldsymbol{q}, A\rangle + \beta_n H |\boldsymbol{q}, B\rangle = \alpha_n E_n |\boldsymbol{q}, A\rangle + \beta_n E_n |\boldsymbol{q}, B\rangle . \tag{2.2.17}$$

Then multiply by $\langle \boldsymbol{q}, A|$ or $\langle \boldsymbol{q}, B|$

$$\begin{aligned} \alpha_n \langle \boldsymbol{q}, A|H|\boldsymbol{q}, A\rangle + \beta_n \langle \boldsymbol{q}, A|H|\boldsymbol{q}, B\rangle = \alpha_n E_n, \\ \alpha_n \langle \boldsymbol{q}, B|H|\boldsymbol{q}, A\rangle + \beta_n \langle \boldsymbol{q}, B|H|\boldsymbol{q}, B\rangle = \beta_n E_n. \end{aligned} \tag{2.2.18}$$

These equations can be considered as rows found by expanding the eigenvalue equation

$$H(\boldsymbol{q}) |u_n(\boldsymbol{q})\rangle = E_n(\boldsymbol{q}) |u_n(\boldsymbol{q})\rangle , \tag{2.2.19}$$

where

$$|u_n(\boldsymbol{q})\rangle = \begin{pmatrix} \alpha_n(\boldsymbol{q}) \\ \beta_n(\boldsymbol{q}) \end{pmatrix} . \tag{2.2.20}$$

Here $H(\boldsymbol{q})$ is a 2×2 matrix and the eigenstate $|u_n(\boldsymbol{q})\rangle$ is a 2×1 column vector (also known as a spinor) consisting of the expansion coefficients α, β of the real space eigenstate $|\Phi_{n,\boldsymbol{q}}\rangle$ in terms of the Bloch functions $|\boldsymbol{q}, A\rangle$ and $|\boldsymbol{q}, B\rangle$. A matrix element of $H(\boldsymbol{q})$ is given by

$$H_{i,j}(\boldsymbol{q}) = \langle \boldsymbol{q}, i|H|\boldsymbol{q}, j\rangle , \quad i, j \in \{A, B\}. \tag{2.2.21}$$

We will refer to the matrix $H(\boldsymbol{q})$ as the Bloch Hamiltonian, and this formalism will be used in our discussion of graphene. In other literature it may be referred to as the "canonical" Bloch Hamiltonian, or the "Basis II" Hamiltonian, because, in this representation of the Hamiltonian, the Fourier transforms depend on the atomic positions $\boldsymbol{R}_A$ and $\boldsymbol{R}_B$. This Hamiltonian has the unfortunate property of not being periodic about the Brillouin zone, $H(\boldsymbol{q} + 2\pi) \neq H(\boldsymbol{q})$, but other forms of the tight-binding Hamiltonian can be found as shown in our discussion of the Su-Schreiffer-Heeger model 2.6 and in appendix B.

In order to determine the matrix elements of the Bloch Hamiltonian (2.2.21)

we substitute in the Bloch functions then apply the Fourier transforms (2.2.4). We begin with the diagonal matrix elements,

$$\begin{aligned} H_{j,j}\left(\boldsymbol{q}\right) &= \langle \boldsymbol{q}, j|H|\boldsymbol{q}, j\rangle \,, \\ &= \frac{1}{N}\sum_{\boldsymbol{R}_j,\boldsymbol{R}'_j} \langle \boldsymbol{R}_j, j|H|\boldsymbol{R}'_j, j\rangle \, e^{i\boldsymbol{q}\cdot\left(\boldsymbol{R}'_j-\boldsymbol{R}_j\right)}. \end{aligned} \tag{2.2.22}$$

If we only take into account contributions from the same atomic sites then $\langle \boldsymbol{R}_j, j|H|\boldsymbol{R}'_j, j\rangle = \langle \boldsymbol{R}_j, j|H|\boldsymbol{R}_j, j\rangle \, \delta_{\boldsymbol{R}_j,\boldsymbol{R}'_j}$. In this case the diagonal elements are

$$H_{j,j}\left(\boldsymbol{q}\right) = \frac{1}{N}\sum_{\boldsymbol{R}_j} \langle \boldsymbol{R}_j, j|H|\boldsymbol{R}_j, j\rangle = \langle \boldsymbol{R}_j, j|H|\boldsymbol{R}_j, j\rangle \,, \tag{2.2.23}$$

as each site of type j gives the same contribution. The diagonal elements of the $\boldsymbol{q}$-space Hamiltonian are real numbers, and we will refer to them as onsite energies.

The off-diagonal matrix elements are found similarly:

$$\begin{aligned} H_{i,j}\left(\boldsymbol{q}\right) &= \langle \boldsymbol{q}, i|H|\boldsymbol{q}, j\rangle \,, \\ &= \frac{1}{N}\sum_{\boldsymbol{R}_i,\boldsymbol{R}_j} \langle \boldsymbol{R}_i, i|H|\boldsymbol{R}_j, j\rangle \, e^{i\boldsymbol{q}\cdot\left(\boldsymbol{R}_j-\boldsymbol{R}_i\right)}. \end{aligned} \tag{2.2.24}$$

In our Hamiltonian H we will only include nearest-neighbour contributions. For a given atom of type i, there will be a small number of nearest-neighbours of type j, which we will index with $l = 1, 2, \ldots, l_{\max}$. Each nearest-neighbour has a lattice vector $\boldsymbol{\delta}_l = \boldsymbol{R}^l_j - \boldsymbol{R}_i$ relative to the first atom i. We only require these neighbouring atoms in the sum when calculating the off-diagonal terms

$$H_{i,j}\left(\boldsymbol{q}\right) = \frac{1}{N}\sum_{\boldsymbol{R}_i}\sum_{l=1}^{l_{\max}} \langle \boldsymbol{R}_i, i|H|\boldsymbol{R}_i+\boldsymbol{\delta}_l, j\rangle \, e^{i\boldsymbol{q}\cdot\boldsymbol{\delta}_l}. \tag{2.2.25}$$

If we also require that matrix elements $\langle \boldsymbol{R}_i, i|H|\boldsymbol{R}_i+\boldsymbol{\delta}_l, j\rangle$ are independent of l (i.e. all bonds are of the same length and evenly distributed around the site i), then the

overlap can be taken out of the sum over l

$$\begin{aligned} H_{i,j}\left(\boldsymbol{q}\right) &= \frac{1}{N}\sum_{\boldsymbol{R}_i}\langle \boldsymbol{R}_i, i|H|\boldsymbol{R}_i+\boldsymbol{\delta}_l, j\rangle \sum_{l=1}^{l_{\max}} e^{i\boldsymbol{q}\cdot\boldsymbol{\delta}_l}, \\ &= \langle \boldsymbol{R}_i, i|H|\boldsymbol{R}_i+\boldsymbol{\delta}_l, j\rangle \sum_{l=1}^{l_{\max}} e^{i\boldsymbol{q}\cdot\boldsymbol{\delta}_l}. \end{aligned} \tag{2.2.26}$$

The matrix element $\langle \boldsymbol{R}_i, i|H|\boldsymbol{R}_i+\boldsymbol{\delta}_l, j\rangle$ is in general complex, but here we will choose a gauge in which all matrix elements are real numbers. Then, just as before with the diagonal term becoming an onsite energy, we refer to it as a "tight-binding parameter", "hopping parameter", or "coupling parameter". The material specific information is contained in the sum of phase factors due to nearest neighbours $\sum_{l=1}^{l_{\max}} e^{i\boldsymbol{q}\cdot\boldsymbol{\delta}_l}$.

2.3 What is Graphene?

Graphene is an atomically-thick single layer of carbon atoms arranged in a honeycomb lattice. The more commonly found graphite consists of many layers of graphene connected by weak interlayer bonds. The graphene honeycomb lattice is not a Bravais lattice, but is instead formed of two interlocked triangular lattices as shown in figure 2.1. This leads to a unit cell of two atoms, one from each triangular lattice, and we choose to use the lattice vectors

$$\boldsymbol{a}_1 = \left(\frac{\sqrt{3}a}{2}, \frac{a}{2}\right), \quad \boldsymbol{a}_2 = \left(\frac{\sqrt{3}a}{2}, -\frac{a}{2}\right), \tag{2.3.1}$$

where $a = |\boldsymbol{a}_1| = |\boldsymbol{a}_2| = \sqrt{3}a_{cc}$ and a_{cc} is the distance between neighbouring carbon atoms.

The reciprocal lattice vectors are found using a dummy unit vector in the z-axis, $a_3 = (0, 0, 1)$:

$$\boldsymbol{b}_1 = 2\pi\frac{\boldsymbol{a}_2 \times \boldsymbol{a}_3}{\boldsymbol{a}_3 \cdot (\boldsymbol{a}_1 \times \boldsymbol{a}_2)}, \quad \boldsymbol{b}_2 = 2\pi\frac{\boldsymbol{a}_3 \times \boldsymbol{a}_1}{\boldsymbol{a}_3 \cdot (\boldsymbol{a}_1 \times \boldsymbol{a}_2)}, \quad \boldsymbol{b}_3 = 2\pi\frac{\boldsymbol{a}_1 \times \boldsymbol{a}_2}{\boldsymbol{a}_3 \cdot (\boldsymbol{a}_1 \times \boldsymbol{a}_2)} \tag{2.3.2}$$

$$\boldsymbol{b}_1 = \frac{2\pi}{a}\left(\frac{1}{\sqrt{3}}, 1\right), \quad \boldsymbol{b}_2 = \frac{2\pi}{a}\left(\frac{1}{\sqrt{3}}, -1\right). \tag{2.3.3}$$

The reciprocal lattice vectors and the first Brillouin zone are shown in figure 2.1. The first Brillouin zone is defined as all of the points in momentum space that are closer to one reciprocal lattice point than all others. The first Brillouin zone is found using a Wigner-Seitz cell, and connecting all perpendicular bisectors of vectors between the given reciprocal lattice point and all other neighbouring reciprocal lattice points. The corners of the first Brillouin zone (where the perpendular bisectors meet each other) are called "K points" or "Dirac points". They are labelled K or K', and are shown as blue circles in the right-hand side of figure 2.1. The two K points along the q_x-axis have reciprocal space coordinates

$$K = \left(\frac{4\pi}{3a}, 0\right), \quad K' = \left(-\frac{4\pi}{3a}, 0\right). \tag{2.3.4}$$

These points are chosen for simplicity, but the others are equivalent to them as they are all connected to K or K' via a reciprocal lattice vector. The K points will be the focus of this work, because the low-energy phenomena of graphene occur in the vicinity of the K valleys, which will be shown in section 2.4.

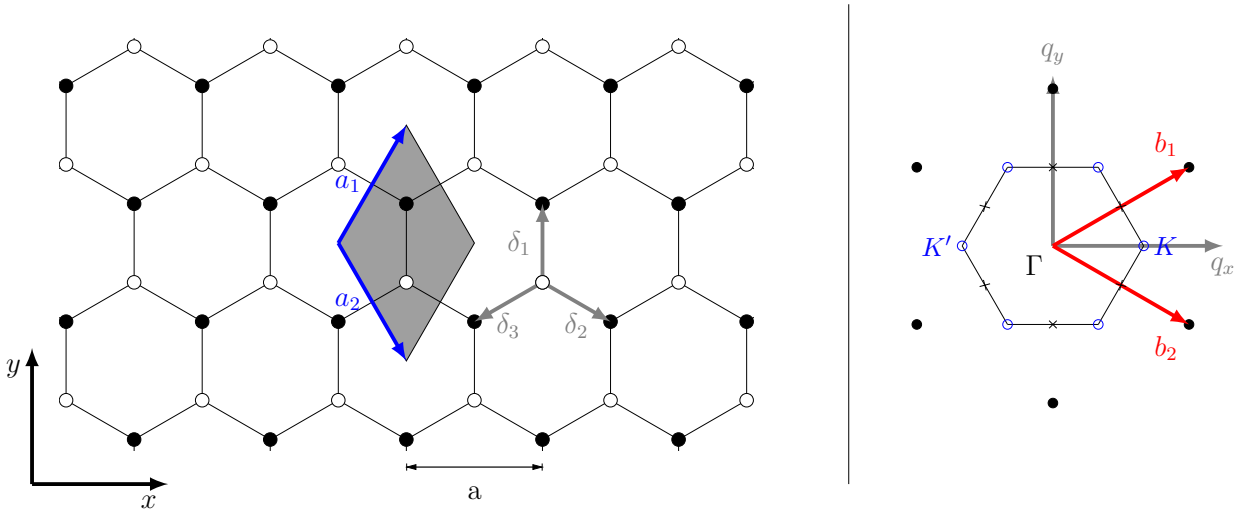

Figure 2.1: Left: monolayer graphene lattice. White circles show sites on the A sublattice, and black circles show sites on the B sublattice. An example unit cell is highlighted in grey. The lattice vectors a_1 and a_2 are shown in blue. The nearest-neighbour vectors δ are shown in grey. Right: reciprocal lattice of monolayer graphene. The reciprocal lattice vectors, b_1 and b_2 are shown in red, the midpoints to all adjacent reciprocal lattice points are marked with black crosses, the K and K' points are marked with blue circles, and the first Brillouin zone is the black hexagon.

2.4 Graphene Tight-Binding Model

The bonding electrons in graphene undergo sp^2 hybridisation so that each atom's single $2s$ orbital and two of the $2p$ orbitals combine, forming three strong in-plane covalent σ bonds, which form the lattice bonds in figure 2.1. This leaves a single p_z orbital on each atomic site, which forms π-bonds with the other carbon atoms. As electronic transport is controlled by the π-bonds, we will treat the graphene lattice as having one orbital per site, with the two atoms per unit cell giving a total of two energy bands. The tight-binding Hamiltonian of graphene in position space is

$$H = -\gamma_0 \sum_{\langle i,j \rangle} |\boldsymbol{R}_{Ai}, A\rangle \langle \boldsymbol{R}_{Bj}, B| + \text{h.c.}, \tag{2.4.1}$$

where $|\boldsymbol{R}_{Ai}, A\rangle$ represents a p_z orbital on the ith atom of type A, $\langle i, j\rangle$ means a sum over nearest-neighbour atoms, and h.c. stands for the Hermitian conjugate. The hopping parameter is the same for all nearest-neighbour bonds,

$$\gamma_0 = -\langle \boldsymbol{R}_{Ai}, A|H|\boldsymbol{R}_{Bj}, B\rangle , \tag{2.4.2}$$

which is defined with a minus sign so that $\gamma_0 > 0$ for graphene ($\gamma_0 \approx 3.16$ eV [60]). The Bloch Hamiltonian is found using (2.2.21), with all of the important information revealed by the relative position of the three nearest neighbours $\boldsymbol{\delta}_l = \boldsymbol{R}_B^l - \boldsymbol{R}_A$, $l = 1, 2, 3$. The off-diagonal matrix element is

$$H_{AB}(\boldsymbol{q}) = -\gamma_0 f(\boldsymbol{q}); \quad f(\boldsymbol{q}) = \sum_{l=1}^{3} e^{i\boldsymbol{q}\cdot\boldsymbol{\delta}_l}, \tag{2.4.3}$$

where the $\boldsymbol{\delta}_l$ are the nearest neighbour vectors with respect to an atom on sublattice A:

$$\boldsymbol{\delta}_1 = \left(0, \frac{a}{\sqrt{3}}\right); \ \boldsymbol{\delta}_2 = \left(\frac{a}{2}, -\frac{a}{2\sqrt{3}}\right); \ \boldsymbol{\delta}_3 = \left(-\frac{a}{2}, -\frac{a}{2\sqrt{3}}\right). \tag{2.4.4}$$

The $\boldsymbol{q}$ space tight-binding Hamiltonian is

$$H(\boldsymbol{q}) = \begin{pmatrix} 0 & -\gamma_0 f(\boldsymbol{q}) \\ -\gamma_0 f^*(\boldsymbol{q}) & 0 \end{pmatrix}, \tag{2.4.5}$$

where

$$f(\boldsymbol{q}) = e^{iq_y a/\sqrt{3}} + 2e^{-iq_y a/2\sqrt{3}} \cos(q_x a/2). \tag{2.4.6}$$

The eigenvalues of the Hamiltonian 2.4.5 are then given by

$$E_{\pm} = \pm\gamma_0 |f(\boldsymbol{q})|, \tag{2.4.7}$$

and the dispersion relation is shown in figure 2.2

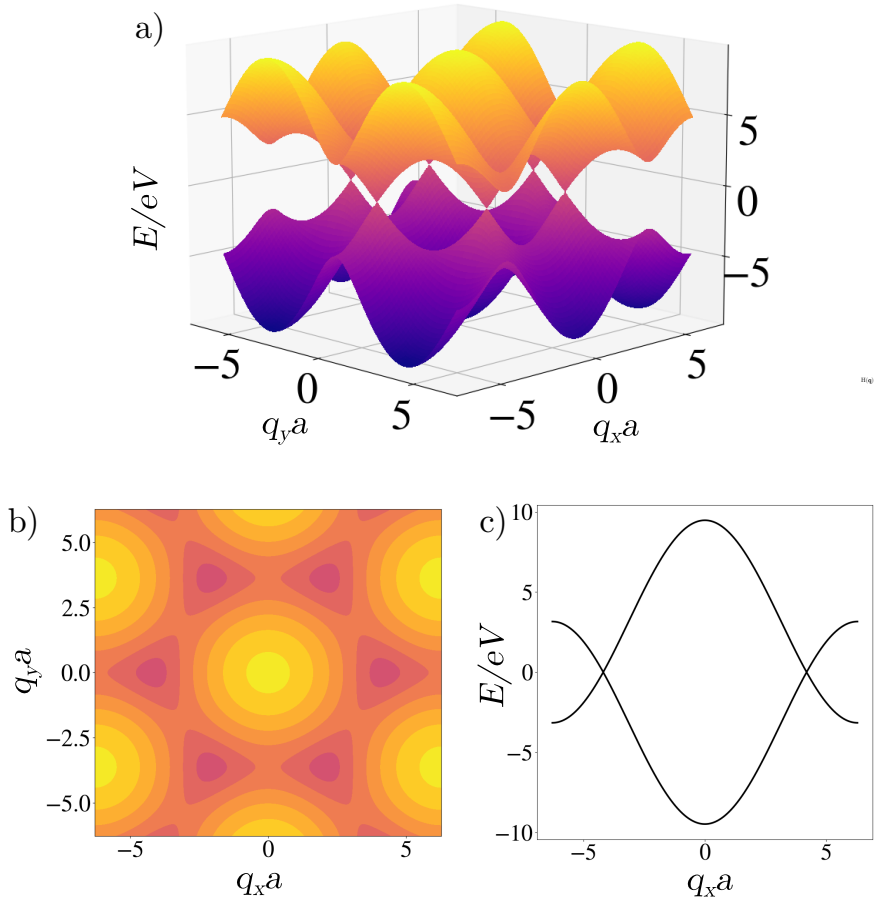

Figure 2.2: Dispersion relations of monolayer graphene found via numerical diagonalisation of the Hamiltonian (2.4.5). Figure a) shows the full dispersion relation of both energy bands in two-dimensional reciprocal space. Figure b) shows a heat map of the upper energy band. Figure c) shows the energy bands with $q_y = 0$ as a function of q_x only. Parameters used are $\gamma_0 = 3.16$ eV [60] and $a = 2.46$ Å[58].

2.4.1 Bilayer Graphene

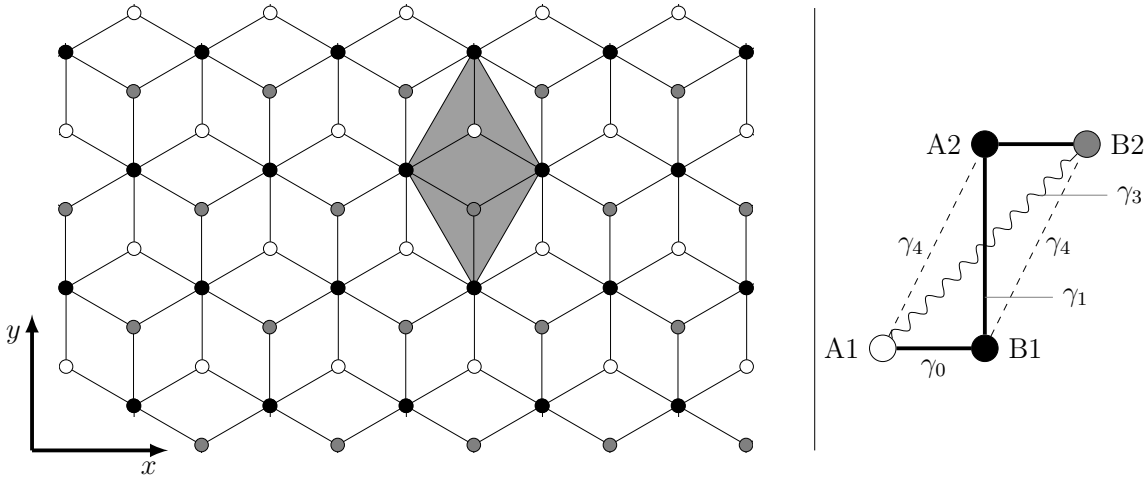

Figure 2.3: Left: Plan of the bilayer graphene lattice. Atoms in sublattices $A1$ and $B1$ of the lower layer are shown as white and black circles, and atoms in sublattices $A2$ and $B2$ on the upper layer are shown as black and grey circles, respectively. An example unit cell is highlighted in grey. Right: Side view of a single unit cell of bilayer graphene, showing the four Slonczewski-Weiss-McClure parameters [61–63].

In the bilayer graphene lattice, there are four atoms in the unit cell - an A and B site from each layer, labelled $j = A1, B2, A2, B2$. Further tight-binding parameters can be defined in the same way as γ_0 (2.4.2), and we use the Slonczewski-Weiss-McClure (SWM) notation [61–63]:

$$\begin{aligned}
\gamma_0 &= -\langle \boldsymbol{R}_{A1}|H|\boldsymbol{R}_{B1}\rangle = -\langle \boldsymbol{R}_{A2}|H|\boldsymbol{R}_{B2}\rangle\,, \\
\gamma_1 &= \langle \boldsymbol{R}_{B1}, B|H|\boldsymbol{R}_{A2}, A\rangle\,, \\
\gamma_3 &= -\langle \boldsymbol{R}_{A1}|H|\boldsymbol{R}_{B2}\rangle\,, \\
\gamma_4 &= \langle \boldsymbol{R}_{A1}|H|\boldsymbol{R}_{A2}\rangle = \langle \boldsymbol{R}_{B1}|H|\boldsymbol{R}_{B2}\rangle\,.
\end{aligned} \tag{2.4.8}$$

These parameters are shown in the right hand side of figure 2.3. The onsite potentials are represented by

$$\epsilon_i = \langle \boldsymbol{R}_i|H|\boldsymbol{R}_i\rangle\,, i \in \{A1, B1, A2, B2\}. \tag{2.4.9}$$

These parameters give the 4×4 tight-binding Hamiltonian

$$H_b(\boldsymbol{q}) = \begin{pmatrix} \epsilon_{A1} & -\gamma_0 f(\boldsymbol{q}) & \gamma_4 f(\boldsymbol{q}) & -\gamma_3 f'^*(\boldsymbol{q}) \\ -\gamma_0 f^*(\boldsymbol{q}) & \epsilon_{B1} & \gamma_1 & \gamma_4 f(\boldsymbol{q}) \\ \gamma_4 f^*(\boldsymbol{q}) & \gamma_1 & \epsilon_{A2} & -\gamma_0 f(\boldsymbol{q}) \\ -\gamma_3 f'(\boldsymbol{q}) & \gamma_4 f^*(\boldsymbol{q}) & -\gamma_0 f^*(\boldsymbol{q}) & \epsilon_{B2} \end{pmatrix}. \tag{2.4.10}$$

The top-left and bottom-right 2×2 blocks of $H_b(\boldsymbol{q})$ are the same as the isolated monolayer (2.4.5); they describe the on-site energies and the nearest neighbour intralayer hopping. The top-right and bottom-left 2×2 matrix block in H_b describe how the two layers couple. Parameter γ_1 describes vertical interlayer hopping between pairs of orbitals on dimer sites $B1$ and $A2$. Because this coupling is entirely vertical (for AB stacked bilayer), the parameter does not include a term in $f(\boldsymbol{q})$. Parameter γ_3 descibes interlayer coupling between the non-dimer sites $A1$ and $B2$, and γ_4 describes interlayer coupling between dimer and non-dimer orbitals; $A1$ to $A2$, or $B1$ to $B2$. Both γ_3 and γ_4 couplings are "skew" - not completely vertical, but with a component of in-plane hopping. The γ_3 terms are multiplied by the function $f'(q)$, which has the same form as $f(q)$, but the lattice vector terms a are all multiplied by a factor of two.

Figure 2.4 shows the dispersion relation of bilayer graphene plotted using the eigenvalues of 2.4.10. We plot along the q_x axis, passing through the K_-, K_+ and Γ points. The tight-binding parameters were determined via infrared spectroscopy $\gamma_0 = 3.16$ eV, $\gamma_1 = 0.381$ eV, $\gamma_3 = 0.38$ eV, $\gamma_4 = 0.14$ eV, $\epsilon_{B1} = \epsilon_{A2} = 0.022$ eV, and $\epsilon_{B1} = \epsilon_{A2} = 0$ [60]. At the K points one conduction and valence band close the gap and meet at zero energy, with the other two bands separated by an energy of the order of the interlayer coupling parameter γ_1. The bands that are separated from zero energy at the K points are due to the dimer sites $B1$ and $A2$, while the zero energy states are due to the edge atoms $A1$ and $B2$, as they do not couple to another layer via the interlayer coupling γ_1.

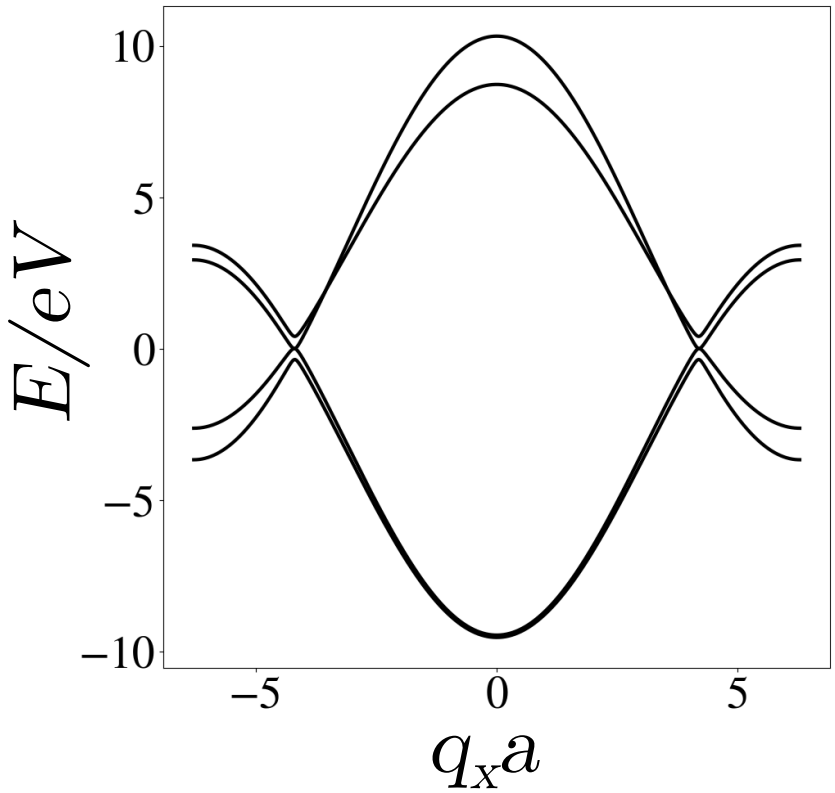

Figure 2.4: Dispersion relation of bilayer graphene with $q_y = 0$ as a function of q_x only. Found via numerical diagonalisation of Hamiltonian (2.4.10). The parameters used are $\gamma_0 = 3.16$ eV, $\gamma_1 = 0.381$ eV, $\gamma_3 = 0.38$ eV, $\gamma_4 = 0.14$ eV, $\epsilon_{B1} = \epsilon_{A2} = 0.022$ eV, $\epsilon_{B1} = \epsilon_{A2} = 0$ [60], and $a = 2.46$ Å[58].

2.4.2 Expansion Near the Dirac Points

When describing the low-energy phenomena of graphene systems it is useful to describe the wave vector relative to the $\boldsymbol{K}$ points using $\boldsymbol{q} = \boldsymbol{K} + \boldsymbol{k}$, where $\boldsymbol{k}$ is very small. We expand the function $f(\boldsymbol{q})$ in powers of $\boldsymbol{k}$ to get

$$\begin{aligned} f(\boldsymbol{q}) &= e^{iq_y a/\sqrt{3}} + 2e^{-iq_y a/2\sqrt{3}} \cos(q_x a/2), \\ f(\boldsymbol{k}) &\approx -\frac{\sqrt{3}a}{2}(\xi k_x - ik_y), \quad \xi = \pm 1. \end{aligned} \tag{2.4.11}$$

The full details of the expansion are given in appendix C. We introduce complex wave vectors π and $\pi^\dagger$

$$\pi = \hbar(\xi k_x + ik_y), \quad \pi^\dagger = \hbar(\xi k_x - ik_y), \tag{2.4.12}$$

which allow us to write the low-energy Hamiltonian in the compact form

$$H_m = \begin{pmatrix} \epsilon_A & v\pi^\dagger \\ v\pi & \epsilon_B \end{pmatrix}, \tag{2.4.13}$$

where $v = \sqrt{3}a\gamma_0/(2\hbar)$ is the band velocity. For intrinsic graphene the onsite potentials are $\epsilon_A = \epsilon_B = 0$, and the eigenvalues will be

$$\begin{aligned} E_\pm &= \pm|v\pi|, \\ &= \pm\hbar v k. \end{aligned} \tag{2.4.14}$$

This is the famous linear dispersion relation of monolayer graphene. As the energy is only dependent on the magnitude of the wave vector, the dispersion relation is isotropic in the vicinity of the K valleys, and "Dirac cones" are formed, shown in figure 2.5. In figure 2.5 we plot the energy eigenvalues of the Hamiltonian (2.4.13) as a function of k_x, normalised by the characteristic wave vector $k_c = \gamma_1/(\hbar v)$ [64], and the energy is plotted in units of γ_1.

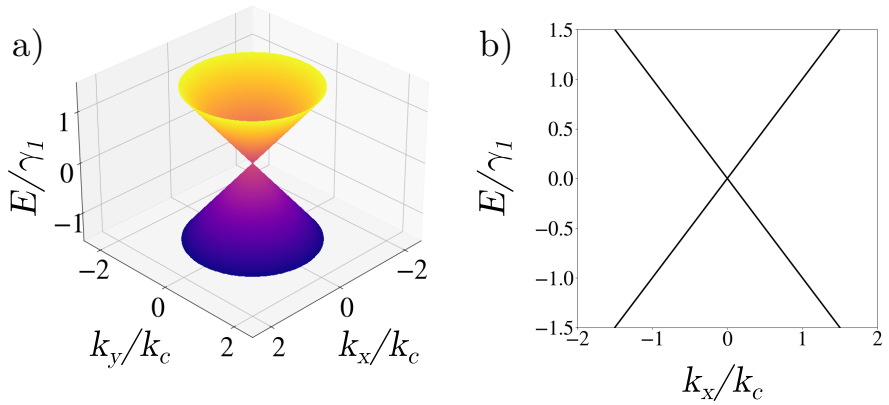

Figure 2.5: Dispersion relations of monolayer graphene near the Dirac points found via numerical diagonalisation of Hamiltonian (2.4.13). Figure a) shows the full dispersion relation of both energy bands in two-dimensional reciprocal space. Figure b) shows the energy bands with $k_y = 0$ as a function of k_x only. Parameters used are $\epsilon_A = \epsilon_B = 0$, $\gamma_0 = 3.16$ eV [60] and $a = 2.46$ Å[58]. In both figures the wave vectors are normalised by the characteristic wave vector $k_c = \gamma_1/(\hbar v)$ and the energy is given in units of γ_1.

In bilayer graphene, equation (2.4.10) is reduced to

$$H_b = \begin{pmatrix} \epsilon_{A1} & v\pi^\dagger & -v_4\pi^\dagger & v_3\pi \\ v\pi & \epsilon_B & \gamma_1 & -v_4\pi^\dagger \\ -v_4\pi & \gamma_1 & \epsilon_{A2} & v\pi^\dagger \\ v_3\pi^\dagger & -v_4\pi & v\pi & \epsilon_{B2} \end{pmatrix}, \tag{2.4.15}$$

where we have introduced the effective velocities $v_3 = \sqrt{3}a\gamma_3/2\hbar$ and $v_4 = \sqrt{3}a\gamma_4/2\hbar$.

Figure 2.6 shows the dispersion relation of bilayer graphene near the K point plotted using the eigenvalues of 2.4.15. We plot along the k_x axis and normalise by the characteristic wave vector k_c. The tight-binding parameters are the same as those used in section 2.4.1: $\gamma_0 = 3.16$ eV, $\gamma_1 = 0.381$ eV, $\gamma_3 = 0.38$ eV, $\gamma_4 = 0.14$ eV, $\epsilon_{B1} = \epsilon_{A2} = 0.022$ eV, and $\epsilon_{B1} = \epsilon_{A2} = 0$ [60]. In figure 2.6 the black lines show the eigenvalues with all parameters present, and red lines show the same dispersion but in the minimal model, with only nearest-neighbour hopping: $\gamma_3 = \gamma_4 = 0$.

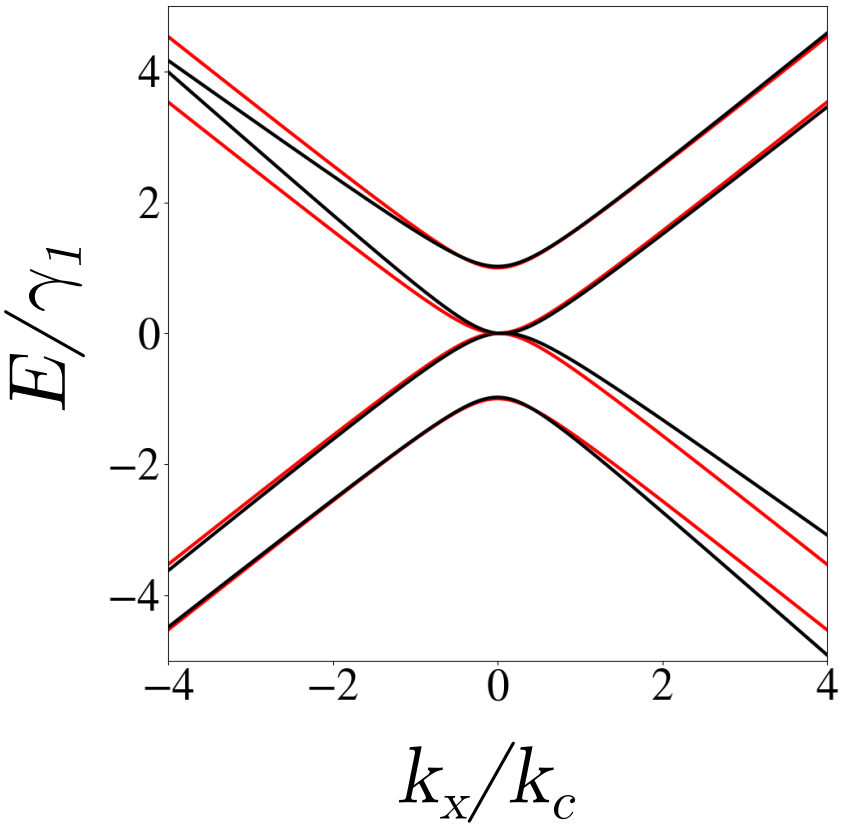

Figure 2.6: Dispersion relations of bilayer graphene near the Dirac points. Both sets of eigenvalues were found using numerical diagonalisation of Hamiltonian (2.4.15), with black lines showing results using all parameters and red lines showing results with nearest-neighbour hopping only. We have set $k_y = 0$ and plotted the energy as a function of k_x only. Parameters used are $\gamma_0 = 3.16$ eV, $\gamma_1 = 0.381$ eV, $\gamma_3 = 0.38$ eV, $\gamma_4 = 0.14$ eV, $\epsilon_{B1} = \epsilon_{A2} = 0.022$ eV, $\epsilon_{B1} = \epsilon_{A2} = 0$ [60], and $a = 2.46$ Å[58]. The wave vector k_x is normalised by the characteristic wave vector $k_c = \gamma_1/(\hbar v)$ and the energy is given in units of γ_1.

2.4.3 N-layer Graphite

The Hamiltonian of N-layer rhombohedrally-stacked graphite in the minimal model (nearest-neighbour hopping only), and in the basis of all $2N$ atomic sites is given by

$$H = \begin{pmatrix} D & V & 0 & 0 & \dots \\ V^\dagger & D & V & 0 & \dots \\ 0 & V^\dagger & D & V & \dots \\ 0 & 0 & V^\dagger & D & \dots \\ \vdots & \vdots & \vdots & \vdots & \ddots \end{pmatrix}, \tag{2.4.16}$$

where the 2×2 matrix blocks are

$$D = \begin{pmatrix} 0 & v\pi^\dagger \\ v\pi & 0 \end{pmatrix}, \quad V = \begin{pmatrix} 0 & 0 \\ \gamma_1 & 0 \end{pmatrix}, \quad \pi = \hbar\left(\xi k_x + i k_y\right). \tag{2.4.17}$$

Here $\xi = \pm 1$, depending on if the momentum is being calculated relative to a K or K' point, $\hbar$ is the reduced Planck's constant, and $v = \sqrt{3}a\gamma_0/(2\hbar)$ is the group velocity. The matrix block D describes hopping within one graphene sheet, and matrix block V describes hopping between atomic sites B_n on layer n and A_{n+1} of the layer above. The matrix block V will vary depending on the stacking type, i.e. for rhombohedral stacking it acts to connect site B_n on layer n to the A_{n+1} site of the layer above. For Bernal stacking the off diagonal blocks must alternate between V and V' and for AA stacking V would be a diagonal matrix block.

The dispersion relation for $N = 10$ layers of rhombohedrally stacked graphite is shown in figure 2.7. Here we numerically diagonalise the Hamiltonian (2.4.16), and plot the energy in units of γ_1 as a function of the wave vector k_x, which is normalised by the characteristic wave vector k_c. For N-layers of rhobohedrally-stacked graphite there are two zero-energy states for $|k| < k_c$ due to the non-dimer sites on the top and bottom layers, and the rest of the states are in the bulk conductance and valence bands. The wavevector $|k| = k_c$ corresponds to the point of the phase transition between the topological and topologically trivial phases of the SSH model, this explains why there are zero-energy edge states for $|k| < k_c$ and why they are no longer present for $|k| \geq k_c$.

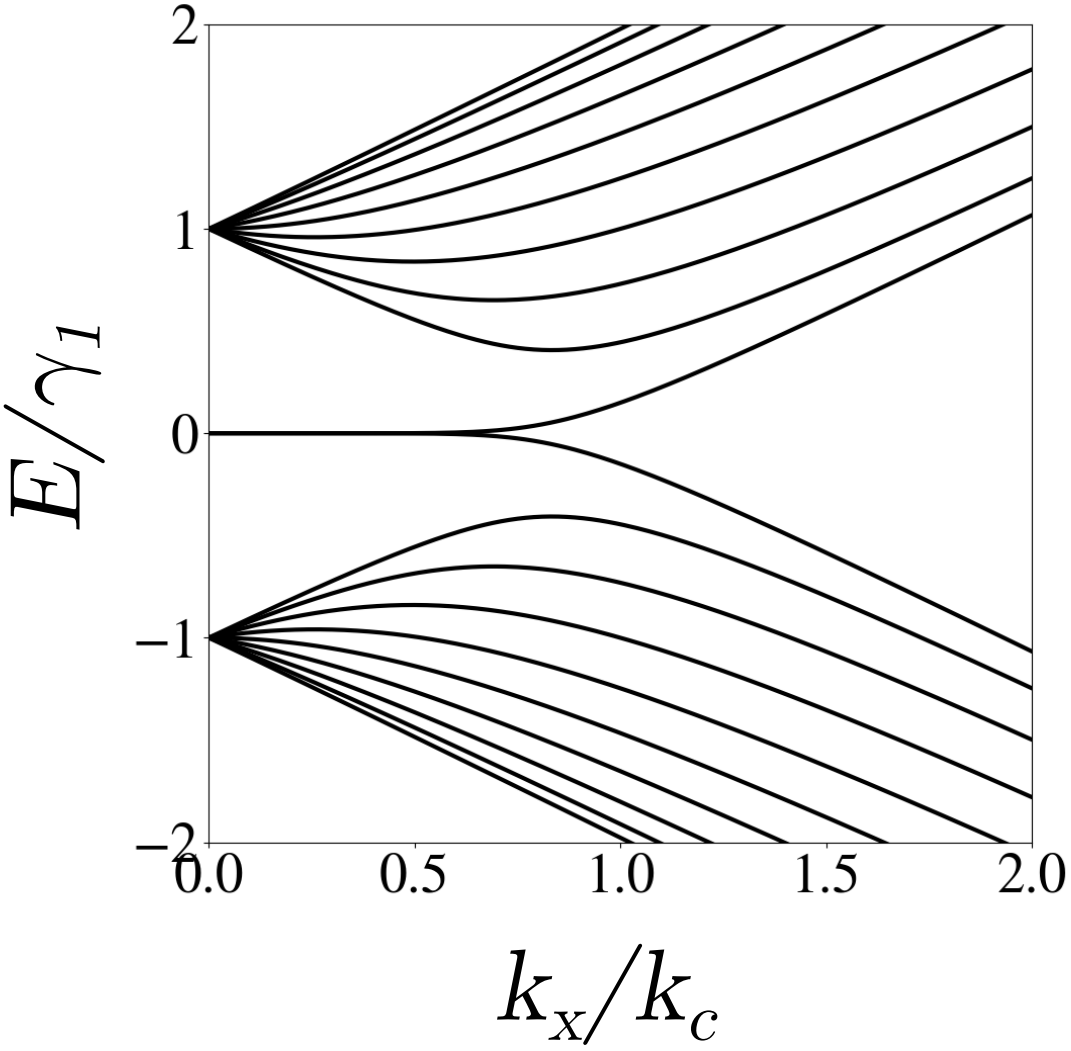

Figure 2.7: Dispersion relation for a rhombohedrally-stacked graphite system of $N = 10$ layers found using numerical diagonalisation of Hamiltonian (2.4.16). The energy is given in units of interlayer hopping γ_1, and the momentum in terms of the critical momentum $k_c = \gamma_1/\hbar v$. The parameters used are $\gamma_0 = 3.16$ eV, $\gamma_1 = 0.381$ eV [60], and $a = 2.46$ Å[58]. The wave vector k_x is normalised by the characteristic wave vector $k_c = \gamma_1/(\hbar v)$ and the energy is given in units of γ_1.

2.4.4 Low-Energy Model

A low-energy effective Hamiltonian can be formed from the full 2N by 2N Hamiltonian by eliminating orbitals relating to dimer sites. We reproduce the steps as derived by McCann and Koshino [65] here. First change the Hamiltonian basis so the low- and high-energy states are separated. The low-energy components are grouped into matrix block θ and the dimer components are grouped into matrix block χ,

$$\begin{pmatrix} h_\theta & u \\ u^\dagger & h_\chi \end{pmatrix} \begin{pmatrix} \theta \\ \chi \end{pmatrix} = E \begin{pmatrix} \theta \\ \chi \end{pmatrix}. \tag{2.4.18}$$

Then find an expression for χ using the second row and substitute it into the first to get an effective eigenvalue equation for the low-energy components,

$$\chi = (E - h_\chi)^{-1} u^\dagger \theta, \tag{2.4.19}$$

$$\left[h_\theta + u\,(E - h_\chi)^{-1} u^\dagger\right] \theta = E\theta, \tag{2.4.20}$$

$$\left[h_\theta - u h_\chi^{-1} u^\dagger\right] \theta \approx ES\theta, \tag{2.4.21}$$

where $S = 1 + u h_\chi^{-2} u^\dagger$. Equation (2.4.21) is accurate up to linear terms in E. Finally, perform a transformation $\Phi = S^{1/2}\theta$:

$$\left[h_\theta - u h_\chi^{-1} u^\dagger\right] S^{-1/2}\Phi \approx E S^{1/2}\Phi, \tag{2.4.22}$$

$$S^{1/2}\left[h_\theta - u h_\chi^{-1} u^\dagger\right] S^{-1/2}\Phi \approx E\Phi. \tag{2.4.23}$$

This transformation ensures that the normalisation of Φ is consistent with that of the original states:

$$\Phi^\dagger\Phi = \theta^\dagger S\theta = \theta^\dagger\left(1 + u h_\chi^{-2} u^\dagger\right)\theta, \tag{2.4.24}$$

$$\approx \theta^\dagger\theta + \chi^\dagger\chi, \tag{2.4.25}$$

where we have used equation (2.4.19) for small E: $\chi \approx -h_\chi^{-1} u^\dagger\theta$. Thus, the effective Hamiltonian for low-energy components is given by equation (2.4.23):

$$H^{(eff)} \approx S^{-1/2}\left[h_\theta - u h_\chi^{-1} u^\dagger\right] S^{-1/2}, \tag{2.4.26}$$

$$S = 1 + uh_{\chi}^{-2}u^{\dagger}. \tag{2.4.27}$$

This expression will be used in chapters 3 and 4 to derive low-energy Hamiltonians for the multilayer systems with stacking faults. A worked example using this model to find the low energy effective Hamiltonian of bilayer graphene is given in appendix D.

2.5 Symmetries

In order to classify physical systems into different categories we study their symmetries. The three non-spatial symmetries (time-reversal, chiral, and charge-conjugation symmetry) describe universal properties of systems. For example, time-reversal symmetry can be used to describe the energy level statistics of a system, meaning that the same energy level statistics will be the same across different systems with the same type of time-reversal symmetry. In this way, symmetries can then be used to predict which physical phenomena will be present.

For a Hamiltonian $H(\boldsymbol{k})$, chiral (S), time-reversal (T), charge-conjugation (C), and spatial inversion (P) symmetries are defined by

$$\begin{aligned} \text{chiral:} \quad & U_S^\dagger(k) H(k) U_S(k) = -H(k), \\ \text{time:} \quad & U_T^\dagger(k) H^*(k) U_T(k) = H(-k), \\ \text{charge:} \quad & U_C^\dagger(k) H^*(k) U_C(k) = -H(-k), \\ \text{space:} \quad & U_P^\dagger(k) H(k) U_P(k) = H(-k), \end{aligned} \tag{2.5.1}$$

where each of these are unitary or antiunitary matrices with

$$\begin{aligned} U_S(k) U_S(k) &= I, \\ U_T(k) U_T^*(-k) &= \pm I, \\ U_C(k) U_C^*(-k) &= \pm I. \end{aligned} \tag{2.5.2}$$

The three non-spatial symmetries are related by $U_S(k) = U_C^*(k) U_T(-k)$.

Given an energy eigenvalue equation $H(k)\psi_\pm(k) = E_\pm(k)\psi_\pm(k)$ for two energy bands $E_\pm(k)$ and eigenstates $\psi_\pm(k)$, the effects of the symmetries are

$$\begin{aligned} \text{chiral:} \quad & E_\pm(k) = -E\mp(k), \\ \text{time:} \quad & E_\pm(-k) = E_\pm(k), \\ \text{charge:} \quad & E_\pm(-k) = -E\mp(k), \\ \text{space:} \quad & E_\pm(-k) = E_\pm(k). \end{aligned} \tag{2.5.3}$$

In position space, the symmetry operators for chiral, time, or charge-conjugation

are written as

$$\begin{aligned} \text{chiral:} \quad & \mathcal{S}^\dagger H \mathcal{S} = -H, \quad \mathcal{S}\mathcal{S} = I \\ \text{time:} \quad & \mathcal{T} H^* \mathcal{T} = H, \quad \mathcal{T}\mathcal{T}^* = \pm I, \\ \text{charge:} \quad & \mathcal{C}^\dagger H^* \mathcal{C} = -H, \quad \mathcal{C}\mathcal{C}^* = \pm I, \\ \text{space:} \quad & \mathcal{P}^\dagger H \mathcal{P} = H, \end{aligned} \tag{2.5.4}$$

where the matrices $\mathcal{S}$, $\mathcal{T}$, $\mathcal{C}$, and $\mathcal{P}$ are unitary, and related by $\mathcal{S} = \mathcal{T} * \mathcal{C}$. Note that while there are three types of time reversal symmetry ($\mathcal{T} = \pm 1$, $\mathcal{T} = 0$), throughout this thesis we will only consider position-space Hamiltonians whose matrix elements are all real, meaning that the time reversal operator will always square to $\mathcal{T}^2 = 1$. Given a system with symmorphic symmetry (one that does not involve a translation), the position space symmetry operators act locally within a unit cell, and may be represented by $\mathcal{J} \times \mathcal{J}$ matrices S_x, S_y, or S_z acting in the atomic basis as

$$S_x = \begin{pmatrix} 0 & 1 & 0 & 0 & \dots & 0 & 0 \\ 1 & 0 & 0 & 0 & \dots & 0 & 0 \\ 0 & 0 & 0 & 1 & \dots & 0 & 0 \\ 0 & 0 & 1 & 0 & \dots & 0 & 0 \\ \vdots & \vdots & \vdots & \vdots & \vdots & \vdots & \vdots \\ 0 & 0 & 0 & 0 & \dots & 0 & 1 \\ 0 & 0 & 0 & 0 & \dots & 1 & 0 \end{pmatrix}, \tag{2.5.5}$$

$$S_y = \begin{pmatrix} 0 & -i & 0 & 0 & \dots & 0 & 0 \\ i & 0 & 0 & 0 & \dots & 0 & 0 \\ 0 & 0 & 0 & -i & \dots & 0 & 0 \\ 0 & 0 & i & 0 & \dots & 0 & 0 \\ \vdots & \vdots & \vdots & \vdots & \vdots & \vdots & \vdots \\ 0 & 0 & 0 & 0 & \dots & 0 & -i \\ 0 & 0 & 0 & 0 & \dots & i & 0 \end{pmatrix}, \tag{2.5.6}$$

$$S_z = \begin{pmatrix} 1 & 0 & 0 & 0 & \dots & 0 & 0 \\ 0 & -1 & 0 & 0 & \dots & 0 & 0 \\ 0 & 0 & 1 & 0 & \dots & 0 & 0 \\ 0 & 0 & 0 & -1 & \dots & 0 & 0 \\ \vdots & \vdots & \vdots & \vdots & \vdots & \vdots & \vdots \\ 0 & 0 & 0 & 0 & \dots & 1 & 0 \\ 0 & 0 & 0 & 0 & \dots & 0 & -1 \end{pmatrix}, \tag{2.5.7}$$

where $\mathcal{J}$ is the number of atoms in the system.

Spatial inversion symmetry (parity) $\mathcal{P}$ is non-local, and may be represented by the $\mathcal{J} \times \mathcal{J}$ matrices P_x, P_y, P_z, or P_0, where

$$P_x = \begin{pmatrix} 0 & 0 & 0 & \dots & 0 & 1 \\ 0 & 0 & 0 & \dots & 1 & 0 \\ \vdots & \vdots & \vdots & \ddots & \vdots & \vdots \\ 0 & 0 & 1 & \dots & 0 & 0 \\ 0 & 1 & 0 & \dots & 0 & 0 \\ 1 & 0 & 0 & \dots & 0 & 0 \end{pmatrix}, \tag{2.5.8}$$

$$P_y = \begin{pmatrix} 0 & 0 & 0 & \dots & 0 & 1 \\ 0 & 0 & 0 & \dots & -1 & 0 \\ \vdots & \vdots & \vdots & \ddots & \vdots & \vdots \\ 0 & 0 & -1 & \dots & 0 & 0 \\ 0 & 1 & 0 & \dots & 0 & 0 \\ -1 & 0 & 0 & \dots & 0 & 0 \end{pmatrix}, \tag{2.5.9}$$

$$P_z = \begin{pmatrix} 0 & 0 & 0 & 0 & \dots & 1 & 0 \\ 0 & 0 & 0 & 0 & \dots & 0 & -1 \\ \vdots & \vdots & \vdots & \vdots & \ddots & \vdots & \vdots \\ 0 & 0 & 1 & 0 & \dots & 0 & 0 \\ 0 & 0 & 0 & -1 & \dots & 0 & 0 \\ 1 & 0 & 0 & 0 & \dots & 0 & 0 \\ 0 & -1 & 0 & 0 & \dots & 0 & 0 \end{pmatrix}, \tag{2.5.10}$$

$$P_0 = \begin{pmatrix} 0 & 0 & 0 & 0 & \dots & 1 & 0 \\ 0 & 0 & 0 & 0 & \dots & 0 & 1 \\ \vdots & \vdots & \vdots & \vdots & \ddots & \vdots & \vdots \\ 0 & 0 & 1 & 0 & \dots & 0 & 0 \\ 0 & 0 & 0 & 1 & \dots & 0 & 0 \\ 1 & 0 & 0 & 0 & \dots & 0 & 0 \\ 0 & 1 & 0 & 0 & \dots & 0 & 0 \end{pmatrix}, \tag{2.5.11}$$

These matrices will be used in sections 2.6 and 2.7 to calculate the polarisation of the SSH and CDW models in real space.

2.6 Su-Schreiffer-Heeger Model

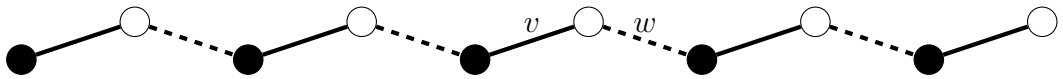

Figure 2.8: Diagram showing the SSH chain. Each unit cell contains two atoms; a black circle on sublattice A and a white circle on sublattice B. The alternating coupling strengths v and w are shown with solid and dashed lines, respectively.

The Su-Schreiffer-Heeger (SSH) [66–69] model was originally used to model polyacetylene; a polymer chain of carbon atoms with alternating double and single bonds, and one hydrogen bonded to each carbon atom. The model consists of a one-dimensional chain of atoms with alternating hopping parameters v and w as shown in figure 2.8. The chain is formed of N unit cells, each with two atomic sites, labelled A and B. The electronic properties can be described by a single particle Hamiltonian [67] of the form

$$\hat{H} = v \sum_{m=1}^{N} |x_{m,A}, A\rangle \langle x_{m,B}, B| + w \sum_{m=1}^{N-1} |x_{m,B}, B\rangle \langle x_{m+1,A}, A| + \text{h.c.}, \tag{2.6.1}$$

where the first term describes intracell hopping with strength v and the second term describes intercell hopping with strength w. The terms $|x_{m,A}, A\rangle$ and $|x_{m,B}, B\rangle$ represent states with atomic positions $x_{m,A} = ma$ and $x_{m,B} = (m + 1/2)\, a$ on sublattices A and B, respectively, and h.c. stands for Hermitian conjugate. As spin is not included, the SSH model describes spin-polarised electrons. The real space Hamiltonian $\hat{H}$ 2.6.1 can be written using a matrix H as $\hat{H} = \Psi^\dagger H \Psi$, where Ψ is a column vector of atomic orbitals. For a chain of $N = 4$ unit cells the matrix H is

$$H = \begin{pmatrix} 0 & v & 0 & 0 & 0 & 0 & 0 & 0 \\ v & 0 & w & 0 & 0 & 0 & 0 & 0 \\ 0 & w & 0 & v & 0 & 0 & 0 & 0 \\ 0 & 0 & v & 0 & w & 0 & 0 & 0 \\ 0 & 0 & 0 & w & 0 & v & 0 & 0 \\ 0 & 0 & 0 & 0 & v & 0 & w & 0 \\ 0 & 0 & 0 & 0 & 0 & w & 0 & v \\ 0 & 0 & 0 & 0 & 0 & 0 & v & 0 \end{pmatrix}. \tag{2.6.2}$$

The majority of the important physical properties of this system will be defined by the bulk, because in the thermodynamic limit, $N \to \infty$, only a negligible part of the system is described by anything other than the bulk physics. To investigate the bulk properties first apply periodic boundary conditions $|x_{m+N,A}, A\rangle = |x_{m,A}, A\rangle$ and use the following Fourier transforms to find the momentum-space Hamiltonian for an infinitely long SSH chain.

$$|k, A\rangle = \frac{1}{\sqrt{N}} \sum_m |x_{m,A}, A\rangle \, e^{ikma}, \tag{2.6.3a}$$

$$|x_{m,A}, A\rangle = \frac{1}{\sqrt{N}} \sum_k |k, A\rangle \, e^{-ikma}, \tag{2.6.3b}$$

$$|k, B\rangle = \frac{1}{\sqrt{N}} \sum_m |x_{m,B}, B\rangle \, e^{ikma}, \tag{2.6.3c}$$

$$|x_{m,B}, B\rangle = \frac{1}{\sqrt{N}} \sum_k |k, B\rangle \, e^{-ikma}. \tag{2.6.3d}$$

Here k is the wave vector measured relative to the $\mathbf{\Gamma}$ point. As in appendix A the periodic boundary conditions applied to the Fourier transforms lead to

$$e^{ikNa} = 1, \quad \Rightarrow \quad k = \frac{2\pi l}{Na}, \tag{2.6.4}$$

where k is chosen to be within the first Brillouin zone $-\pi/a < k \leq \pi/a$ and l is an integer $l = -(N/2) + 1, 1, \ldots, -1, 0, 1, \ldots, (N/2)$. We assume there is no overlap between the atomic orbitals

$$\langle x_{m,A}, A | x_{m',A}, A\rangle = \delta_{m,m'}; \quad \langle k, A | k', A\rangle = \delta_{k,k'}. \tag{2.6.5}$$

The bulk momentum-space Hamiltonian in the basis of the A and B atomic sites is

$$H(k) = \begin{pmatrix} 0 & v + we^{-ika} \\ v + we^{ika} & 0 \end{pmatrix}. \tag{2.6.6}$$

In real space, with a finite length chain of atoms, the definition of the unit cell is simple because it must span the system. This means for the SSH model it will have one boundary on the left edge of the chain (including an atom on sublattice A) and extend until just before the next atom of sublattice A. This unit cell then repeats

all the way until the end of the chain. However, in k-space the definition of the unit cell is ambiguous. This is because to define the SSH chain in k-space you must either consider a chain of infinite physical length, or a chain whose ends connect to form a ring, and in both cases there will be no restriction on the first boundary of the unit cell. The ambiguity of the definition of the unit cell leads to subtle changes in the resulting Bloch Hamiltonian, which is why we defined the Fourier transforms (2.6.3) in such a way as to not be dependent on the chosen unit cell. These Fourier transforms also specify that the A and B sites within the same unit cell share the same physical space, but this does not change the tight-binding parameters v and w.

The derivation of the Hamiltonian (2.6.6) was chosen so that it is periodic about the first Brillouin zone, this is an important property that is necessary to understand the topology of the system, and without a periodic Hamiltonian it is impossible to calculate the winding number, which is presented later in this section. See appendix B for more details on alternate Hamiltonians.

The bulk momentum space Hamiltonian (2.6.6) has simple eigenvalues

$$E(k) = \pm\sqrt{v^2 + w^2 + 2vw\cos ka}. \tag{2.6.7}$$

The dispersion relation will have different forms depending on the relationship between the two hopping terms v and w. This can happen naturally in solid state systems through Peierls instability [70]. Figure 2.9 shows dispersion relations of the bulk momentum-space Hamiltonian 2.6.6 for different values of the hopping parameters v and w. If the hopping terms are equal, $v = w$, then the system is a conductor, and there is no band gap between the contuctance and valence electron bands. The staggered hopping opens a gap $\Delta = 2|v - w|$, but if either parameter is zero then the system breaks into dimers with energies $E(k) = \pm v$ or $E(k) = \pm w$.

The symmetry operators of the SSH model for chiral, time-reversal, charge-conjugation, and spatial-inversion symmetry are represented in k-space and position space in table 2.1. The combination of symmmetries found in this model mean it is in the symmetry class BDI [69, 71].

The chiral symmetry of the SSH model is represented by S_z (2.5.7) in position

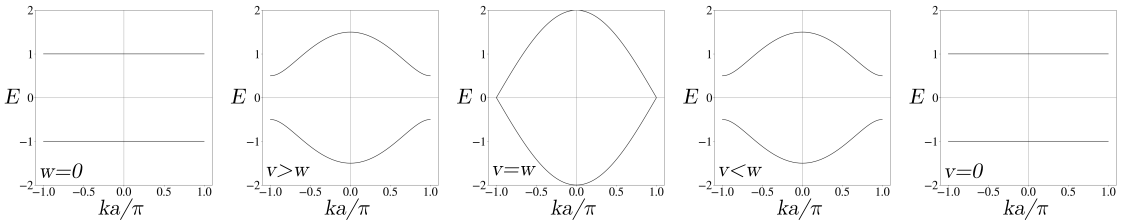

Figure 2.9: Dispersion relations for SSH chains with different values of hopping parameters v and w. The graphs on the far left and right show the fully dimerised chains, with $w = 0$ or $v = 0$, respectively. The centre graph shows equal hopping parameters, $v = w$. The band gap is shown to close at $k = \pm\pi$. Either side of the centre are the graphs with $v \neq w \neq 0$. In all five cases the band gap is $\Delta = 2|v - w|$.

	k-space	position space
chiral	σ_z	S_z
time	σ_0	I
charge	σ_z	S_z
space	σ_x	P_x

Table 2.1: Symmetries of the Su-Schreiffer-Heeger model in k-space and position space. σ_x and σ_z are the Pauli matrices, S_z and P_z are defined in section 2.5 as equations (2.5.7) and (2.5.10).

space. We consider the expectation value of the chiral operator

$$p_z = \langle\psi|S_z|\psi\rangle\,, \tag{2.6.8}$$

and refer to this as a generalisation of electric polarisation.

The SSH model is an example of a two-band model. The charge-density wave (CDW) model, which will be discussed in section 2.7, and the Rice Mele model, discussed in section 2.8, are also two-band models. The bulk momentum-space Hamiltonians of any two-band model can be represented by the Hamiltonian (2.6.9) [69]

$$H(k) = \boldsymbol{\sigma}\cdot\boldsymbol{d} = \begin{pmatrix} d_z & d_x - id_y \\ d_x + id_y & -d_z \end{pmatrix}, \tag{2.6.9}$$

where $\boldsymbol{\sigma}$ is the vector of Pauli spin matrices, and $\boldsymbol{d}$ is a vector whose components are real numbers specific to the model in question.

The eigenvalue equation $H|n\rangle = E_n|n\rangle$ can be solved using $\det(E_\pm I_2 - H) = 0$ to give eigenvalues

$$E_\pm = \pm d, \tag{2.6.10}$$

where

$$d = |\boldsymbol{d}| = \sqrt{d_x^2 + d_y^2 + d_z^2}. \tag{2.6.11}$$

This means that the eigenvalues only depend on the magnitude of $\boldsymbol{d}$ and not the direction of the vector. The spinor eigenstates can also be found in terms of components of $\boldsymbol{d}$ by expanding the second row of the energy eigenvalue equation with the spinor eigenstates written as $|n_\pm\rangle = \left(\begin{smallmatrix} A \\ B \end{smallmatrix}\right)$

$$\begin{pmatrix} d_z & d_x - id_y \\ d_x + id_y & -d_z \end{pmatrix} \begin{pmatrix} A \\ B \end{pmatrix} = E_\pm \begin{pmatrix} A \\ B \end{pmatrix} \tag{2.6.12}$$

$$\begin{aligned} (d_x + id_y)\, A - d_z B &= E_\pm B \\ \rightarrow (d_x + id_y)\, A &= (d_z \pm d)\, B, \end{aligned} \tag{2.6.13}$$

where the substitution $E_\pm = \pm d$ has been used. The eigenstates are then

$$\begin{aligned} |n_\pm\rangle &= \begin{pmatrix} A \\ B \end{pmatrix}, \\ &= \begin{pmatrix} (d_z \pm d)\, A \\ (d_z \pm d)\, B \end{pmatrix}, \\ &= A \begin{pmatrix} d_z \pm d \\ d_x + id_y \end{pmatrix}. \end{aligned} \tag{2.6.14}$$

In the second line the spinor has been multiplied by a constant $(d_z \pm d)$ and in the third line we have substituted in our result from equation (2.6.13). The remaining prefactor A can be considered as a normalisation constant.

The components of $\boldsymbol{d}$ for the SSH model (2.6.6) are

$$d_x(k) = v + w\cos ka, \quad d_y(k) = w\sin ka, \quad d_z(k) = 0. \tag{2.6.15}$$

Substituting these into equation (2.6.10) returns the eigenvalues (2.6.7) we had directly calculated from the Bloch Hamiltonian (2.6.6). As the wave vector k spans the Brillouin zone $-\pi/a < k \leq \pi/a$, the vector $\boldsymbol{d}$ traces a circle on the d_x-d_y plane.

The equation of this circle is

$$(d_x - v)^2 + d_y^2 = w^2, \tag{2.6.16}$$

having radius w, and being centred at $(v, 0)$.

In order for these parameters to describe an insulator, the path that the vector $\boldsymbol{d}(k)$ traces as k passes through the Brillouin zone must be a closed loop that does not pass through the origin. If the loop passes through the origin, $\boldsymbol{d}(k) = 0$, and the system is no longer an insulator (there will be no band gap).

Different topological phases of the SSH model can be described using the winding number, n_w, which counts the number of times the path of $\boldsymbol{d}(k)$ wraps around the origin in the $(d_x d_y)$ plane. Given a system with $v > w$, the radius of the loop is always less than the distance of the centre of the loop from the origin. This means that the loop cannot touch nor enclose the origin, so the winding number will be $n_w = 0$. For this reason, the system with $v > w$ is called the "topologically trivial" case. The other case is the "topologically nontrivial" case with $v < w$. Here the radius now exceeds the distance between the centre of the circle and the origin, so the loop will wrap around the origin once, giving a winding number $n_w = 1$. The final phase of the SSH model is the metallic phase, with equal hoppings $v = w$. In this case, the loop will always pass through the origin, closing the band gap, and the winding number cannot be defined.

The winding number can be used to make a connection between the bulk and edges of the system, this is known as the bulk-edge correspondence. First consider a long one-dimensional system where the left hand side of the chain is in the topologically trivial phase ($v > w$), and the right hand side is in the topologically nontrivial phase ($v < w$). In the centre of the system there must then be an interface where the winding number changes, and at this point the band gap must close. The same phenomena applies given a finite system, where there must be an interface between the chain and vacuum. If the winding number is non zero in the chain, then at the edge the gap must close to form the interface. For the SSH model with its zero onsite potential, this results in zero-energy states at the edges.

In order to change the winding number, the path of the endpoint of $\boldsymbol{d}$ must be changed so that it wraps around the origin a different number of times. To do

this, the path can either i) be pulled across the origin by modifying parameters v, w or ii) lifting the path out of the $d_x d_y$ plane and placing it in a new position so that the origin is now enclosed/excluded. Method i) involves the path crossing through the origin, at which point the system enters a metallic phase, and method ii) means changing parameter d_z, which breaks chiral symmetry, as any finite d_z is not compatible with our definition of chiral symmetry, equation (2.5.1).

The winding number n_w is protected by the chiral symmetry of the system. Instead of the endpoint of $\boldsymbol{d}$ exploring the full three-dimensional spherical parameter space, it is restricted to a circle in the $d_x d_y$ plane, so the winding number will always be well-defined.

Solitons in the SSH Model

Any deviation from the usual order of hopping parameters in the SSH model can lead to interesting physical properties. These interruptions are known as solitons, an example soliton in the middle of an SSH chain is shown in figure 2.10.

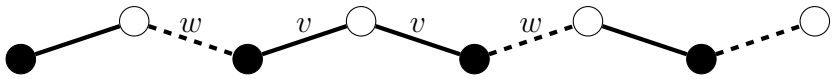

Figure 2.10: SSH chain with a fault in the centre. Between the second and third unit cells, the intracell v and intercell w hopping terms have swapped, and the new hopping texture continues for the remainder of the chain.

Solitons divide areas with different textures and each provide one additional topologically-protected low energy state. We consider two types of soliton: "sharp" and "smooth". A sharp soliton is defined by a sudden change in the parameter being modified, as shown in figure 2.10 - the order of hopping strength changes at the fault only, and the new ordering, or "texture", of hopping parameters will continue throughout the rest of the chain.

A soliton does not necessarily have to be atomically sharp (as in figure 2.10), but can instead be represented by a smooth texture. Often in numerics a tanh function will be used

$$\Delta_j = -\Delta_0 \tanh\left(\frac{j-m}{\xi}\right), \tag{2.6.17}$$

where j indexes the unit cells, Δ_0 is the difference between the hopping terms at the end of the chain (or far from the soliton centre), $\Delta_j = v_j - w_j$ is the difference

between hopping terms for each unit cell, m is the location of the soliton centre, and ξ is the soliton width. For the soliton to be in the centre of the system m must be an even number plus 1/2. The tanh function is shown in figure 2.11, this shows how the original parameter Δ_0 is modified on each atomic site. A smooth soliton involves a gradual decrease of the magnitude of the parameter being changed up to the soliton centre, then the change in texture occurs while the parameter is very small. After the order of parameters is swapped the magnitude of the parameter strength gradually increases back to its original value.

The elements of the real-space Hamiltonian (2.6.2) are modified according to

$$H_{i+1,i} = H_{i,i+1} = \begin{cases} t + \frac{1}{2}\Delta_j, & \text{for odd } j \\ t - \frac{1}{2}\Delta_j, & \text{for even } j, \end{cases} \tag{2.6.18}$$

where $t = (v + w)/2$ is the mean average of the original two hopping parameters.

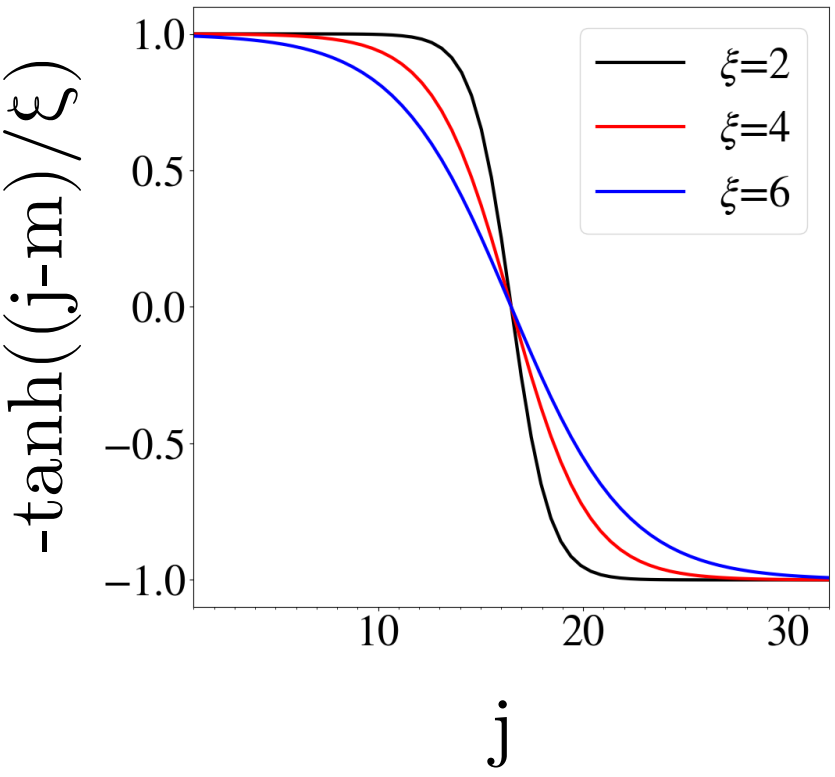

Figure 2.11: The negative tanh function (2.6.17) as a function of atomic position j. All results are for $N = 16$ unit cells (32 atoms) and the soliton centre is $m = 16.5$, in order to be in the centre of the system. The black curve shows a soliton width of $\xi = 2$, red shows $\xi = 4$, and blue shows $\xi = 6$.

Jackiw-Rebbi Mechanism

Solitons in the SSH model can be shown to host localised zero-energy states, as described by the Jackiw-Rebbi mechanism [72, 73]. We first find the continuum limit Hamiltonian by re-writing the Bloch Hamiltonian 2.6.6 in a different gauge

$$H_B^{\text{SSH}} = \begin{pmatrix} 0 & 2t\cos(ka/2) + i\Delta\sin(ka/2) \\ 2t\cos(ka/2) - i\Delta\sin(ka/2) & 0 \end{pmatrix}, \quad (2.6.19)$$

where $\Delta = v - w$ is the difference between the two hopping parameters, and t is the mean average hopping parameter, $t = (v + w)/2$. We make the substitution $k \to (\pi/a) + \hat{p}/\hbar$, where $\hat{p}$ is the momentum operator, in order to find the Hamiltonian in the continuum limit. The expansion is performed about $k = \pi/a$ because the band gap is located here. This substitution gives

$$H_c^{\text{SSH}} = \begin{pmatrix} 0 & v\hat{p} + i\Delta \\ v\hat{p} - i\Delta & 0 \end{pmatrix}, \quad (2.6.20)$$

where $v = at/\hbar$ is the velocity. The soliton profile of the hopping energies $\Delta(x)$ centered on $x = 0$ has limits given by

$$\lim_{x\to-\infty} \Delta(x) = -s\Delta_0; \quad \lim_{x\to\infty} \Delta(x) = s\Delta_0, \quad (2.6.21)$$

where $\Delta_0 > 0$ is the soliton strength at infinity, and the two textures are described by $s = \pm 1$. The specific soliton profile could be one of any number of functions, a straight line would suffice, or the tanh function described previously (2.6.17). For each texture, the localised zero-energy state is given by

$$\psi_s(x) = e^{-\frac{s}{\hbar v}\int_0^x \Delta(x')dx'} \begin{pmatrix} (1-s)/2 \\ (1+s)/2 \end{pmatrix}. \quad (2.6.22)$$

The column vector in (2.6.22) shows that the wavefunctions will be polarised, as it is an eigenstate of σ_z. The form of the soliton function Δ can be anything as long as it satisfies the boundary conditions (2.6.21).

Polarisation in the SSH model

We investigate the polarisation of the wavefunctions in the SSH model. Figures 2.12 and 2.13 show the amplitudes of the wavefunction ψ on each site within an SSH chain of $N = 16$ unit cells, with white and black bars representing the A and B sites, respectively. Figure 2.12 shows the chain in the topological phase, with $v < w$. In this case, especially for small values of v, the wavefunctions are almost fully localised on the ends of the chain, and towards the left and right ends of the chain the are fully localised on the A and B sublattices, respectively. While the system is fully polarised at the edges, the overall polarisation of the system is still $p_y = 0$. Figure 2.13 shows the amplitudes oft he same system, but this time in the topologically trivial phase, with $v > w$. In this case the zero-energy edge states are no longer present, and the edges are not polarised.

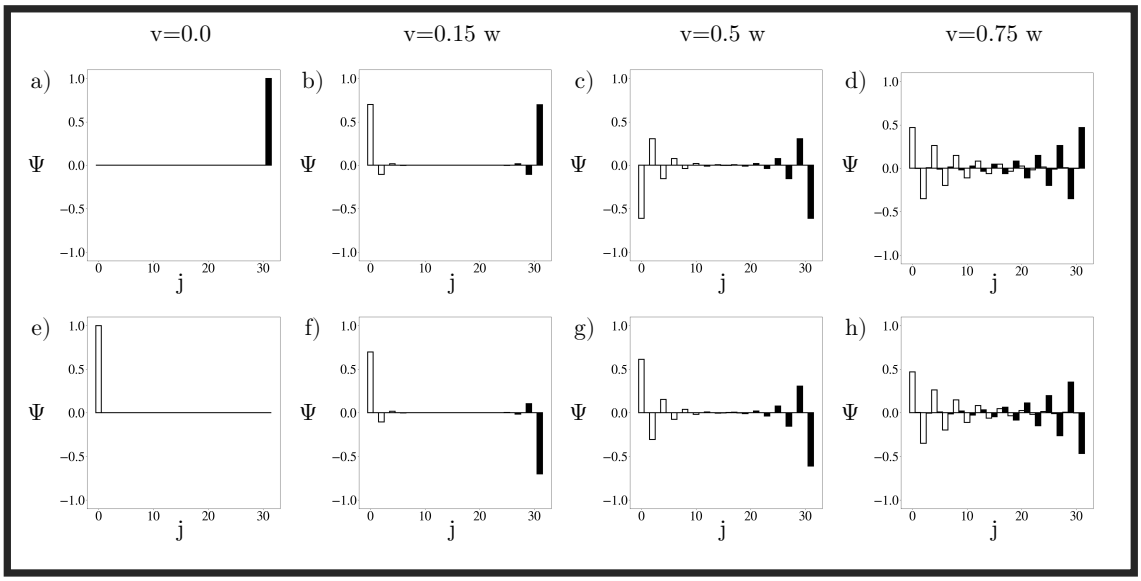

Figure 2.12: Wavefunction amplitudes of the two degenerate zero-energy states in an SSH chain of $N = 16$ unit cells. In each figure $v < w$ which means this shows the topological phase.

Previous work has shown that the low-energy edge states in the SSH model are topologically protected, and will remain gapless even in the presence of weak hopping disorder [1, 74–77], whereas onsite disorder will break the chiral symmetry and the edge states are no longer protected [1, 78].

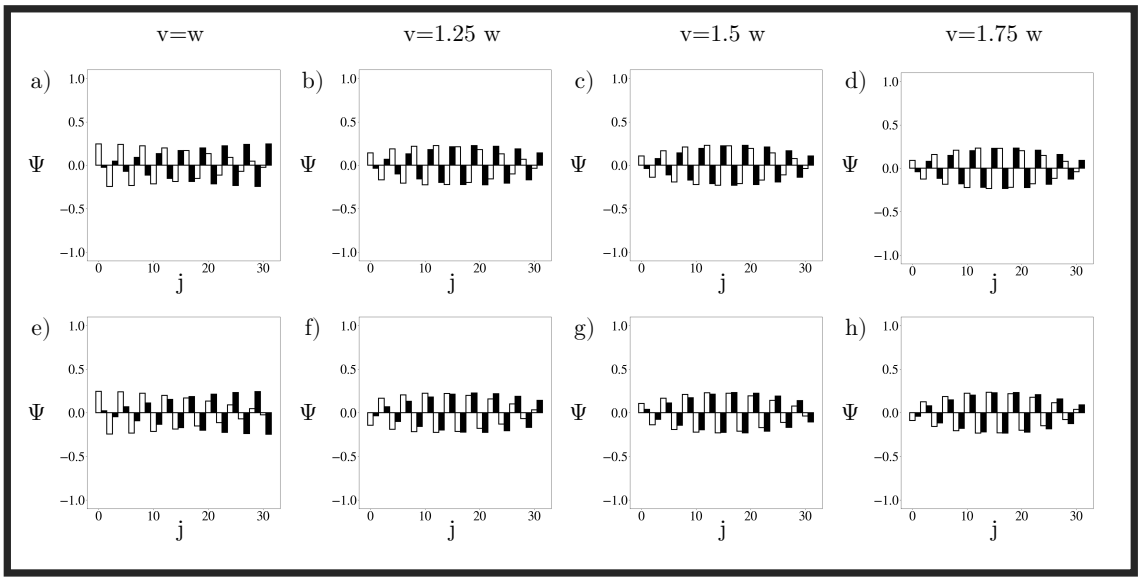

Figure 2.13: Wavefunction amplitudes of the two degenerate zero-energy states in an SSH chain of $N = 16$ unit cells. In each figure $v > w$ indicating that this is the topologically trivial phase.

2.7 Charge-Density-Wave Model

The Charge-Density-Wave (CDW) model is similar to the SSH model, but instead of alternating the hopping potentials, it alternates the sign of the onsite potential on each atom and has constant hopping t.

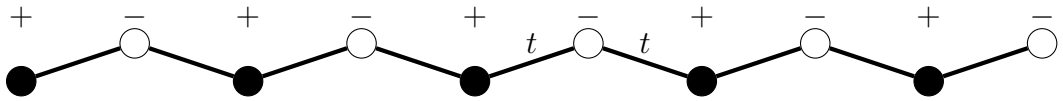

Figure 2.14: Diagram showing the Charge-Density-Wave (CDW) chain. Each unit cell contains two atoms; a black circle on sublattice A and a white circle on sublattice B. All hopping terms are the same (t) and the sign of the onsite potential alternates between lattice sites.

The real-space Hamiltonian is

$$\begin{aligned}\hat{H} = U\sum_{m=1}^{N}|x_{m,A},A\rangle\langle x_{m,A},A| - U\sum_{m=1}^{N}|x_{m,B},B\rangle\langle x_{m,B},B| \\ + \left[t\sum_{m=1}^{N}|x_{m,A},A\rangle\langle x_{m,B},B| + t\sum_{m=1}^{N-1}|x_{m,B},B\rangle\langle x_{m+1,A},A| + \text{h.c.}\right],\end{aligned} \tag{2.7.1}$$

where the first two summations describe the positive and negative onsite potentials of strength U on the A and B sites, respectively, and the inter- and intracall hopping is given by parameter t. The terms $|x_{m,A},A\rangle$ and $|x_{m,B},B\rangle$ represent states with atomic positions $x_{m,A} = ma$ and $x_{m,B} = (m+1/2)\,a$ on sublattices A and B respectively. h.c. represents the Hermitian conjugate. The real space Hamiltonian $\hat{H}$ 2.7.1 can be written using a matrix H as $\hat{H} = \Psi^{\dagger}H\Psi$, where Ψ is a column vector of atomic orbitals. For a chain of $N = 4$ unit cells the matrix H is

$$H = \begin{pmatrix} U & t & 0 & 0 & 0 & 0 & 0 & 0 \\ t & -U & t & 0 & 0 & 0 & 0 & 0 \\ 0 & t & U & t & 0 & 0 & 0 & 0 \\ 0 & 0 & t & -U & t & 0 & 0 & 0 \\ 0 & 0 & 0 & t & U & t & 0 & 0 \\ 0 & 0 & 0 & 0 & t & -U & t & 0 \\ 0 & 0 & 0 & 0 & 0 & t & U & t \\ 0 & 0 & 0 & 0 & 0 & 0 & t & -U \end{pmatrix}. \tag{2.7.2}$$

As in section 2.6 we use Fourier transforms in order to find the Bloch Hamiltonian, which, in the basis of the A and B sites, is

$$H_{\mathrm{CDW}} = \begin{pmatrix} U & 2t\cos\left(ka/2\right) \\ 2t\cos\left(ka/2\right) & -U \end{pmatrix}, \tag{2.7.3}$$

where $|U|$ is the magnitude of the alternating onsite potential, k is the wave vector, and a is the length of the lattice vector. This two-band Hamiltonian can be written in terms of the vector $\boldsymbol{d}$, with components

$$d_x\left(k\right) = 2t\cos\left(ka/2\right), \quad d_y\left(k\right) = 0, \quad d_z\left(k\right) = U. \tag{2.7.4}$$

The corresponding eigenvalues are

$$E_{\pm} = \pm|\boldsymbol{d}| = \pm\sqrt{U^2 + 4t^2\cos^2\left(ka/2\right)}, \tag{2.7.5}$$

these are plotted in figure 2.15. There is a band gap of $E_g = 2|U|$ located at $k = \pm\pi/a$, so for $U = 0$ the system is in a metallic phase.

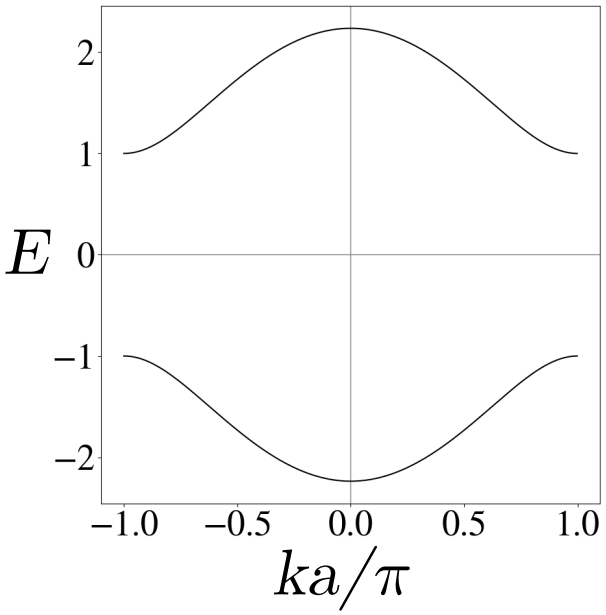

Figure 2.15: Dispersion relation of a CDW chain with $U = 1.0$, $t = 1$. The alternating onsite potential opens a band gap.

In this gauge, d_x is not 2π periodic, a closed loop is not formed, and a winding number cannot be defined. A different topological index has been proposed by

Shiozaki et. al. [79], which we will call μ_2. This $\mathbb{Z}_2$ topological index is defined by counting whether the trajectory crosses the negative d_x axis an even or odd number of times. If it is even, $\mu_2 = 0$, and if it is odd, $\mu_2 = 1$. Because d_x is not 2π periodic, the trajectory will not form a closed loop, but we know that the initial and final values of the d_x component must be equal, and that $d_y(2\pi) = -d_y(0)$. These two restrictions mean that it is impossible to change the topological index μ_2 via an adiabatic deformation. The distinction between the two phases is difficult to show with only nearest neighbour hopping parameters, so more details are given in appendix E.

The symmetries of the CDW model are shown in table 2.2. The chiral symmetry of the CDW model in reciprocal space is simply represented by σ_y. This only applies in the continuum limit - realised by an infinitely long chain of atoms, or a large loop with periodic boundary conditions. In real space the chiral symmetry of the CDW model is nonsymmorphic, this means that the symmetry requires the combination of a translation (by a vector that is not a primitive lattice vector) with either a mirror reflection or a rotation. The chiral symmetry of the CDW model in real space is represented by $S_y = T_{a/2}S_z$, where S_z is equation (2.5.7) and $T_{a/2}$ (2.7.6) describes translation by an atomic spacing $a/2$. This symmetry only holds for infinitely long systems. The combination of symmmetries found in this model mean it is in the nonsymmorphic symmetry class A1 [69, 71].

	k-space	position space
chiral	σ_y	$T_{a/2}S_z$
time	σ_0	I
charge	σ_y	$T_{a/2}S_z$
space	σ_0	P_0

Table 2.2: Symmetries of the charge density wave model in k-space and position space. σ_y and σ_0 are the Pauli matrices, and matrices $T_{a/2}$, S_z and P_0 are defined in section 2.5 as equations (2.7.6), (2.5.7), and (2.5.11).

$$T_{a/2} = \begin{pmatrix} 0 & 1 & 0 & 0 & \dots & 0 & 0 \\ 0 & 0 & 1 & 0 & \dots & 0 & 0 \\ 0 & 0 & 0 & 1 & \dots & 0 & 0 \\ 0 & 0 & 0 & 0 & \dots & 0 & 0 \\ \vdots & \vdots & \vdots & \vdots & \vdots & \vdots & \vdots \\ 0 & 0 & 0 & 0 & \dots & 0 & 1 \\ 1 & 0 & 0 & 0 & \dots & 0 & 0 \end{pmatrix}. \tag{2.7.6}$$

Solitons in the CDW Model

Solitons can be added to the CDW model by modifying the pattern of positive and negative onsite potenitals. A sharp soliton would be introduced by repeating the sign of the onsite potential, and continuing the pattern afterwards. This reverses the texture of the CDW chain, as for a finite chain with an even number of atoms, the first and last atom will now have the same sign of onsite potential.

A smooth soliton can be introduced in the same way as in section 2.6. We modify the onsite potential of each atom according to some function $U(x)$. Within each unit cell, j, the atom on sublattice A has onsite potential given by

$$U_{A,j} = -U_0 \tanh\left(\frac{j - m - 1/2}{\xi}\right), \tag{2.7.7}$$

and the corresponding B atom in the same unit cell has onsite potential $U_{B,j} = -U_{A,j}$. U_0 gives the magnitude of the soliton potential at $x = \pm\infty$, m gives the location of the soliton centre, and ξ is the soliton width.

Jackiw-Rebbi Mechanism

Solitons in the CDW model can be shown to host localised zero-energy states, as described by the Jackiw-Rebbi mechanism [72, 73]. We first find the continuum limit Hamiltonian by substituting $k \to (\pi/a) + \hat{p}/\hbar$ into the Bloch Hamiltonian 2.7.3, where $\hat{p}$ is the momentum operator. This gives

$$H_c = \begin{pmatrix} U(x) & v\hat{p} \\ v\hat{p} & -U(x) \end{pmatrix}, \tag{2.7.8}$$

where $v = at/\hbar$ is the velocity. The soliton profile of the onsite energies $U(x)$ centered on $x = 0$ has limits given by

$$\lim_{x\to-\infty} U(x) = -sU_0; \quad \lim_{x\to\infty} U(x) = sU_0, \tag{2.7.9}$$

where $U_0 > 0$ is the soliton strength at infinity, and the two textures are described by $s = \pm 1$. For each texture, the localised zero-energy state is given by

$$\psi_s(x) = e^{-\frac{s}{\hbar v}\int_0^x U(x')dx'} \begin{pmatrix} 1 \\ is \end{pmatrix}. \tag{2.7.10}$$

Polarisation in the CDW Model

We investigate the polarisation of the wavefunctions in the CDW model. Figures 2.16 and 2.17 show the amplitudes of the wavefunction ψ on each site within a CDW chain of $N = 16$ unit cells, with white and black bars representing the A and B sites, respectively. Figure 2.16 shows the chain for small values of the hopping parameter, t, and it shows that the wavefunctions are fully localised on the ends of the chain, as well as fully localised on the A or B sublattices. Figure 2.17 shows the amplitudes of the same system with larger values of the hopping parameter, t. In this case the system is no longer polarised on the A and B sublattices, nor polarised on the ends of the chain.

Previous work [72] has shown that although solitons in the CDW model will break the nonsymmorphic chiral symmetry, the polarisation of the soliton state will approach $p_y = 1$ for a large enough soliton width.

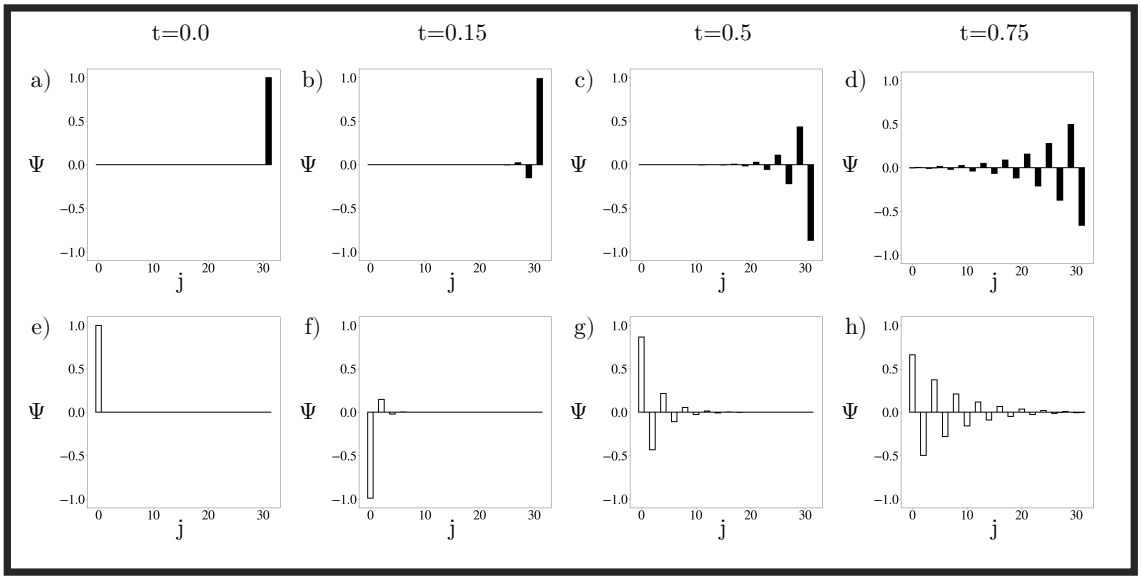

Figure 2.16: Wavefunction amplitudes of the two flat bands in a CDW chain of $N = 16$ unit cells for small values of the hopping parameter t. Figures a-d) corrrespond with the negative energy band at $E = -U$ and figures e-h) correspond with the positive energy band $E = U$.

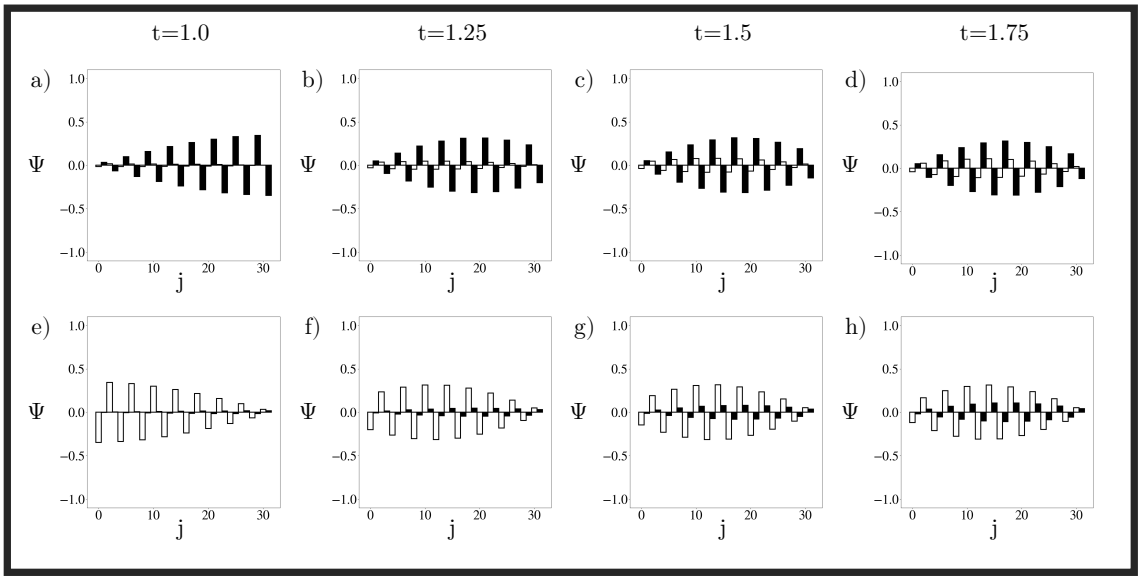

Figure 2.17: Wavefunction amplitudes of the two flat bands in a CDW chain of $N = 16$ unit cells for large values of the hopping parameter t. Figures a-d) corrrespond with the negative energy band at $E = -U$ and figures e-h) correspond with the positive energy band $E = U$.

2.8 Rice-Mele Model

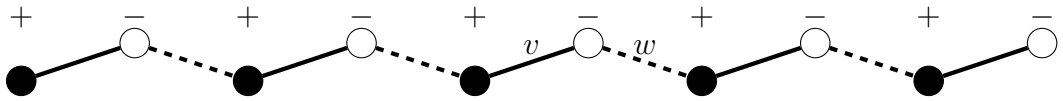

Figure 2.18: Diagram showing the Rice-Mele chain. Each unit cell contains two atoms; a black circle on sublattice A and a black circle on sublattice B. Atoms on sublattice A have a postive onsite potential energy, and atoms on sublattice B have a negative onsite potential energy. The alternating coupling strengths v and w are shown with solid and dashed lines, respectively.

The Rice-Mele model [80] can be seen as a combination of the two previous models - it is a one-dimensional chain of atoms with alternating hopping terms and alternating sign of the onsite potentials, as shown in figure 2.18. The Rice-Mele Hamiltonian in the basis of the A and B atomic sites is

$$H_{\mathrm{RM}} = \begin{pmatrix} U & ve^{ika/2} + we^{-ika/2} \\ ve^{-ika/2} + we^{ika/2} & -U \end{pmatrix}, \tag{2.8.1}$$

where v and w are the alternating hopping terms, U is the strength of the alternating onsite potentials, k is the wave vector, and $a/2$ is the atomic spacing - giving lattice vector length a. The components of the vector $\boldsymbol{d}$ are

$$d_x(k) = (v+w)\cos(ka/2), \quad d_y(k) = -(v-w)\sin(ka/2), \quad d_z(k) = U. \tag{2.8.2}$$

The corresponding eigenvalues are

$$E = \pm|\boldsymbol{d}| = \pm\sqrt{U^2 + v^2 + w^2 + 2vw\cos(ka)} \tag{2.8.3}$$

Given positive parameters U, v, w, the band gap will be at the edges of the Brillouin zone, with value $E_g = 2\sqrt{U^2 + v^2 + w^2 - 2vw}$.

The Rice-Mele model does not have chiral or charge conjugation symmetry, but does have time-reversal symmetry. It is in the symmetry class AI [69, 71].

In chapter 4 we will use dimensional reduction to relate our model of rhombohedral graphite to the Rice-Mele model.

2.9 Numerical Methods

In our research presented in Chapters 3 and 4 we calculate energy eigenvalues by numerically diagonalising tight-binding Hamiltonians similar to that of equation 2.4.16. The parameters chosen are those found experimentally for Bernal stacked bilayer graphene $\gamma_0 = 3.16$ eV, $\gamma_1 = 0.381$ eV [60], $a = 2.46$ Å[58]. The dispersion relations are shown in the vicinity of the Dirac point K_+, which has wave vector $\boldsymbol{K}_+ = (4\pi/3a, 0)$, and calculated using wave vector $\boldsymbol{k} = \boldsymbol{q} - \boldsymbol{K}_+$, with $\boldsymbol{k} = (k_x, k_y)$. The eigenvalues are calculated on a square grid of points centred on K_+. For low energies the dispersion relations are approximately isotropic about the Dirac point, so figures show the eigenvalues as functions of k_x only, with $k_y = 0$. The k_x axis is also normalised by the characteristic wave vector $k_c = \gamma_1/\hbar v$, where $\hbar v = \sqrt{3}a\gamma_0/2$ is the group velocity related to intralayer hopping. The density of states per unit energy per unit area, L^2, is calculated using a Lorentzian approximation with finite width δ_L,

$$g(E) = \frac{1}{\pi L^2} \sum_n \frac{\delta_L}{(E - E_n)^2 + \delta_L^2}. \tag{2.9.1}$$

Chapter 3

Solitons Due to Stacking Faults

3.1 Pristine Rhombohedrally-Stacked Graphite

Multilayer graphite systems with rhombohedral stacking can be modelled similarly to the SSH model, where the alternating hopping terms v and w are replaced by the intralayer hopping γ_0 and vertical interlayer hopping γ_1. The two triangular lattices lead to a two atom unit cell, which matches the two atom unit cell of the SSH model. Dimensional reduction describes the mapping of a problem from a higher to a lower dimension, and in this work we do this by setting a component of $\boldsymbol{k}$ to a fixed constant [71, 81, 82]. By using dimensional reduction the dispersion relation of rhombohedrally-stacked graphite can be directly compared to the dispersion relation of the SSH model, as shown in figure 3.1. There the eigenvalues of the SSH model are always equal to the eigenvalues of the graphite system, in units of its interlayer hopping γ_1. The critical momentum, $k_c = \gamma_1/\hbar v$, is the point where the intralayer hopping becomes equal to the interlayer hopping.

The Hamiltonian of N-layer rhombohedrally-stacked graphite in the minimal model (nearest-neighbour hopping only), and in the basis of all $2N$ atomic sites is

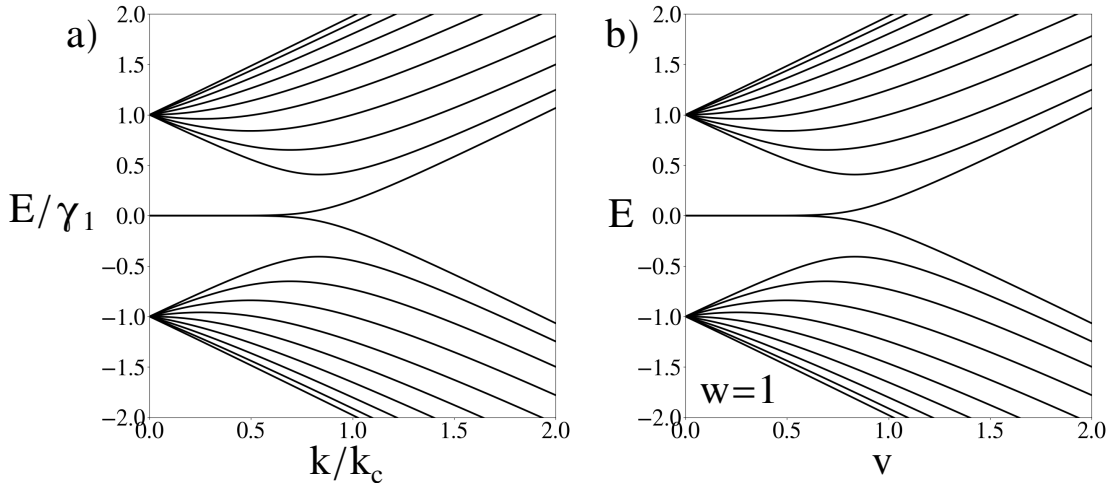

Figure 3.1: a) Dispersion relation near the K point for a rhombohedrally-stacked graphite system of $N = 10$ layers. The energy is given in units of interlayer hopping γ_1, and the momentum in terms of the critical momentum $k_c = \gamma_1/\hbar v$. Calculated using Hamiltonian (2.4.16) and the method and parameters outlined in section 2.9. b) Dispersion relation of an SSH chain of $N = 10$ unit cells. Calculated using Hamiltonian (2.6.2).

given in equation (2.4.16)

$$H = \begin{pmatrix} D & V & 0 & 0 & \dots \\ V^\dagger & D & V & 0 & \dots \\ 0 & V^\dagger & D & V & \dots \\ 0 & 0 & V^\dagger & D & \dots \\ \vdots & \vdots & \vdots & \vdots & \ddots \end{pmatrix}, \tag{2.4.16}$$

where the 2×2 matrix blocks are

$$D = \begin{pmatrix} 0 & v\pi^\dagger \\ v\pi & 0 \end{pmatrix}, \quad V = \begin{pmatrix} 0 & 0 \\ \gamma_1 & 0 \end{pmatrix}, \quad \pi = \hbar\left(\xi k_x + i k_y\right). \tag{3.1.1}$$

$\xi = \pm 1$, depending on if the momentum is being calculated relative to a K or K' point, $\hbar$ is the reduced Planck's constant, and v is the group velocity. The matrix block D describes hopping within one graphene sheet, and matrix block V describes hopping between layers n and $n+1$, with the γ_1 term specifying the hopping between atomic sites B_n on layer n and A_{n+1} of the layer above.

We find dispersion relations and density of states throughout this chapter using

the methods in section 2.9, and the Hamiltonians used are specified in each figure.

The behaviour of the low energy states can be analysed by forming a low energy effective Hamiltonian using the method described in 2.4.4. For pristine rhombohedrally-stacked multilayer graphite the effective Hamiltonian (3.1.2) is in the basis of the edge states $\psi_{A,1}$ and $\psi_{B,N}$ only, and they are weakly coupled with strength decreasing with the number of layers, N.

$$H^{\text{eff}} = -\gamma_1 \begin{pmatrix} 0 & \left(-\kappa^\dagger\right)^N \\ (-\kappa)^N & 0 \end{pmatrix}. \tag{3.1.2}$$

Here $\kappa = (\xi k_x + i k_y)/k_c$ and $\kappa^\dagger = (\xi k_x - i k_y)/k_c$. This gives the simple eigenvalues near the K point

$$\epsilon = \pm\gamma_1 (k/k_c)^N . \tag{3.1.3}$$

Equation (3.1.3) shows that for a large number of layers N, the states are at zero energy for $k < k_c$. For $k > k_c$ the energies are dispersive. Figure 3.2a) shows the dispersion relation for $N = 16$ layers of rhombohedrally-stacked graphite. We show numerical results with black lines and plot the analytical expression 3.1.3 with blue dashed lines. This figure shows that our analytical expression for the low-energy states shows good agreement with the numerical results for $k < k_c$. The density of states plot 3.2b) shows a sharp peak at $E = 0$, corresponding with the flat bands in the dispersion.

We consider two types of stacking faults in rhombohedrally-stacked graphite [1, 83–85]. Figure 3.3 a) shows a diagram of the usual rhombohedral stacking. Figure 3.3 b) shows the stacking interrupted by a Bernal fault, where the usual ABC order is swapped for a short ABA section. Figure 3.3 c) show a twin-boundary fault in rhombohedral graphite, where two ABC sections are connected via one of the layers, but otherwise do not follow the same stacking structure. Both types of stacking fault act as domain walls separating two graphite sections, which we will explore in the rest of this chapter.

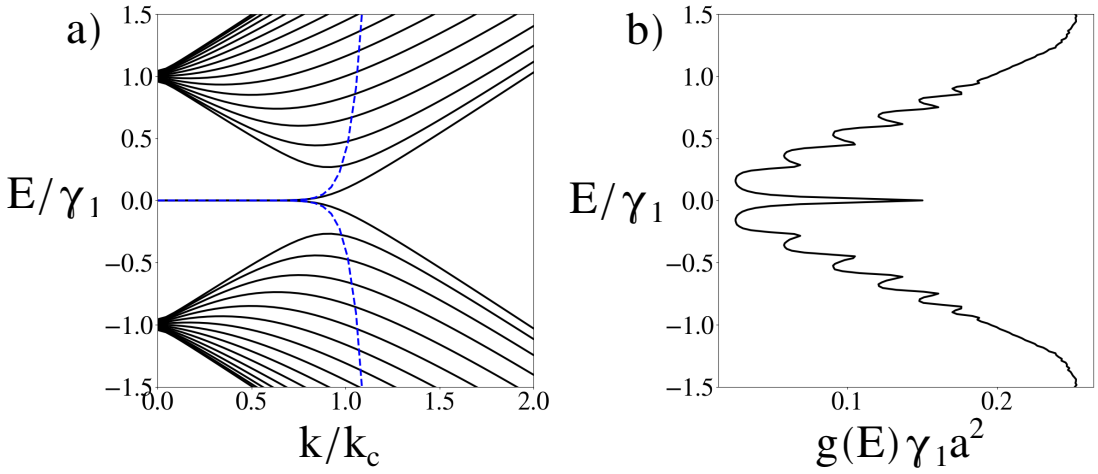

Figure 3.2: Dispersion relation (a) and density of states (b) for $N = 16$ layers of pristine rhombohedrally-stacked graphite. The numerics are plotted using black lines and the analytical expressions (3.1.3) are plotted in blue dashed lines. Numerics found using Hamiltonian 2.4.16. Parameters used are $\gamma_0 = 3.16$ eV, $\gamma_1 = 0.381$ eV [60], and $a = 2.46$ Å[58]. The Lorentzian width used is $\delta_L = 0.01\gamma_1$.

3.2 Graphite with a Bernal Fault

The first type of stacking fault considered here is the Bernal fault, shown in figure 3.3b). We define stacking faults via two integers (m, n), with m being the number of layers before the faults and n the number of layers after the fault, such that the total number of layers N is $N = m + n$. As an example, figure 3.3b)shows a $(3, 5)$ Bernal fault. This fault acts as a boundary, or domain wall, between two regularly-stacked RG sections. The low-energy properties can be simply seen by imagining the intralayer coupling $k \to 0$. In this regime the system forms vertically-connected dimer pairs, and the four remaining monomers form the low-energy states. These states are localised on the top and bottom edge states, and the two sites either side of the fault that do not directly couple to an adjacent layer. The full $2N \times 2N$ Hamiltonian, H_B, is formed similarly to (2.4.16), but with slightly different interlayer connections either side of the fault.

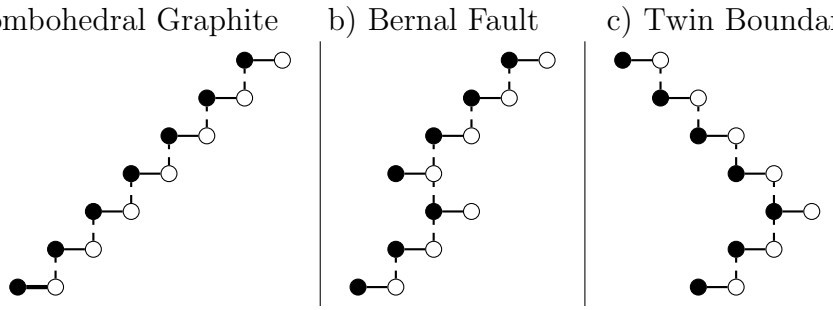

Figure 3.3: Diagram of the side view of a pristine rhombohedral graphene lattice, a single Bernal stacking fault, and a single twin boundary stacking fault. The filled and open circles represent the atoms on the A and B sublattices, respectively. Horizontal lines represent the intralayer coupling γ_0 and vertical lines represent the interlayer coupling γ_1.

$$H_B = \begin{pmatrix} \ddots & \vdots & \vdots & \vdots & \vdots & \iddots \\ \dots & D & V & 0 & 0 & \dots \\ \dots & V^\dagger & D & V^\dagger & 0 & \dots \\ \dots & 0 & V & D & V & \dots \\ \dots & 0 & 0 & V^\dagger & D & \dots \\ \iddots & \vdots & \vdots & \vdots & \vdots & \ddots \end{pmatrix}, \tag{3.2.1}$$

where the 2×2 matrix blocks are the same as previously

$$D = \begin{pmatrix} 0 & v\pi^\dagger \\ v\pi & 0 \end{pmatrix}, \quad V = \begin{pmatrix} 0 & 0 \\ \gamma_1 & 0 \end{pmatrix}, \quad \pi = \hbar\left(\xi k_x + i k_y\right). \tag{3.2.2}$$

The stacking faults each contribute two additional low energy states, as shown in the dispersion relation 3.4 a). We can form a low-energy effective Hamiltonian in the basis of the now four low-energy states. For the Bernal fault the effective Hamiltonian is in the basis $\psi_{A,1}$, $\psi_{B,m}$, $\psi_{A,m+1}$, $\psi_{B,N}$.

$$H^{m,n}_{\text{Bernal}} = \begin{pmatrix} 0 & -\left(-\kappa^\dagger\right)^m & 0 & \left(-\kappa^\dagger\right)^{m+n-2} \\ -\left(-\kappa\right)^m & 0 & -c_{mn}\left(k/k_c\right)^{2(l-1)}\kappa^2 & 0 \\ 0 & -c_{mn}\left(k/k_c\right)^{2(l-1)}\left(\kappa^\dagger\right)^2 & 0 & -\left(-\kappa^\dagger\right)^n \\ \left(-\kappa\right)^{m+n-2} & 0 & -\left(-\kappa\right)^n & 0 \end{pmatrix} \tag{3.2.3}$$

where $c_{mn} = \left(1 + \delta_{mn}\right)/2$ and $l = \min\left(m, n\right)$, and only the leading term in k/k_c has been kept for the nonzero elements between A and B sites. Note that k is the

magnitude of the wavevector (meaning k/k_c is the magnitude of the corresponding κ) while κ is the vector containing k_x and k_y components. The Hamiltonian (3.2.3) has chiral symmetry, so all matrix elements between two A sites or between two B sites are zero [1]. The eigenvalues of this Hamiltonian are

$$\begin{aligned}
(E/\gamma_1)^2 &= \frac{1}{2}\beta_B\left(k/k_c\right) \pm \frac{1}{2}\sqrt{\beta_B^2\left(k/k_c\right) - 4\eta_B\left(k/k_c\right)}, \\
\beta_B\left(x\right) &= x^{2m} + x^{2n} + x^{2m+2n-4} + c_{mn}^2 x^{4l}, \\
\eta_B\left(x\right) &= x^{2m+2n} + 2c_{mn}x^{2m+2n+2l-2} + c_{mn}^2 x^{2m+2n+4l-4}.
\end{aligned} \tag{3.2.4}$$

These eigenvalues are shown as blue dashed lines in figure 3.4a), and show strong agreement with the full numerical calculation for $k < k_c$. As in figure 3.2, the density of states plot shows a peak at $E = 0$, corresponding to the flat bands in the dispersion relation.

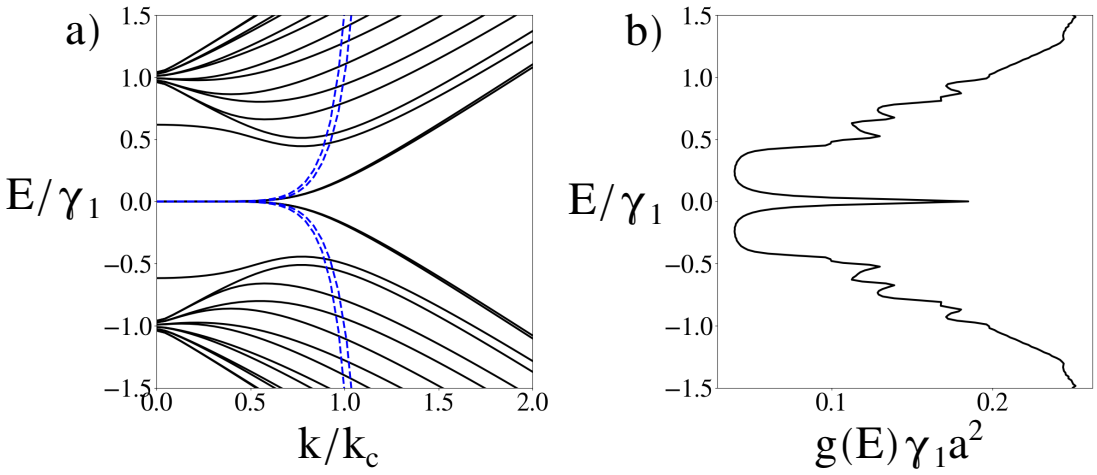

Figure 3.4: Dispersion relation (a) and density of states (b) for $N = 16$ layers of rhombohedrally-stacked graphite with a Bernal stacking fault in the centre. The numerics are plotted using black lines and the analytical expressions (3.2.4) are plotted in blue dashed lines. Numerics found using Hamiltonian 3.2.1. Parameters used are $\gamma_0 = 3.16$ eV, $\gamma_1 = 0.381$ eV [60], and $a = 2.46$ Å[58]. The Lorentzian width used is $\delta_L = 0.01\gamma_1$.

Figure 3.4a) shows the dispersion relation of $N = 16$ layers of RG with a Bernal stacking fault in the centre. There are four zero-energy states for $k < k_c$, and these lead to a sharp peak in the density of states, shown in figure 3.4b).

3.3 Graphite with Twin-Boundary Fault

The second stacking fault is called a twin-boundary fault, and is shown in the third section of figure 3.3. Here the low energy states are the edges, the monomer site at the fault, and the odd combination of the trimer at the fault. The full Hamiltonian, H_T, can be found by swapping the interlayer coupling blocks for all layers following the stacking fault.

$$H_T = \begin{pmatrix} \ddots & \vdots & \vdots & \vdots & \vdots & \iddots \\ \dots & D & V & 0 & 0 & \dots \\ \dots & V^\dagger & D & V^\dagger & 0 & \dots \\ \dots & 0 & V & D & V^\dagger & \dots \\ \dots & 0 & 0 & V & D & \dots \\ \iddots & \vdots & \vdots & \vdots & \vdots & \ddots \end{pmatrix}, \tag{3.3.1}$$

where the 2×2 matrix blocks are the same as previously

$$D = \begin{pmatrix} 0 & v\pi^\dagger \\ v\pi & 0 \end{pmatrix}, \quad V = \begin{pmatrix} 0 & 0 \\ \gamma_1 & 0 \end{pmatrix}, \quad \pi = \hbar\left(\xi k_x + i k_y\right). \tag{3.3.2}$$

Again, an effective Hamiltonian can be found in the basis of low-energy states, which is: $\psi_{A,1}$, $\left(\psi_{B,m-1} + \psi_{B,m+1}\right)/\sqrt{2}$, $\psi_{B,m}$, $\psi_{A,N}$.

$$H^{m,n}_{\text{twin}} = \gamma_1 \begin{pmatrix} 0 & -\left(-\kappa^\dagger\right)^{m-1}/\sqrt{2} & 0 & -\left(-\kappa^\dagger\right)^{m}/2 \\ -\left(-\kappa\right)^{m-1}/\sqrt{2} & 0 & \left(-\kappa\right)^{n-1}/\sqrt{2} & 0 \\ 0 & \left(-\kappa^\dagger\right)^{n-1}/\sqrt{2} & 0 & -\left(-\kappa^\dagger\right)^{m}/2 \\ -\left(-\kappa\right)^{m}/2 & 0 & -\left(-\kappa\right)^{n}/2 & 0 \end{pmatrix} \tag{3.3.3}$$

The eigenvalues of this are given by

$$\begin{aligned} \left(E/\gamma_1\right)^2 &= \frac{1}{2}\beta_t\left(k/k_c\right) \pm \frac{1}{2}\sqrt{\beta_t^2\left(k/k_c\right) - 4\eta_t\left(k/k_c\right)}, \\ \beta_t\left(x\right) &= \frac{1}{2}\left(x^{2m-2} + x^{2n-2}\right) + \frac{1}{4}\left(x^{2m} + x^{2n}\right) \\ \eta_t\left(x\right) &= \frac{1}{2}\left(x^{2m+2n-2}\right) \end{aligned} \tag{3.3.4}$$

The dispersion relations found from both analytical expressions and numerical calculation for $N = 16$ layers of RG with a twin boundary fault are shown in figure 3.5 a). Here the analytical expressions (blue dashed lines) show good agreement with the numerics for small values of k/k_c. There are four zero-energy states for $k < k_c$, and these lead to a sharp peak in the density of states at zero energy. The dispersion relation behaves similarly to that of the system with a Bernal fault, but there is a slightly larger separation between the two positive and two negative bands, respectively, and this separation stays constant for $k > k_c$.

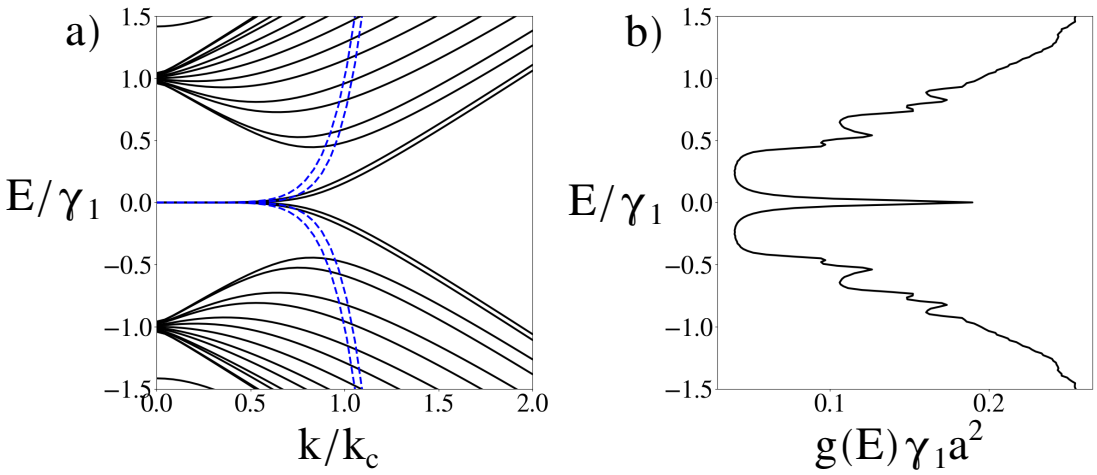

Figure 3.5: Dispersion relation (a) and density of states (b) for $N = 16$ layers of rhombohedrally-stacked graphite with a twin-boundary stacking fault in the centre. The numerics are plotted using black lines and the analytical expressions (3.3.4) are plotted in blue dashed lines. Numerics found using Hamiltonian 3.3.1. Parameters used are $\gamma_0 = 3.16$ eV, $\gamma_1 = 0.381$ eV [60], and $a = 2.46$ Å[58]. The Lorentzian width used is $\delta_L = 0.01\gamma_1$.

3.4 Disorder

The presence of flat bands at zero energy creates a sharp peak in the density of states. In this section, we investigate how robust this peak is in the presence of disorder. In particular, the Hamiltonians posses chiral symmetry as can be seen by examining the low-energy Hamiltonians (3.1.2), (3.2.3), and (3.3.3). We consider two types of disorder: onsite energy disorder and interlayer hopping disorder. The former breaks chiral symmetry and the latter preserves it.

We investigate the band gap, E_g, of the three graphene systems described above in the presence of both types of disorder. The first type of disorder modifies the layer energies. For disorder of strength δ the magnitude of the diagonal elements of the Hamiltonian H_{A_n,A_n} and H_{B_n,B_n} are increased by δ_n for $n = 1, 2, \ldots, N$, where the δ_n take uniformly distributed random values in the range $[-\delta, \delta]$. The second type of disorder modifies the interlayer coupling γ_1. The coupling elements $H_{B_n,A_{n+1}} = H_{A_{n+1},B_n} = \gamma_1 + \delta_n$ for $n = 1, 2, \ldots, N-1$, where the δ_n take uniformly distributed values in the range $[-\delta, \delta]$.

We have defined the band gap, E_g, as the separation of the low-energy states. The mean values of the band gap for faultless RG, a Bernal fault, and a twin-boundary fault are given as a function of disorder strength δ in figure 3.6. Results for random layer energies are plotted with crosses and random interlayer hopping energies are plotted with circles. The band gaps are the average over twenty different realisations of disorder. All three parts of figure 3.6 show that the band gap of the RG systems are unaffected by interlayer disorder, and slightly increase in the presence of random layer energies.

The disorder-averaged density of states for all three systems with random layer energies are shown in figure 3.7. The first column shows the density of states without disorder ($\delta = 0.0$), the second colunm shows the average of twenty realisations of disorder with a strength of $\delta = 0.1\gamma_1$, and the third column has a disorder strength of $\delta = 0.2\gamma_1$. The density of states initially shows a sharp peak at zero energy, which is due to the highly-localised flat edge states in the band structure. There are also smaller peaks due to the minima of the conduction bands and maxima of the valence bands. With weak disorder applied to the onsite energies of each layer, the

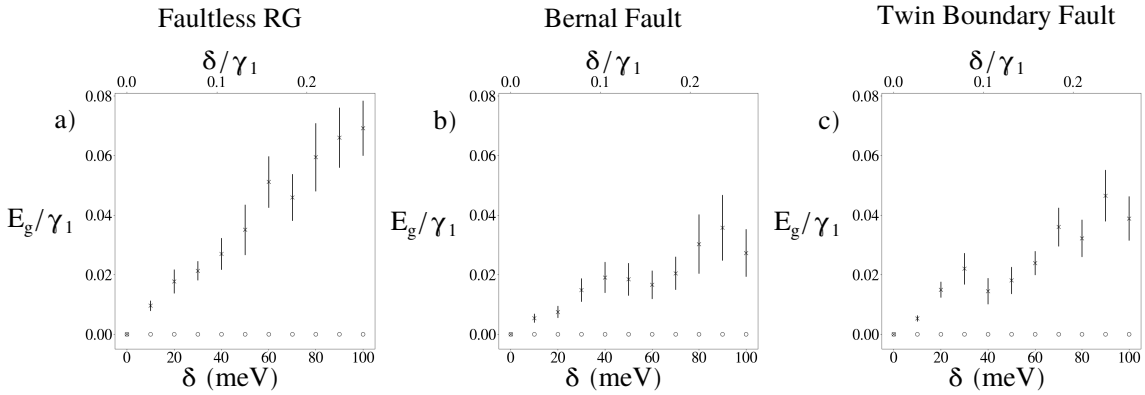

Figure 3.6: The disorder-averaged band gaps (in units of γ_1) for (a) faultless RG (b) a Bernal fault and (c) a twin-boundary fault as a function of disorder strenth δ. Crosses show the random layer energies and circles show the random interlayer hopping energies. All points are the mean average of twenty different realisations of disorder, and error bars give the standard error. The upper x-axis shows the disorder strength in units of γ_1.

density of states loses its defining features, and the peak at zero energy is completely destroyed. When the disorder strength is further increased, almost all features of the density of states are lost.

The disorder-averaged density of states for all three RG systems with random interlayer coupling energies are shown in figure 3.8. The left column is the same as that of figure 3.7 - the density of states with no disorder applied. The second column shows the systems with interlayer disorder of strength $\delta = 0.1\gamma_1$, and the third shows a disorder strength of $\delta = 0.2\gamma_1$. The increases in disorder strength acts only to smooth the small peaks in the conductance and valence bands, but the near-zero-energy peak is robust to this disorder.

To understand why the three RG systems are all robust to interlayer disorder, but not to onsite energy disorder, we must return to the low energy effective Hamiltonians (3.1.2), (3.2.3), and (3.3.3). In each of these, the energies of the edge states appear along the diagonal elements, so any disorder applied to these states will directly affect the eigenvalues of the system. The interlayer coupling appears in the off diagonal elements of these Hamiltonians as $H_{A1,BN} = -\gamma_1 (-\kappa)^N$ in (3.1.2), and the lowest power for a Bernal fault would be $-(-\kappa)^l$ (3.2.3), or for a twin-boundary fault $-(-\kappa)^{l-1}$ (3.3.3). This means that the coupling between either opposing surface states, or the coupling between a surface and a fault state is a product of each disorder parameter between the two. For $N \gg 1$, the system will self-average so

that the effect of any single interlayer disorder parameter δ_n on the low-energy bands will be negligible.

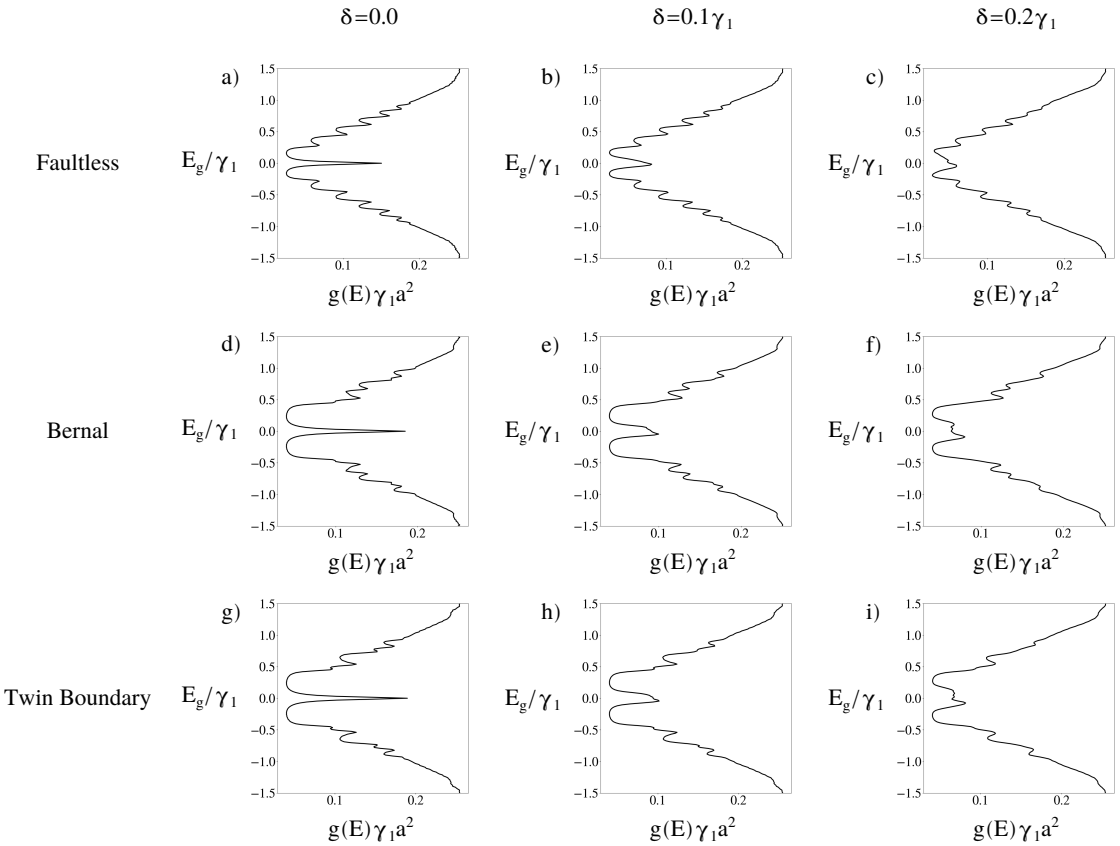

Figure 3.7: The disorder averaged density of states for $N = 16$ layers of faultless RG (top row), RG with a Bernal stacking fault in the centre (middle row), and RG with a twin-boundary fault in the centre (bottom row). The left column shows the density of states of each system, then the middle and right columns show the disorder-averaged density of states for $\delta = 0.1\gamma_1$ and $0.2\gamma_1$, respectively. Disorder is applied to the onsite energies and each disorder-averaged calculation is averaged over twenty realisations of disorder.

In our model of disordered rhobohedral graphite we have assumed translational invariance within each graphene plane. This is necessary in order to find a k-space Hamiltonian using Bloch's theorem. In order to fully analyse disorder within graphene would take a much greater computational effort, as modelling localised disorder in graphene requires the use of position space Hamiltonians, and the Hamiltonian matrices would become very large when modelling large enough graphene sheets and the matrix size would also need to be multiplied by the number of layers used.

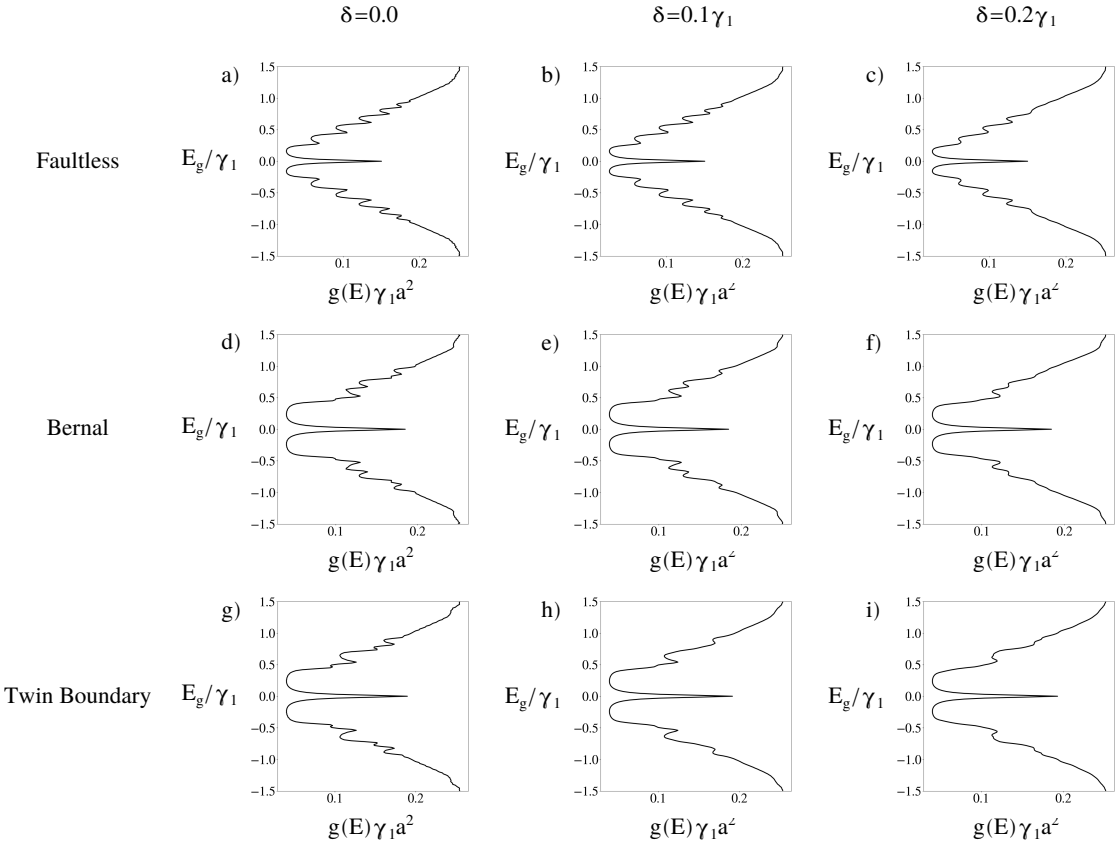

Figure 3.8: The disorder averaged density of states for $N = 16$ layers of faultless RG (top row), RG with a Bernal stacking fault in the centre (middle row), and RG with a twin-boundary fault in the centre (bottom row). The left column shows the density of states of each system, then the middle and right columns show the disorder-averaged density of states for $\delta = 0.1\gamma_1$ and $0.2\gamma_1$, respectively. Disorder is applied to the interlayer coupling energies and each disorder-averaged calculation is averaged over twenty realisations of disorder.

3.5 Finite Onsite Potential U

Graphene systems will usually have zero onsite potential U, but the following investigation can be applied to a honeycomb lattice with two different atomic species, such hexagonal boron nitride [2, 26] and other materials described in the introduction.

An interaction-induced band gap was investigated in our paper [1]. The effects of this can be mimicked using a single particle gap acting via a staggered potential. The gap parameters are given in the paper but here they are added to the diagonal terms of the Hamiltonian phenomenologically.

$$H = \begin{pmatrix} D & V & 0 & 0 & \dots \\ V^\dagger & D & V & 0 & \dots \\ 0 & V^\dagger & D & V & \dots \\ 0 & 0 & V^\dagger & D & \dots \\ \vdots & \vdots & \vdots & \vdots & \ddots \end{pmatrix}, \tag{3.5.1}$$

where the 2×2 matrix blocks are

$$D = \begin{pmatrix} U & v\pi^\dagger \\ v\pi & -U \end{pmatrix}, \quad V = \begin{pmatrix} 0 & 0 \\ \gamma_1 & 0 \end{pmatrix}, \quad \pi = \hbar\left(\xi k_x + i k_y\right). \tag{3.5.2}$$

The alternating onsite potentials $\pm U$ act to open a band gap of $2U$. The onsite values are added to Hamiltonians (3.2.1) and (3.3.1) similarly.

Figure 3.9 shows the dispersion relations and density of states for faultless RG, RG with a Bernal fault in the centre, and RG with a twin-boundary fault in the centre, all with onsite potentials $U = 0.1\gamma_1$. Figure 3.9 a) shows that the finite onsite potential acts to open a gap between the two zero-energy states, which remain as flat bands for $k < k_c$, and become dispersive for $k > k_c$ as in figure 3.2. The corresponding density of states plot, figure 3.9 d) shows pronounced peaks that correspond with the zero energy states, at energies $E = \pm U$.

Figure 3.9 b) and e) show the dispersion relation and density of states for RG with a Bernal fault in the centre. In this case, there are four flat bands for $k < k_c$, and the additional flat bands lead to an increase in the size of the peaks in the density of states, again at energies $E = \pm U$.

Figure 3.9 c) and f) show the dispersion relation and density of states for RG with a twin-boundary fault in the centre. In the same way as for the Bernal fault, there are four flat bands for $k < k_c$, and the additional flat bands lead to an increase in the size of the peaks in the density of states, again at energies $E = \pm U$.

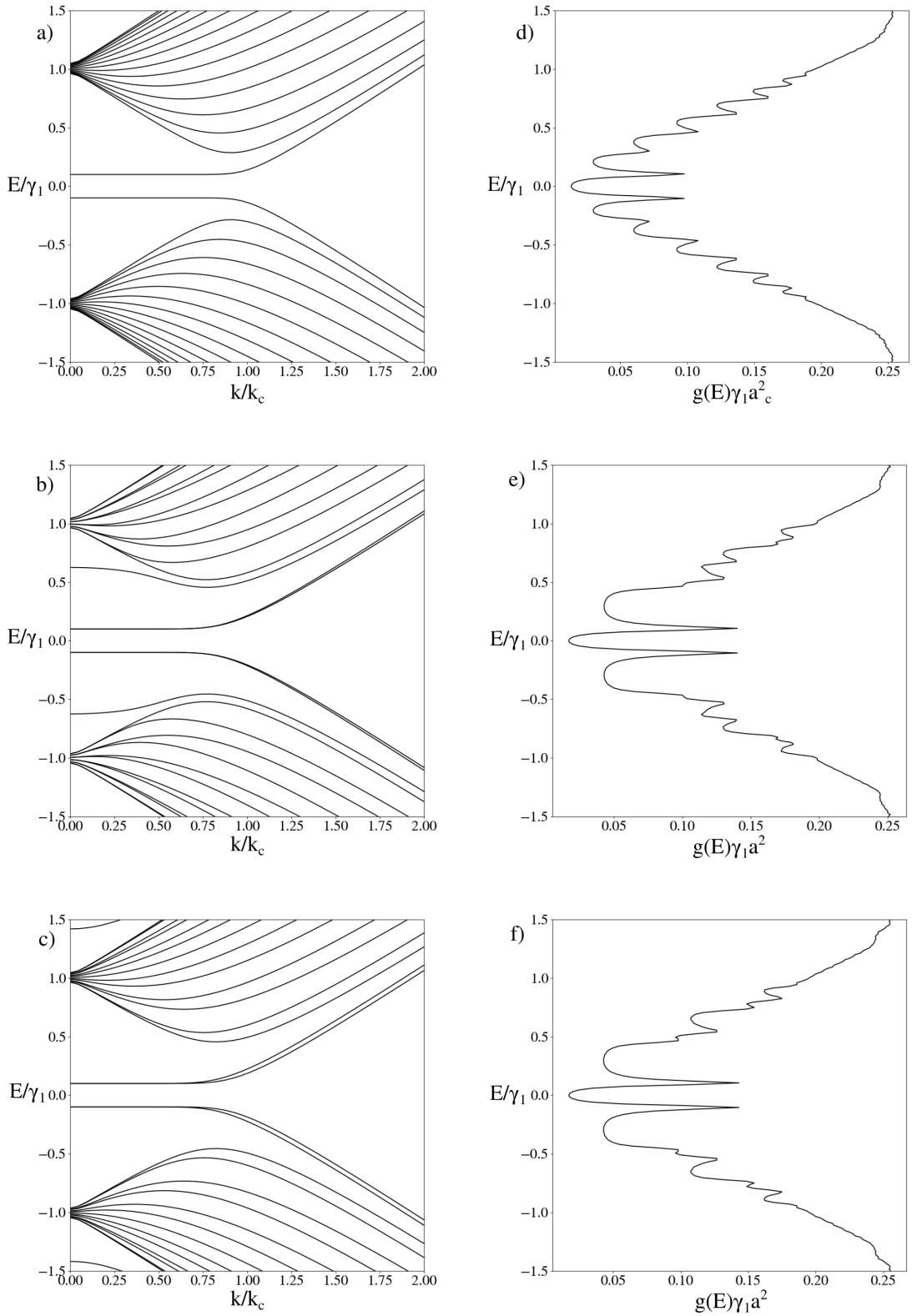

Figure 3.9: Dispersion relations and density of states for $N = 16$ layers of RG with a stacking fault in the centre, and with alternating onsite of magnitude $U = 0.1\gamma_1$. a,d) show no stacking fault, b,e) show a Bernal fault, c,f) show a twin-boundary fault.

3.6 Disorder with Finite U

Disorder is added in the same way as in section 3.4. We first investigate the band gap in the presence of disorder, and then the disorder-averaged density of states. As compared with our investigation of disorder in section 3.4, the presence of finite onsite potential U will break chiral symmetry.

Figure 3.10 shows the band gap, E_g, as a function of both interlayer and onsite energy disorder. With a finite separation of the bands, $U = 0.1\gamma_1$, the gap is initially at $2U$, but with increasing onsite disorder the band gap decreases. However, as before, the band gap is unaffected by the increasing interlayer disorder.

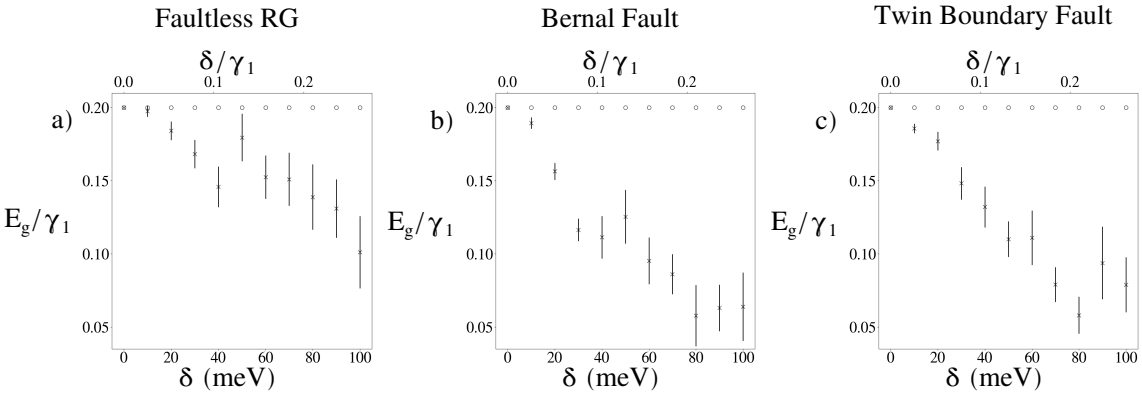

Figure 3.10: The disorder averaged band gaps (in units of γ_1) for (a) faultless RG (b) a Bernal fault and (c) a twin-boundary fault as a function of disorder strenth δ. The onsite potential is $U = 0.1\gamma_1$. Results for random layer energies are plotted with crosses and results for random interlayer hopping energies are plotted with circles. All points are the mean average of twenty different realisations of disorder, and error bars give the standard error. The upper x-axis shows the disorder strength in units of γ_1.

Similarly to the disorder-averaged density of states calculations shown in section 3.4, figure 3.11 shows that the onsite disorder acts to remove all sharp features from the density of states plots. Figure 3.12 shows that only the smaller peaks in the conduction and valence bands are smoothed by the addition of interlayer hopping disorder, but the sharp peaks at $E/\gamma_1 = \pm U$ are resistant to the effects of disorder.

Even though the presence of U breaks chiral symmetry, the low-energy states remain robust in the presence of interlayer hopping disorder. Thus, we don't attribute this behaviour to symmetry-protected topology, but simply to the self-averaging argument, as described at the end of section 3.4.

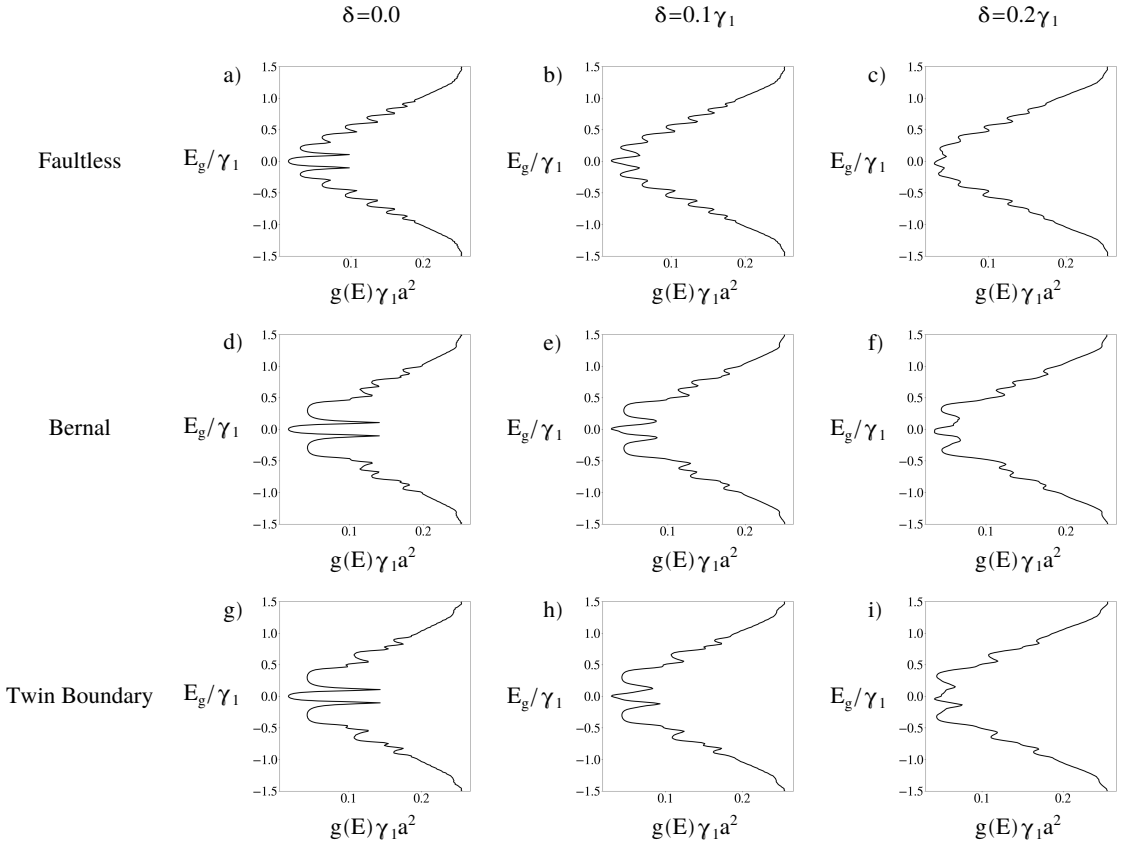

Figure 3.11: The disorder averaged density of states for $N = 16$ layers of faultless RG (top row), RG with a Bernal stacking fault in the centre (middle row), and RG with a twin-boundary fault in the centre (bottom row). In each case the initial onsite energy $U = 0.1\gamma_1$ The left column shows the density of states of each system, then the middle and right columns show the disorder-averaged density of states for $\delta = 0.1\gamma_1$ and $0.2\gamma_1$, respectively. Disorder is applied to the onsite energies and each disorder-averaged calculation is averaged over twenty realisations of disorder.

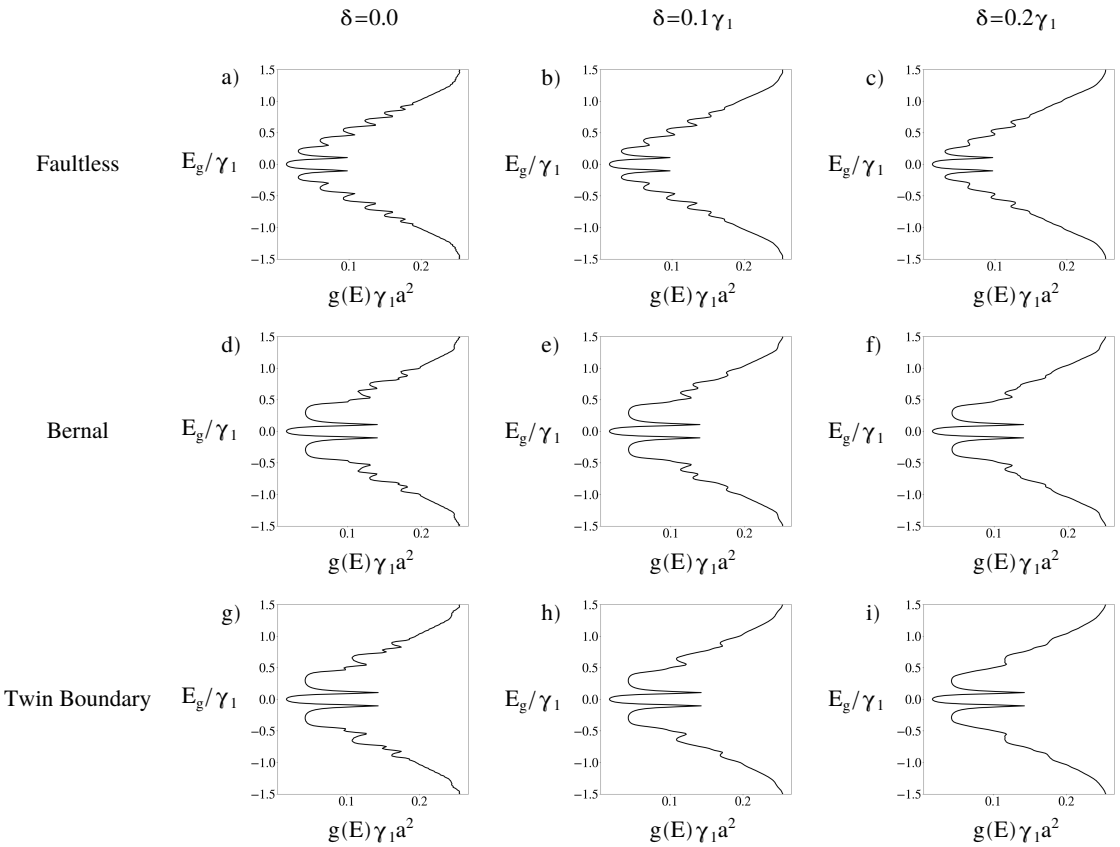

Figure 3.12: The disorder averaged density of states for $N = 16$ layers of faultless RG (top row), RG with a Bernal stacking fault in the centre (middle row), and RG with a twin-boundary fault in the centre (bottom row). In each case the initial onsite energy $U = 0.1\gamma_1$ The left column shows the density of states of each system, then the middle and right columns show the disorder-averaged density of states for $\delta = 0.1\gamma_1$ and $0.2\gamma_1$, respectively. Disorder is applied to the interlayer coupling energies and each disorder-averaged calculation is averaged over twenty realisations of disorder.

3.7 Polarisation

As described in section 2.6, the chiral symmetry of the SSH model is described by the S_z operator.

We find that for RG systems with onsite potential $U = 0$, the polarisation $p_z = \langle\psi|S_z|\psi\rangle$ of the low energy states is zero for all values of k_x. This result is the same for the faultless, Bernal fault, and Twin-Boundary fault systems. To better understand this result, we inspect the amplitudes of the wavefunctions in figures 3.13, 3.14, and 3.15.

For figures 3.13, 3.14, and 3.15a)-d) the wavevector $k = 0$, and there can be no hybridisation between states. The wavefunction amplitudes of the low energy states are then fully localised on the edge and fault sites, as shown by the amplitudes of $\psi = 1$ at the far left and right ends and at the location of the stacking fault. In the case of the twin-boundary stacking fault, the low-energy states are due to the monomer (3.15b)) and the odd combination of the trimer sites either side of the fault (3.15d)).

With a finite wavevector k, the states begin to hybridise. Figures 3.13e) and f) show that the two edge states form an odd and even combination. The white bars in each figure show amplitude on A sites, and black bars show amplitude on B sites. It is then clear that at the ends of the chain (on the top and bottom monomer sites) the states are fully polarised, but because they are hybridised the total polarisation p_z over the entire system is still zero. At larger values of k the edge states can be seen to more strongly influence the centre of the system.

With a Bernal fault the system presents as if there are two sets of edge states. Figures 3.14a)-d) show the four fully localised edge states with $k = 0$ (with no hybridisation), and figures 3.14e)-h) show the slight hybridisation of the edge states. Again they are even and odd combinations of A and B sites.

With a twin-boundary fault, there are again four localised states, but instead of them all presenting like simple edge states, one of the states at the fault is due to the odd combination of the trimer of B sites either side of the fault.

As described in section 2.7, the chiral symmetry of the CDW model is described by the S_y operator. Figure 3.16 shows the dispersion relations and polarisation p_y

of the three graphene systems with a finite onsite potential, $U = 0.1\gamma_1$. This shows that the flat bands still have the polarisation of $p_y = \pm 1$, even though they are no longer zero-energy states. As k approaches k_c the flat bands separate and move towards the bulk bands, and the states are no longer fully polarised. Each case is in agreement with the polarisation shown in the CDW model (see figures 2.16 and 2.17). The low-energy states due to the stacking faults behave in the same way as the low-energy states due to the edges of the system.

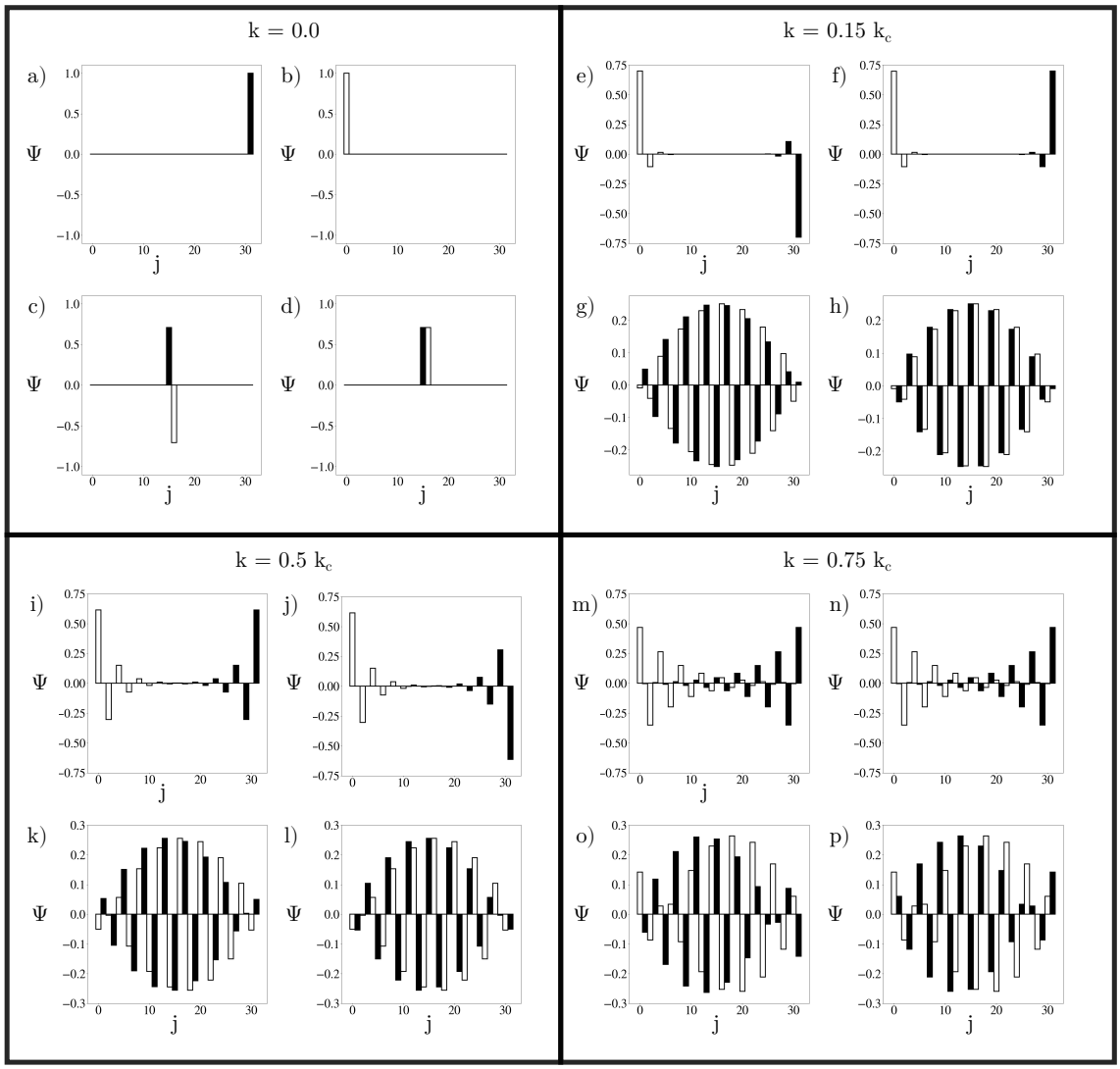

Figure 3.13: The amplitudes of the wavefunction Ψ of the four low-energy states in a faultless RG system of $N = 16$ layers with onsite potential $U = 0$. Figures a)-d) show results with $k = 0$, e)-h) with $k = 0.15\ k_c$, i)-l) with $k = 0.5\ k_c$, and m)-p) with $k = 0.75\ k_c$.

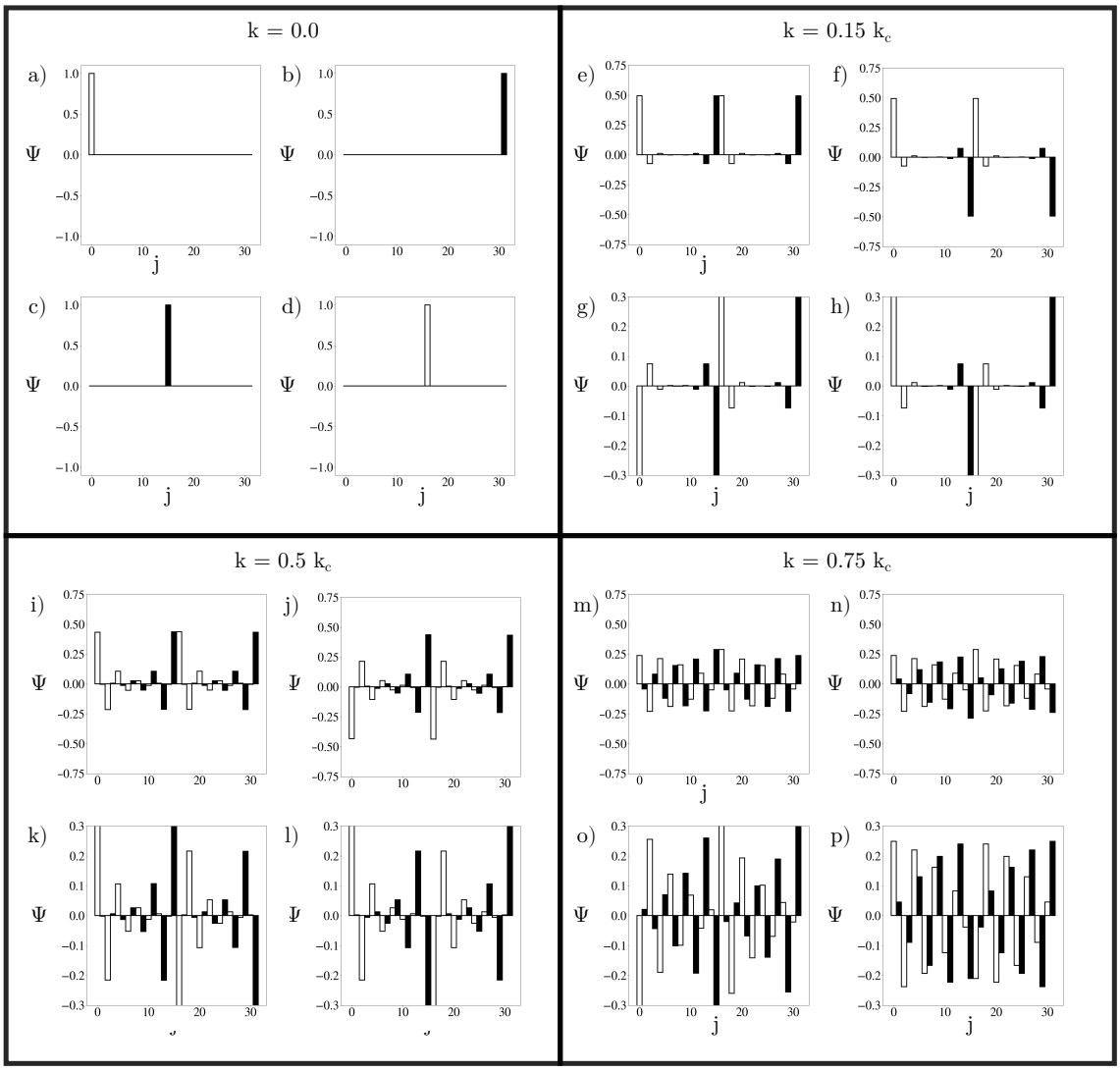

Figure 3.14: The amplitudes of the wavefunction Ψ of the four low-energy states in a faultless RG system of $N = 16$ layers with a Bernal fault in the centre and onsite potential $U = 0$. Figures a)-d) show results with $k = 0$, e)-h) with $k = 0.15\ k_c$, i)-l) with $k = 0.5\ k_c$, and m)-p) with $k = 0.75\ k_c$.

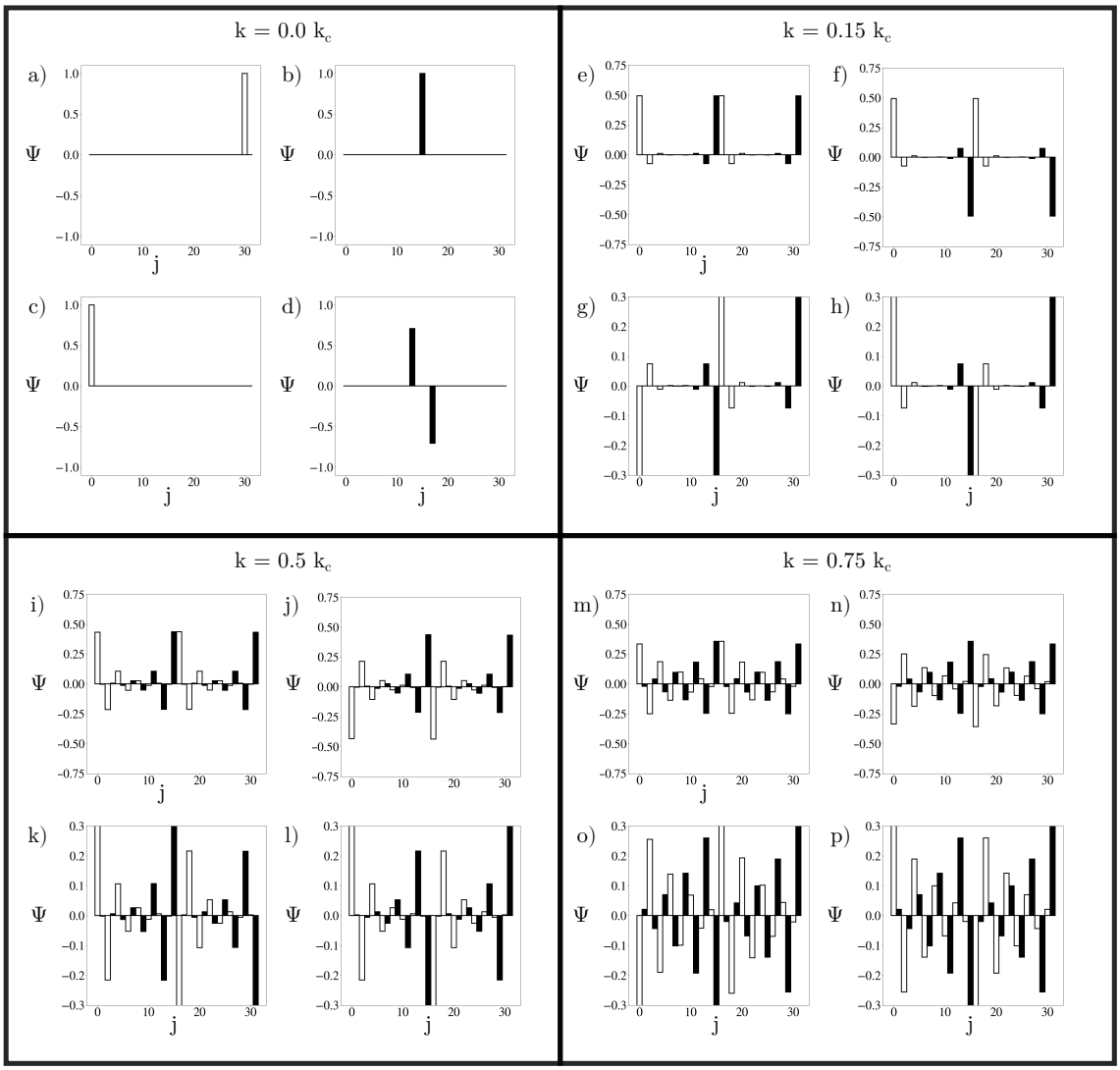

Figure 3.15: The amplitudes of the wavefunction Ψ of the four low-energy states in an RG system of $N = 16$ layers with a twin-boundary fault in the centre and onsite potential $U = 0$. Figures a)-d) show results with $k = 0$, e)-h) with $k = 0.15\ k_c$, i)-l) with $k = 0.5\ k_c$, and m)-p) with $k = 0.75\ k_c$.

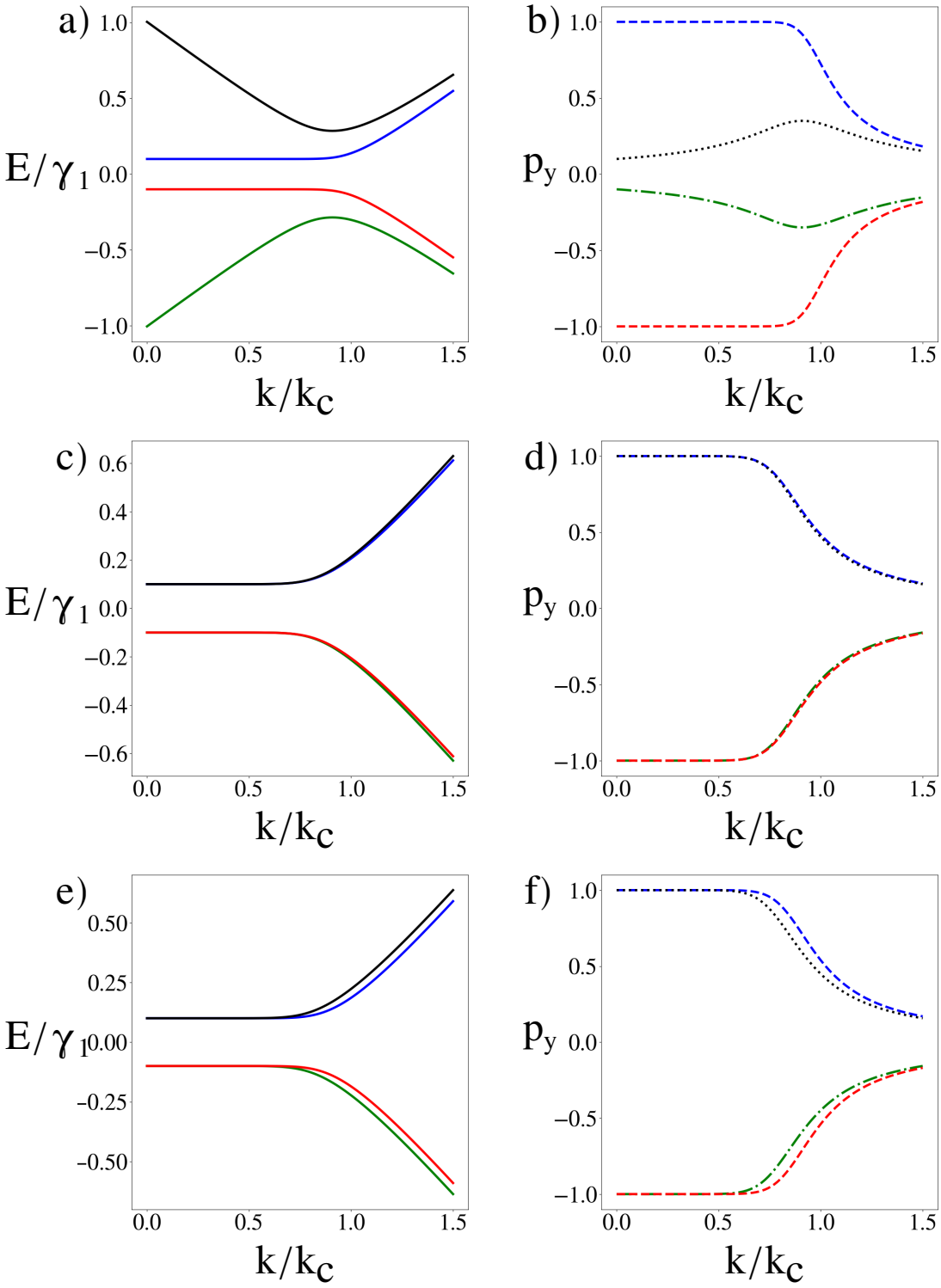

Figure 3.16: The dispersion relations and polarisation p_z of the low-energy bands of $N = 16$ layer RG with no fault (top row), a Bernal fault in the centre (middle row), or a twin-boundary fault in the centre (bottom row). Only the bands near zero energy are shown, and colours correspond across rows. Each system has a finite onsite potenital $U = 0.1$.

3.8 Conclusion

We have shown that both Bernal faults and twin-boundary faults each provide a pair of low-energy energy eigenstates. These states act in the same way as the energy eigenstates caused by the isolated edge states on the top and bottom layers of faultless RG.

We have shown that the low-energy states due to edges of a finite RG system and due to both types of stacking fault are affected by disorder applied to the onsite potentials, but resistant to interlayer disorder via a self-averaging effect. This is the case with and without the addition of an alternating onsite potential $\pm U$, as our results show that the strong peaks in density of states plots appear at $E = \pm U$, even in the presence of interlayer disorder.

Our investigation into the polarisation of the low-energy states has shown that the zero energy states are topologically protected, with a polarisation of $p_y = \pm 1$ for $k < k_c$, corresponding to the range for which $E = \pm U$.

Chapter 4

Solitons Due to Onsite Potentials

4.1 Single Sharp Soliton

As shown in Chapter 3, stacking faults in rhombohedrally-stacked thin films support localised states, manifested as flat bands in quasi-2D. Such bands tend to appear in pairs at about the same energy because the sequence of intra- and interlayer bonding either side of the fault is fixed, i.e., the texture of bonding strengths away from the fault cannot be changed by the fault. Hence, such faults are effectively coupled soliton-antisoliton pairs.

In this Chapter, we investigate the possible existence of a single, isolated band localised on a stacking fault in rhombohedrally-stacked thin films by adding different onsite energies U_i^A and U_i^B to the two atomic sites per layer i. Graphene systems will usually have zero onsite potential U, but the following investigation can be applied to a honeycomb lattice with two different atomic species, for example hexagonal boron nitride [2, 26] and others described in the introduction.

Dimensional reduction describes the mapping of a problem from a higher to a lower dimension, and in this work we do this by considering the in-plane wave vector k_x as a fixed parameter [71, 81, 82]. By using dimensional reduction we relate the Hamiltonian to that of the Rice-Mele model. This is generally not topological, but, at certain wave vectors ($|\boldsymbol{k}| = k_c$), the intra- and interlayer hoppings are effectively equal, and rhombohedral stacking is related to the charge density wave (CDW) model. Thus, stacking faults in the order of onsite energies for rhombohedral stacking are analogous to solitons in the CDW model, albeit only at a cetain wave vector.

The aim is to explore this analogy. The $2N \times 2N$ Hamiltonian of pristine, faultless,

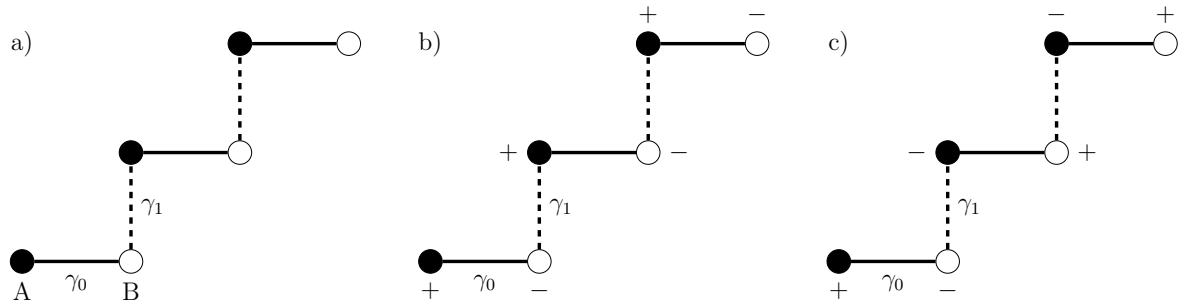

Figure 4.1: Diagram of the graphene system. The circles show the positions of the atoms in one unit cell of RG, filled black circles are sites on the A sublattice and open circles are sites on the B sublattice. The solid lines show intralayer hopping γ_0, and the dotted lines show intralayer hopping γ_1. Figure a) shows the simple RG system, b) shows the same with alternating onsite potential $\pm U$, and c) shows the same with a soliton after the first layer, so that $m = 1$, $n = 2$.

rhombohedrally-stacked N-layer graphite in the vicinity of the K point is given by (see section 2.4.3)

$$H_{ABC} = \begin{pmatrix} D_1 & V & 0 & 0 & 0 & \dots \\ V^\dagger & D_2 & V & 0 & 0 & \dots \\ 0 & V^\dagger & D_3 & V & 0 & \dots \\ 0 & 0 & V^\dagger & D_4 & V & \dots \\ \vdots & \vdots & \vdots & \vdots & \vdots & \ddots \end{pmatrix}, \tag{4.1.1}$$

where the 2×2 matrix blocks are

$$D_i = \begin{pmatrix} U_i^A & v\pi^\dagger \\ v\pi & U_i^B \end{pmatrix}, \quad V = \begin{pmatrix} 0 & 0 \\ \gamma_1 & 0 \end{pmatrix}, \quad \pi = \hbar\left(\xi k_x + i k_y\right), \tag{4.1.2}$$

and the U_i^A and U_i^B are the onsite energies of atoms on the A and B sublattices, respectively.

In this chapter we investigate whether a single, isolated band may be contained within the bulk band gap of an RG system. We introduce a soliton to the RG system by first alternating the sign of the onsite energy between atoms on the same layer, $U_i^B = -U_i^A$. A system of N layers will have the fault described by parameters (m, n), where m is the number of layers preceeding the fault, and n the number of layers that follow so that $N = m + n$. For a "sharp" soliton, the magnitudes of all

U_i are equal, and the order of the onsite energy signs reverses after m layers, and is swapped for the remaining n layers, for a total of $N = m + n$. Figure 4.1 illustrates the different variations of onsite potentials. The presence of the soliton means that two neighbouring sites in different layers will now have a negative potential, and the reversal of the onsite energy texture means that the sites on the top and bottom layers with no interlayer neighbour will have the same sign. Later in this chapter we will describe "smooth" solitons, but the location of the fault is described with the same nomenclature.

We find dispersion relations and density of states throughout this chapter using the methods in section 2.9, and the Hamiltonians used are specified in each figure. To interpret our numerical results we use dimensional reduction [71] (a mapping of a problem to one with a lower number of spatial dimensions), considering the wave vector $\boldsymbol{k}$ as a fixed parameter, with focus on values $k = 0$ and $k = k_c$. At $k = 0$ we expect this model to behave similarly to the CDW model, and at $k = k_c$ we expect it to behave similarly to the Rice-Mele model. In this way, the model RG system can be compared to a one-dimensional tight-binding model. The Rice-Mele model has two orbitals per unit cell, alternating nearest-neighbour hopping, and alternating onsite potentials. The SSH phase 2.6 and the CDW phase 2.7 of the Rice-Mele model contain chiral symmetry.

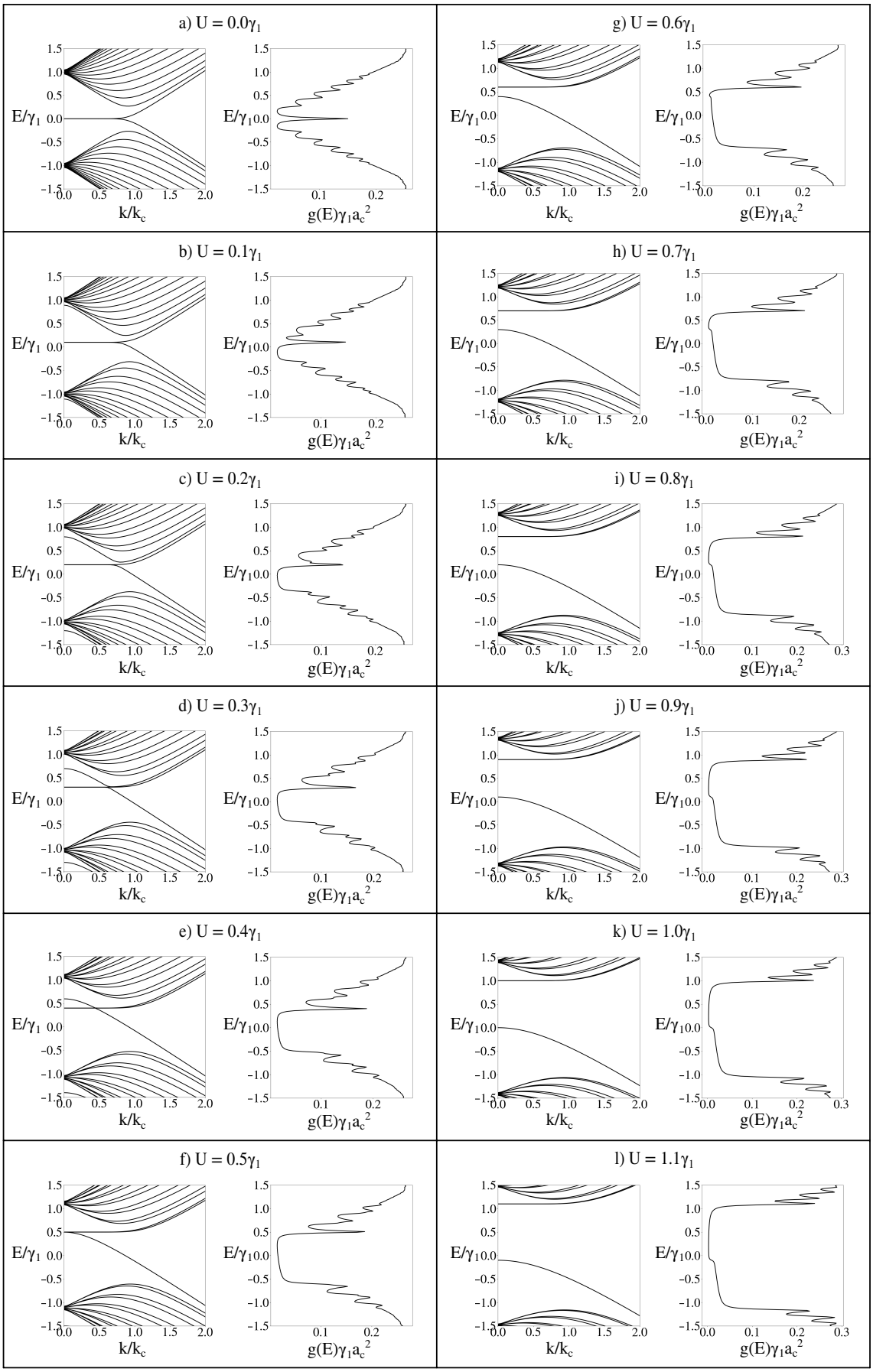

Figure 4.2: The dispersion relations and density of states of an RG system of $N = 16$ layers with a sharp soliton in the centre. The onsite potential U is varied from $U = 0.0\gamma_1$ to $U = 1.1\gamma_1$. Calculated using Hamiltonian 4.1.1.

Figure 4.2 shows the dispersion relations and density of states for an RG system of $N = 16$ layers with a single sharp soliton in the centre for varying values of the onsite energy U. 4.2 a) shows the dispersion and density of states for an RG system with onsite energy $U = 0.0$. With no finite potential there can be no soliton - this regime describes pristine faultless rhombohedral graphite. Here the two flat bands at zero energy are due to the surface states A_1 and B_N, and these flat bands lead to a sharp peak in the density of states at the same energy. The remaining figures have a finite onsite potential, with the soliton specified by $m = n = 8$. The soliton acts to displace two of the energy bands. As U is increased one band from the bulk conduction bands and one from the bulk valence bands show a slight reduction in energy. At $U = 0.5\gamma_1$, the soliton state and two edge states are triply degenerate, as shown in 4.2 f). For $U \leq 0.5\gamma_1$ the soliton band will hybridise with the surface states, and the density of states is nonzero. For $U > 0.5\gamma_1$ the soliton will be separated from all other states, and alone within the band gap.

The states are simple to understand at $k = 0$, as with no intralayer hopping present, the RG system reduces to a system of dimers, with only the edge states as monomers with energy $+U$. There are $(N-2)$ dimers with onsite energies $\pm U$, each providing states at $E = \pm\sqrt{U^2 + \gamma_1^2}$, then the two states at the soliton remain, which have energies $E = -U \pm \gamma_1$. The state which I am referring to as the "soliton" state has the higher energy of the two.

$$E_s = -U + \gamma_1 \quad \text{for } k = 0. \tag{4.1.3}$$

For $U \approx \gamma_1/2$ and $k \ll k_c$ we can derive a low-energy effective Hamiltonian using the method described in section 2.4.4. The low energy sites used are the two edge states, ψ_{A_1} and ψ_{B_N}, and the positive combination of the dimer sites that support the soliton $\psi_{\text{sol}} = \left(\psi_{B_m} + \psi_{A_{m+1}}\right)\sqrt{2}$,

$$\frac{H_{\text{sol}}^{m,n}}{\gamma_1} = \begin{pmatrix} \frac{1}{2} + \Delta + \frac{2}{9}\left(\frac{4}{5}\right)^{2(m-1)}\left(\kappa\kappa^\dagger\right)^m & \frac{1}{\sqrt{2}}\left(-\frac{4}{5}\right)^{m-1}\left(\kappa^\dagger\right)^m & -\frac{2}{9}\left(-\frac{4}{5}\right)^{m+n-2}\left(\kappa^\dagger\right)^{m+n} \\ \frac{1}{\sqrt{2}}\left(-\frac{4}{5}\right)^{m-1}\kappa^m & \frac{1}{2} - \Delta - \frac{4}{5}c_{m,n}\kappa\kappa^\dagger & \frac{1}{\sqrt{2}}\left(-\frac{4}{5}\right)^{n-1}\left(\kappa^\dagger\right)^n \\ -\frac{2}{9}\left(-\frac{4}{5}\right)^{m+n-2}\kappa^{m+n} & \frac{1}{\sqrt{2}}\left(-\frac{4}{5}\right)^{n-1}\kappa^n & \frac{1}{2} + \Delta + \frac{2}{9}\left(\frac{4}{5}\right)^{2(n-1)}\left(\kappa\kappa^\dagger\right)^n \end{pmatrix}, \tag{4.1.4}$$

where Δ is a very small dimensionless onsite energy $U/\gamma_1 = 1/2 + \Delta$, $\Delta \ll 1$, κ is

a dimensionless wave vector $\kappa = (\xi k_x + i k_y)/k_c$, $\kappa \ll 1$, and $c_{m,n}$ depends on the position of the soliton within the system,

$$c_{m,n} = \begin{cases} 1 & \text{if } m = n, \\ \frac{1}{2} & \text{if } m \neq n. \end{cases} \tag{4.1.5}$$

Only the leading order in $|\kappa|$ is kept in each element of (4.1.4).

To analyse the hybridisation of the soliton band with the surface states, the Hamiltonian (4.1.4) is simplified. We consider a soliton in the centre of the RG system, $m = n$, $N = 2m$, and also consider a large number of layers $N \gg 1$ so that terms of order $(k/k_c)^N$ may be neglected,

$$H_{\text{sol}}^{m,n} \approx \gamma_1 \begin{pmatrix} \frac{1}{2} + \Delta & \beta^\dagger & 0 \\ \beta & \frac{1}{2} - \Delta - \alpha & \beta^\dagger \\ 0 & \beta & \frac{1}{2} + \Delta \end{pmatrix}, \tag{4.1.6}$$

where $\alpha = (4/5)|\kappa|^2$ and $\beta = \left(1/\sqrt{2}\right)(-4/5)^{m-1}\kappa^m$. The three eigenvalues of (4.1.6) are

$$\frac{E}{\gamma_1} = \frac{1}{2} + \Delta, \tag{4.1.7}$$

$$\frac{E}{\gamma_1} = \frac{1}{2} - \frac{\alpha}{2} \pm \sqrt{\left(\Delta + \frac{\alpha}{2}\right)^2 + 2|\beta|^2}. \tag{4.1.8}$$

By reversing the substitution $U/\gamma_1 = 1/2 + \Delta$, the eigenvalues can be found in terms of physical parameters,

$$E = U, \tag{4.1.9}$$

$$\frac{E}{\gamma_1} = \frac{1}{2} - \frac{2}{5}\left(\frac{k}{k_c}\right)^2 \pm \sqrt{\left[\frac{U}{\gamma_1} - \frac{1}{2} + \frac{2}{5}\left(\frac{k}{k_c}\right)^2\right]^2 + \left(\frac{4}{5}\right)^{N-2}\left(\frac{k}{k_c}\right)^N}. \tag{4.1.10}$$

The corresponding unnormalised eigenstates are

$$\psi_0 = \begin{pmatrix} 1 \\ 0 \\ -1 \end{pmatrix}, \quad \psi_\pm = \begin{pmatrix} 1 \\ \frac{1}{2\beta}\left[\alpha + 2\Delta \pm \sqrt{\alpha + 4\alpha\Delta + 4\Delta^2 + 8|\beta|^2}\right] \\ 1 \end{pmatrix}, \tag{4.1.11}$$

which show that the eigenstate corresponding to the flat band, ψ_0, has no weight on the soliton - it is only a linear combination of the two surface states. An avoided crossing can be predicted using the two other eigenvalues (4.1.8). With the higher-order term in β^2 removed, the eigenvalues become

$$\frac{E_\pm}{\gamma_1} = \frac{1}{2} - \frac{\alpha}{2} \pm |\Delta + \frac{\alpha}{2}|. \tag{4.1.12}$$

For $\Delta > 0$, these become

$$\frac{E_+}{\gamma_1} = \frac{1}{2} + \Delta, \tag{4.1.13}$$

$$\frac{E_-}{\gamma_1} = \frac{1}{2} - \Delta - \alpha, \tag{4.1.14}$$

which do not interact for any values of κ. For $\Delta < 0$, there are two regimes to consider, first with $q \ll \Delta$. Substitute $\Delta = -\delta$,

$$\frac{E_+}{\gamma_1} = \frac{1}{2} + \delta - \alpha, \quad \frac{E_-}{\gamma_1} = \frac{1}{2} - \delta. \tag{4.1.15}$$

When $\alpha > 2\Delta$

$$\frac{E_+}{\gamma_1} = \frac{1}{2} - \delta, \quad \frac{E_-}{\gamma_1} = \frac{1}{2} + \delta - \alpha, \tag{4.1.16}$$

the order of the bands is reversed, and the lower energy band follows the trajectory that the higher energy band previously had. The avoided crossing occurs at the momentum

$$\alpha = 2|\Delta|, \quad \Delta < 0. \tag{4.1.17}$$

In physical parameters the avoided crossing is located at momentum

$$\left(\frac{k}{k_c}\right)^2 = \frac{5}{2}\Delta, \quad \Delta < 0. \tag{4.1.18}$$

Figure 4.3 shows a comparison of the numerics and analytics for the system described above ($N = 16$, $m = n = 8$) near the triply-degenerate point $U = \gamma_1/2$. Only the numerical eigenvalues describing the soliton state and both edge states are shown, and the analytical eigenvalues (4.1.10). This shows very good agreement for $k < k_c$.

Figure 4.4 shows the dispersion relations for an RG system of $N = 16$ layers

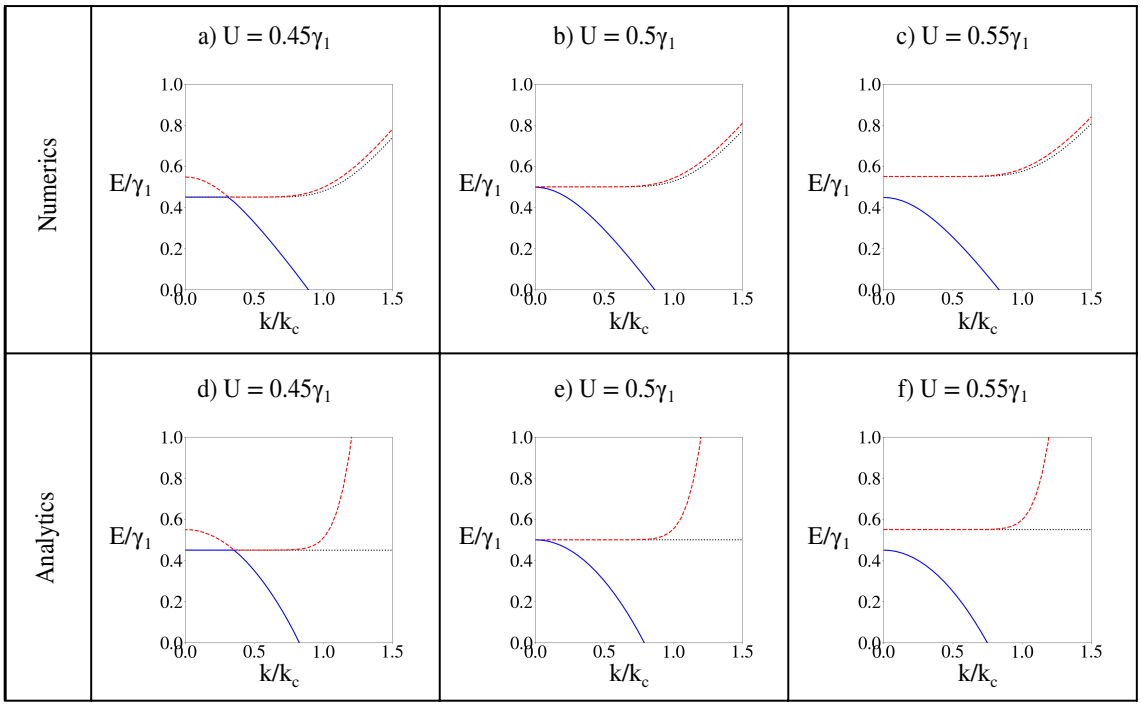

Figure 4.3: The dispersion relations of the edge states and soliton state near $U = 0.5\gamma_1$. The RG system has $N = 16$ layers, with the soliton in the centre ($m = n = 8$). The top row show the numerical calulation using Hamiltonian 4.1.4 and the bottom row shows the analytical result of equation (4.1.10).

with a sharp soliton following different numbers of layers m. The onsite potential is fixed at $U = 0.6\gamma_1$. The dispersion relations are shown from $m = 1$, where the soliton follows the very first layer, to $m = 8$, where the soliton is in the centre. After $m = 8$ the symmetry of the system is shown, ie. the dispersion relation for $m = 9$ is identical to that of $m = 7$ and so on. Figure 4.4 shows that the position of the sharp soliton has a very minimal effect on the dispersion of the soliton state - for all cases it starts at energy $E_{\text{sol}} = -U + \gamma_1$ at $k = 0$, then crosses the band gap as k increases. The soliton position is shown to have an effect on the edge state that it is closer to, as this state is pushed higher into the conductance bands for small values of k, but still unaffected at $k = 0$. This effect is most prominent in figure 4.4 a).

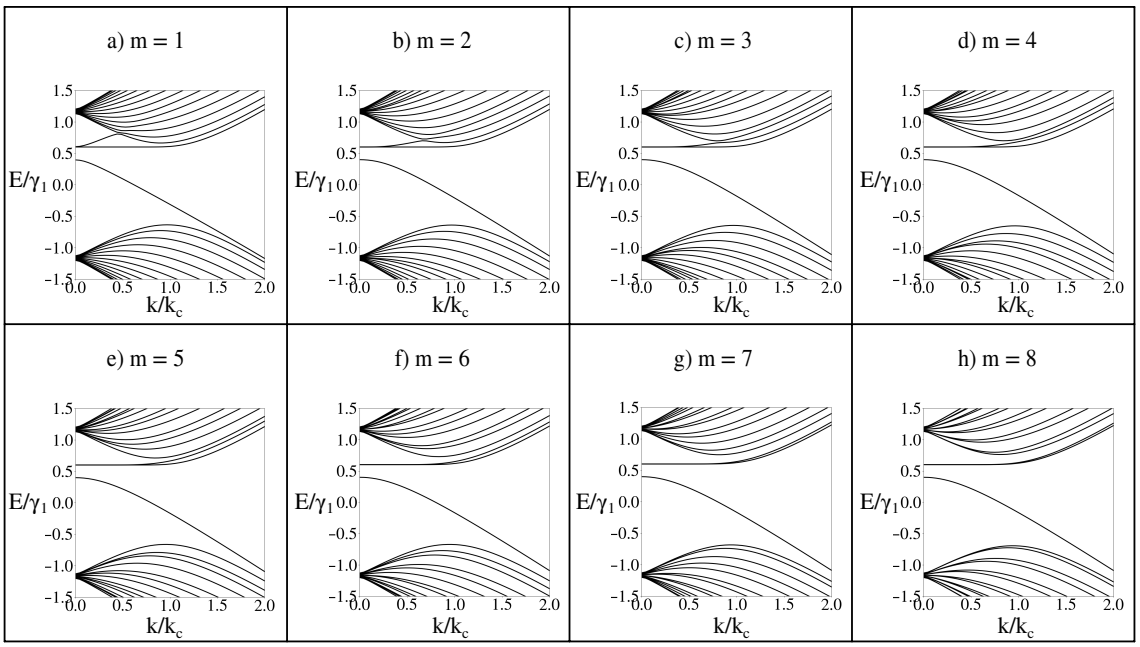

Figure 4.4: Dispersion relations for an RG system of $N = 16$ layers with a sharp soliton after different numbers of layers m. The onsite potential is $U = 0.6\gamma_1$.

4.2 Soliton-Antisoliton Pair

A soliton-antisoliton pair is introduced to the RG system by swapping the order of onsite potentials after l layers (creating the soliton) and then swapping the order again after an additional m layers (creating the antisoliton). There will be a further n layers for a total of $N = l + m + n$. The band structure and density of states for this system with $l = m = n = 8$ and varying onsite magnitudes are shown in figure 4.5. For $U = 0.0$, the soliton-antisoliton pair has no effect on the system, and the band structure is unchanged, see figure 4.5 a). For a small finite onsite potential, the flat bands gain a slight separation, and the band associated with the soliton state falls from the bulk conductance bands, while the antisoliton band rises from the bulk valence bands. At $k = 0$, the soliton has energy $E_{\text{sol}} = -U + \gamma_1$, and the antisoliton has energy $E_{\text{sol}} = U - \gamma_1$, and the surface states have energy $\pm U$. For onsite energies $U \leq \gamma_1/2$, the soliton and antisoliton states can be seen to hybridise with the bottom $(+U)$ and top$(-U)$ edge states, respectively, as shown in 4.5 c)-e). For $U = \gamma_1/2$, 4.5 f), and $k = 0$, the soliton state is degenerate with the bottom edge state, and the antisoliton states is degenerate with the upper edge state. For $U > \gamma_1/2$, the magnitudes of the soliton and antisoliton energies are lower than that of the surface state energies, and they hybridise with each other, showing an anticrossing near zero energy. For $U \leq \gamma_1$, the density of states is nonzero. For $U > \gamma_1$, 4.5 l), the antisoliton state has higher energy than the soliton state for all values of k, and there is an overall band gap of $E_g = 2\,(U - \gamma_1)$.

By expanding near energy $U \approx \gamma_1/2$ we can derive an effective 4×4 Hamiltonian in the basis ψ_{A_1}, $(\psi_{B_l} + \psi_{A_{l+1}})/\sqrt{2}$, $(\psi_{B_{l+m}} + \psi_{A_{l+m+1}})/\sqrt{2}$, ψ_{B_N}.

$$\frac{H_{\text{pair}}^{(l,m,n)}}{\gamma_1} = \begin{pmatrix} \alpha_l & \beta_l^\dagger & \Lambda_{l,m}^\dagger & 0 \\ \beta_l & \frac{1}{2} - \Delta - f_{l,m}\kappa\kappa^\dagger & \beta_m^\dagger/\sqrt{2} & \Lambda_{n,m}^\dagger \\ \Lambda_{l,m} & \beta_m/\sqrt{2} & -\frac{1}{2} + \Delta + f_{n,m}\kappa\kappa^\dagger & -\beta_n^\dagger \\ 0 & \Lambda_{n,m} & -\beta_n & -\alpha_n \end{pmatrix}, \tag{4.2.1}$$

where

$$\alpha_j = \frac{1}{2} + \Delta + \frac{2}{9}\left(\frac{4}{5}\right)^{2(j-1)} \left(\kappa\kappa^\dagger\right)^j, \tag{4.2.2}$$

$$\beta_k^{(\dagger)} = \frac{1}{\sqrt{2}}\left(-\frac{4}{5}\right)^{k-1} \left(\kappa^{(\dagger)}\right)^k, \tag{4.2.3}$$

$$\Lambda_{j,k}^{(\dagger)} = -\frac{1}{3\sqrt{2}}\left(-\frac{4}{5}\right)^{j+k-2} \left(\kappa^{(\dagger)}\right)^{j+k}, \tag{4.2.4}$$

and $U/\gamma_1 = 1/2 + \Delta$, $|\Delta| \ll 1$, and $\kappa = \left(\xi k_x + i k_y\right)/k_c$, $|\kappa| \ll 1$. Here the terms of order $|\kappa|^N$ are neglected in elements $\left(H_{\text{pair}}^{(l,m,n)}\right)_{14} = \left(H_{\text{pair}}^{(l,m,n)}\right)_{41}$, and $f_{n,m}$ is a numerical factor dependent on the position of the soliton or antisoliton,

$$f_{n,m} = \begin{cases} \frac{2}{9} & \text{for } n = 1 \text{ and } m = 1, \\ \frac{2}{5} & \text{for } n = 1 \text{ and } m > 1, \\ \frac{28}{45} & \text{for } n > 1 \text{ and } m = 1, \\ \frac{4}{5} & \text{for } n > 1 \text{ and } m > 1. \end{cases} \tag{4.2.5}$$

For $U \approx \gamma_1$, and $k = 0$, the soliton and antisoliton bands are at zero energy, and they hybridise for $k \neq 0$. To describe the relationship between the soliton and antisoliton states, we use a two-component basis and derive another low-energy effective Hamiltonian. The basis is $\left(\psi_{B_l} + \psi_{A_{l+1}}\right)/\sqrt{2}$, $\left(\psi_{B_{l+m}} + \psi_{A_{l+m+1}}\right)/\sqrt{2}$,

$$H_{\text{pair}}^{(l,m,n)} = \gamma_1 \begin{pmatrix} -\delta - g_{m,l}\kappa\kappa^\dagger & -\left(-\kappa^\dagger/2\right)^m \\ -\left(-\kappa/2\right)^m & \delta + g_{m,n}\kappa\kappa^\dagger \end{pmatrix}, \tag{4.2.6}$$

where $U/\gamma_1 = 1 + \delta$, $|\delta| \ll 1$, $|\kappa| \ll 1$, and $g_{m,l}$ depends on the relative positions of the soliton and antisoliton,

$$g_{m,l} = \begin{cases} \frac{5}{8} & \text{for } m = 1 \text{ and } l = 1, \\ \frac{3}{8} & \text{for } m = 1 \text{ and } l > 1, \\ \frac{3}{4} & \text{for } m > 1 \text{ and } l = 1, \\ \frac{1}{2} & \text{for } m > 1 \text{ and } l > 1. \end{cases} \tag{4.2.7}$$

The eigenvalues of the 2×2 Hamiltonian 4.2.6 are

$$\frac{E}{\gamma_1} = \frac{1}{2}\left(g_{m,n} - g_{m,l}\right)\left(\frac{k}{k_c}\right)^2 \pm \sqrt{\left[\frac{U}{\gamma_1} - 1 + \frac{1}{2}\left(g_{m,n} + g_{m,l}\right)\left(\frac{k}{k_c}\right)^2\right]^2 + \left(\frac{k}{2k_c}\right)^{2m}}, \tag{4.2.8}$$

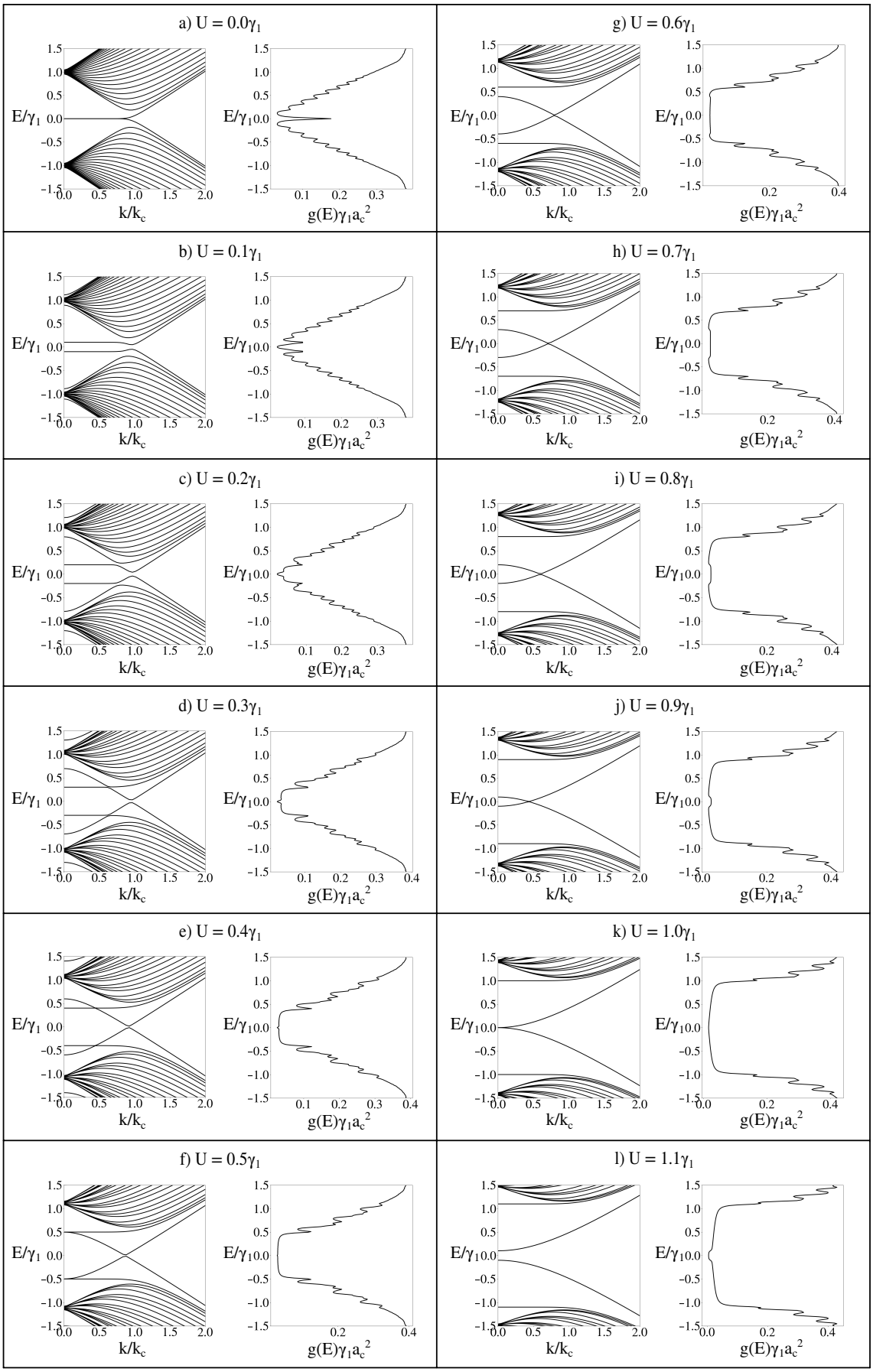

Figure 4.5: The dispersion relations and density of states of an RG system of $N = 24$ layers with a sharp soliton-antisoliton pair evenly spaced throughout the layers. The onsite potential U is varied from $U = 0.0\gamma_1$ to $U = 1.1\gamma_1$.

4.3 Smooth Solitons

A smooth soliton is formed by gradually decreasing the magnitudes of the onsite potentials until you reach the soliton layer, and then gradually increasing it back to the original magnitude. The magnitude of onsite potentials on the same layer are kept the same, and the onsite potential can be described using equation 4.3.1. The energies of an A site of the jth layer are given by

$$\epsilon_{A,j} = -U \tanh\left(\frac{j-m-1/2}{\xi}\right), \tag{4.3.1}$$

where $j = 1, \ldots, N$, and m is the number of layers preceeding the soliton, U is the magnitude of the onsite potential at infinite distance from the soliton centre, and ξ is the width of the smooth soliton (the physical width divided by the atomic spacing a). The energy of the B site on the jth layer is the negative of the corresponding A site, $\epsilon_{B,j} = -\epsilon_{A,j}$, so that each layer remains charge neutral.

Figure 4.6 shows the dispersion relations and density of states for an RG system of $N = 16$ layers with a smooth soliton of width $\xi = 8$ after 8 layers. Results are shown with onsite values at the edges of the system of $U = 0.0$ to $U = 1.1\gamma_1$. The energy of the soliton state is $E_{\text{sol}} \approx 0$ for $k = 0$, regardless of the onsite value U. The soliton state always decreases in energy and falls to the valence band as k increases, so the density of states are nonzero for all energies.

When $k = 0$, the system separates into dimers (other than the two edge states), and the soliton is localised on the two sites B_m and A_{m+1}, which are connected via interlayer hopping γ_1. The two sites will have equal onsite potentials, $\epsilon_{A,m+1} = \epsilon_{B,m} = -U \tanh(1/2\xi)$. The soliton state is the higher of the two states localised on this dimer

$$E_{\text{sol}} = \gamma_1 - U \tanh\left(\frac{1}{2\xi}\right) \quad \text{for } k = 0. \tag{4.3.2}$$

In the limit $\xi \to 0$, this returns the result shown for sharp solitons, $E_{\text{sol}} = \gamma_1 - U$, as expected. For solitons with a large width, $\xi \to \infty$, the soliton energy will converge to the value $E_{\text{sol}} \approx \gamma_1$, for all values of U.

For $k = k_c$, the soliton energy is $E_{\text{sol}} \approx 0$. This is because here the system is

analogous to the CDW model and, in this system, a soliton in the continuum limit supports a zero energy level.

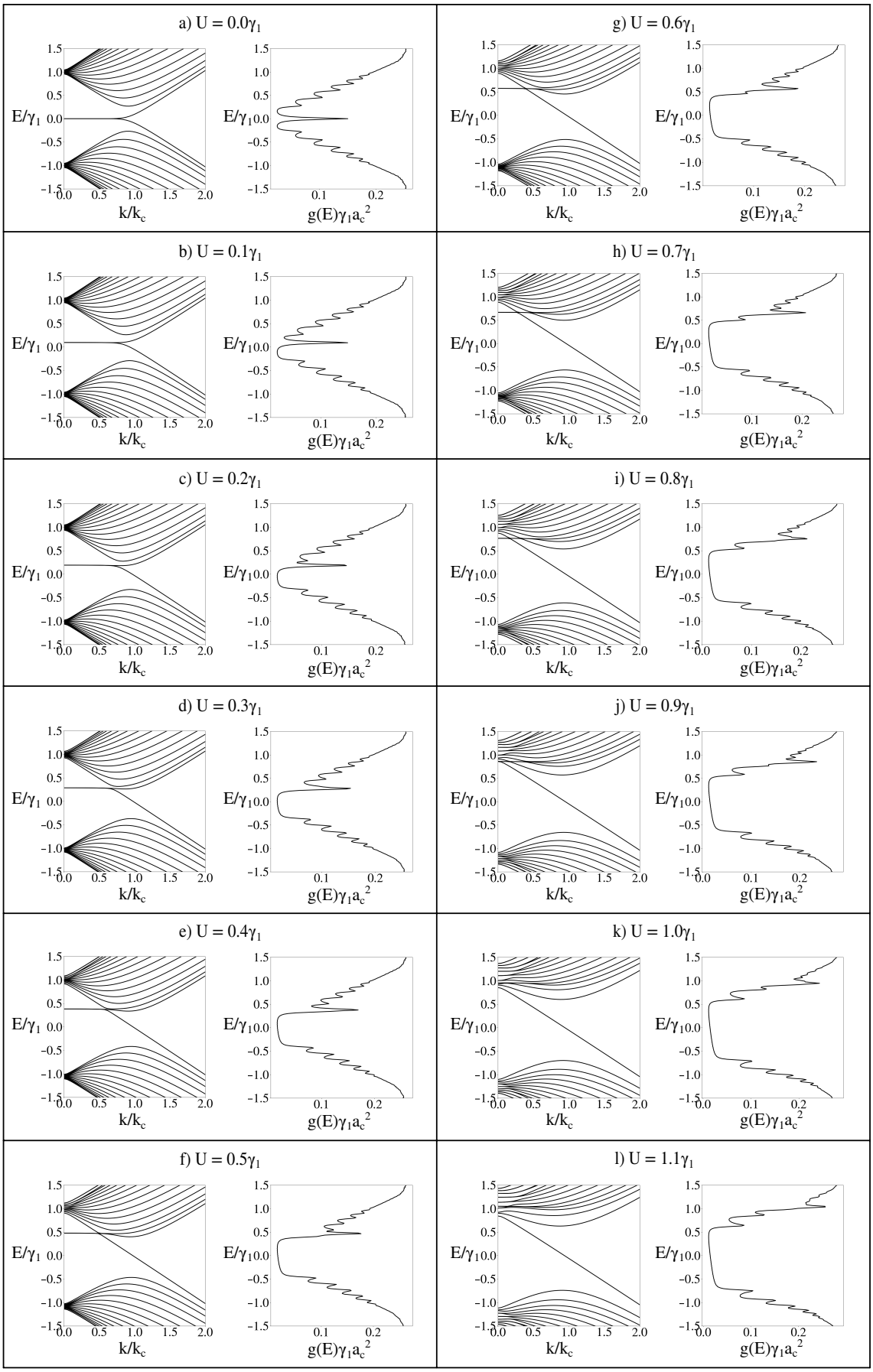

Figure 4.6: The dispersion relations and density of states of an RG system of $N = 16$ layers with a smooth soliton of width $\xi = 8$ after 8 layers. The onsite potential at infinity, U, is varied from $U = 0.0\gamma_1$ to $U = 1.1\gamma_1$.

A soliton-antisoliton pair is created by using equation (4.3.1) twice, once at the soliton position as usual, then a second time at the antisoliton position, with the signs of all onsite potentials reversed. For sites affected by both the soliton and the antisoliton, the lower of the two onsite potential values is used.

Figure 4.7 shows the dispersion relations and density of states for an RG system with a soliton-antisoliton pair. Here $N = 24$, $l = m = n = 8$, the widths of both the soliton and antisoliton are $\xi = 8$. The onsite potentials at infinity for both the soliton and antisoliton are kept equal to each other, and varied from $U = 0.0$ to $U = 1.1\gamma_1$. As in the systems discussed before, the soliton state is initially in the conductance band at $k = 0$, and as in the case of the sharp soliton-antisoliton pair, 4.5, the antisoliton state is initially in the valence band at $k = 0$. The soliton state falls and the antisoliton state rises as k is increased, with both states crossing the band gap. For $U < \gamma_1$, the soliton and antisoliton states show an avoided crossing with their closest edge state (the soliton being closer to the bottom and the antisoliton closer to the top). For all values of U the soliton and antisoliton states show an avoided crossing at $k = k_c$, where they interact at zero energy.

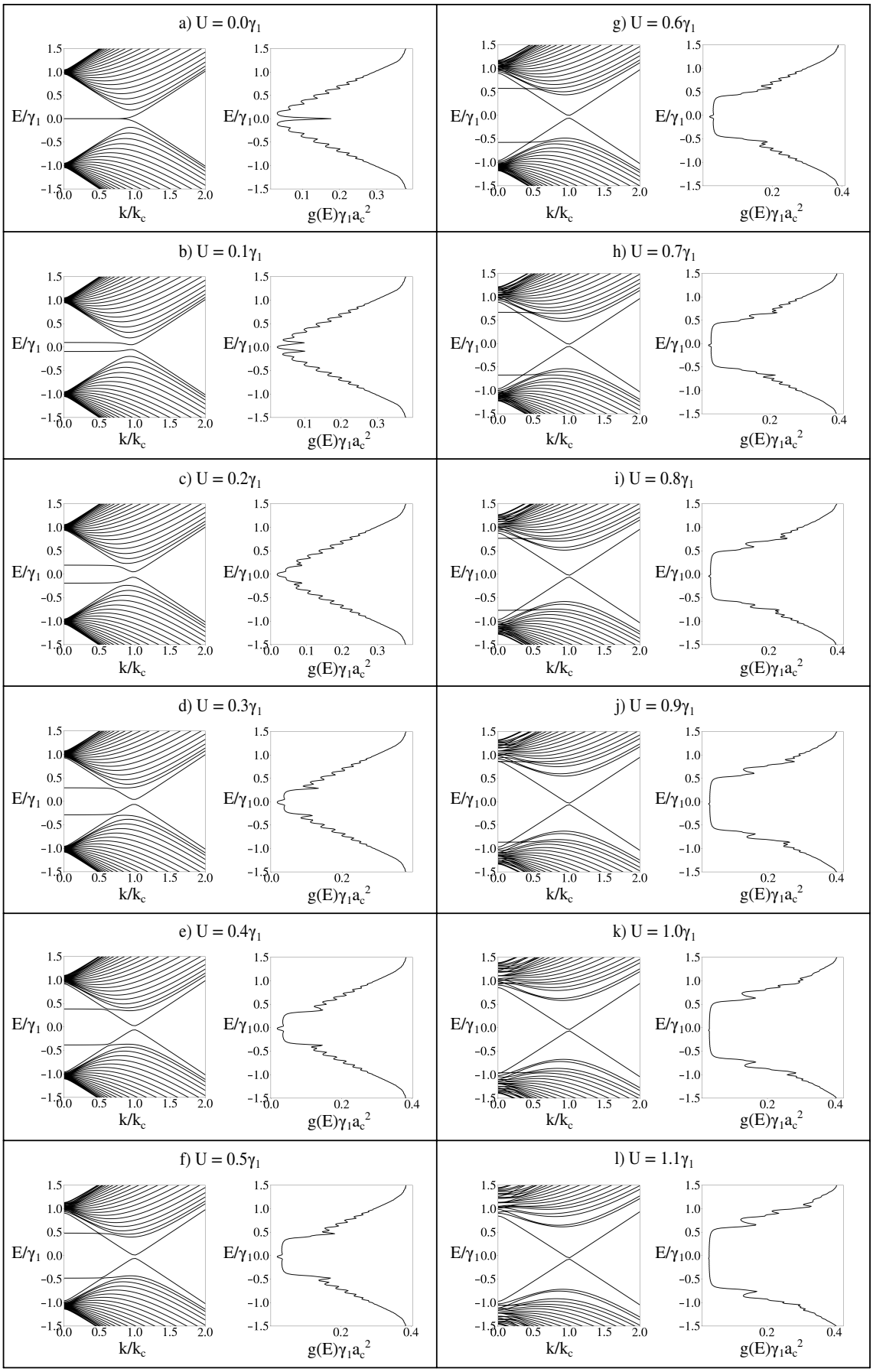

Figure 4.7: The dispersion relations and density of states of an RG system of $N = 24$ layers with a smooth soliton-antisoliton pair specified by $l = m = n = 8$, both of width $\xi = 8$. The onsite potential at infinity, U, for both features is varied from $U = 0.0\gamma_1$ to $U = 1.1\gamma_1$.

Figure 4.8 shows the dispersion relations for an RG system with a single smooth soliton with the soliton centre following different numbers of layers m.

Figure 4.9 shows the dispersion relations for an RG system of $N = 16$ layers with a smooth soliton after $m = 8$ layers with varying widths ξ. For smooth solitons with small widths, 4.9 a) the system acts similarly to the sharp soliton of the same onsite potential U, in agreement with equation (4.3.2). As the width of the soliton is increased, the energy of the soliton state at $k = 0$ rises above the energies of the edge states and into the conduction band, reaching the value $E_{\text{sol}} \approx \gamma_1$. The width of the soliton has a negligible effect on the other states.

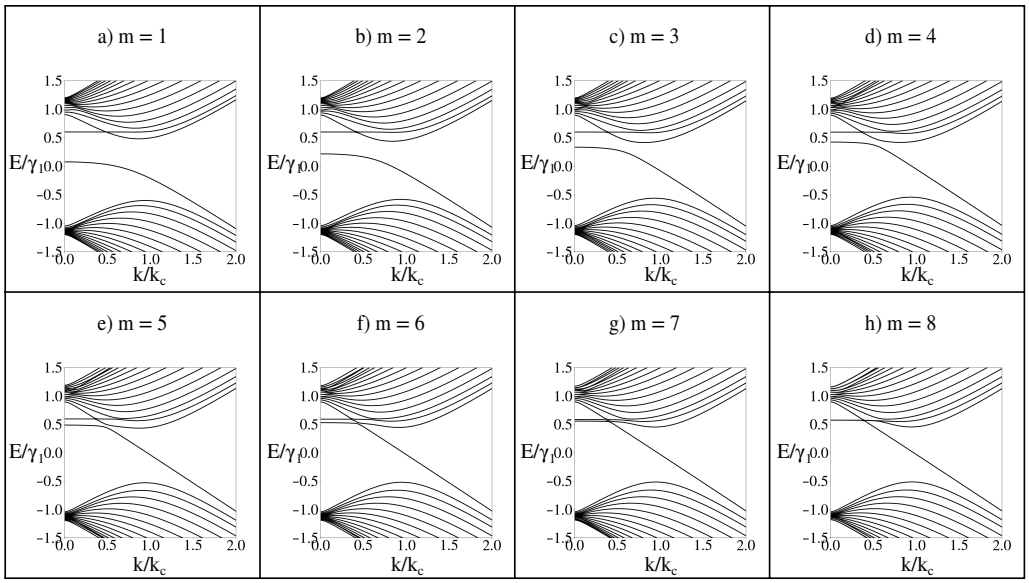

Figure 4.8: Dispersion relations for an RG system of $N = 16$ layers with a smooth soliton of width $\xi = 8$ after different numbers of layers m. The onsite potential at infinity is $U = 0.6\gamma_1$.

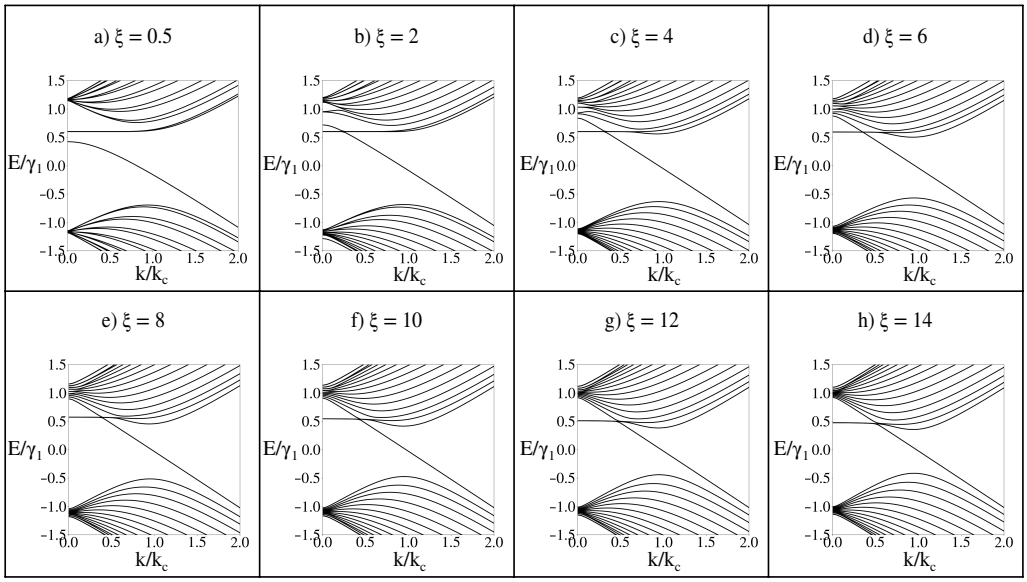

Figure 4.9: Dispersion relations for an RG system of $N = 16$ layers with smooth solitons after $m = 8$ layers with varying widths, ξ. The onsite potential is $U = 0.6\gamma_1$.

4.4 Polarisation

As described in chapter 2.7, the chiral symmetry of the CDW model in real space is represented by $U_S = T_{a/2}S_z$ in position space, and σ_y in reciprocal space. This means that, in position space, the chiral symmetry is broken by the ends of the chain (at the top and bottom layers), and also broken by a texture in the onsite potentials (which any soliton will create). In the case of a sharp soliton, the change in texture is sudden, and occurs over the length scale of the interlayer spacing. In the case of a smooth soliton, with a large enough width, ξ, the texture changes over a long distance. The reciprocal space representation of the chiral symmetry is found assuming an infinite system - it is in the continuum limit. For a large enough finite system, the polarisation can be seen to be approaching the continuum limit, and the texture of the smooth soliton interrupts the continuity far less than that of the sharp soliton.

Figure 4.10 shows the polarisation $p_y = \langle\psi_{\text{sol}}|T_{a/2}S_z|\psi_{\text{sol}}\rangle$ as a function of k_x. Plots are shown for systems with sharp solitons with onsite potentials $U = 0.6\gamma_1$ (solid line) and $U = 1.8\gamma_1$ (dashed line), and also systems with smooth solitons with onsite potentials $U = 0.6\gamma_1$ (dashed-and-dotted line) and $U = 1.8\gamma_1$ (dotted line). In all systems the polarisation initially has the value $p_y = 0.5$ at $k_x = 0$, then increases close to unity as k_x increases. The polarisation asymptotically approaches unity because the ends of the chain have already broken the chiral symmetry of the system. The polarisation sees a far steeper increase for both smooth soliton systems, as these are closer to the continuum limit. In the case of the smooth soliton system at $U = 0.6\gamma_1$, the band structure, 4.6 g), shows an avoided crossing . At the avoided crossing the bands become degenerate, and it is not possible to assign a particular wavefunction a particular energy, neither a polarisation value. Near the avoided crossing the polarisation has been interpolated, this area is shown in red.

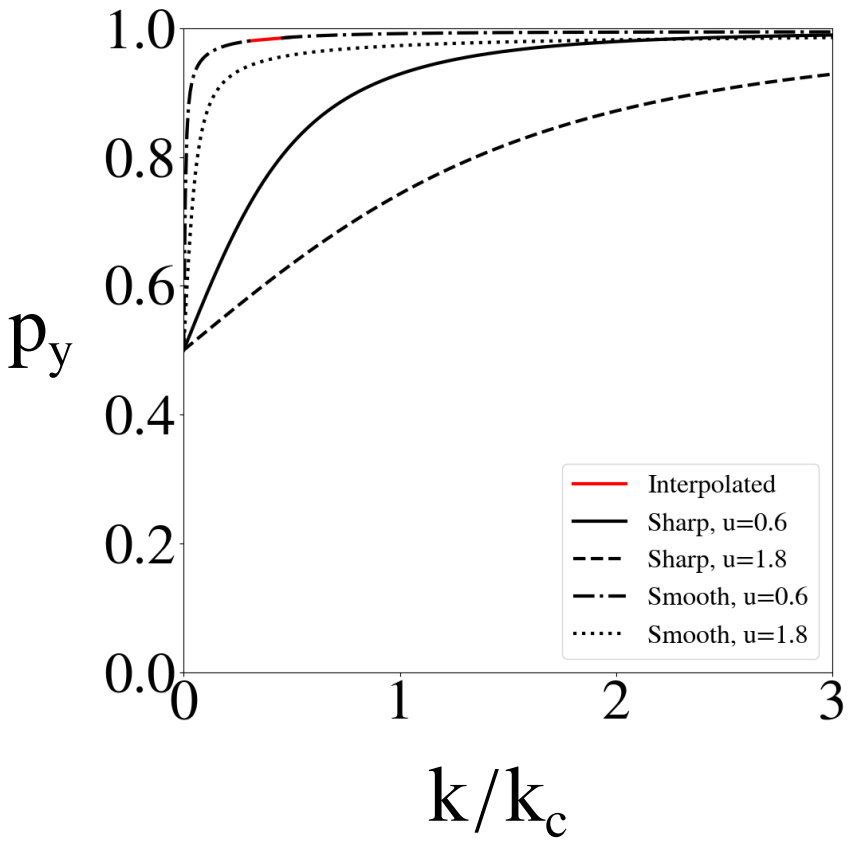

Figure 4.10: Polarisation of $N = 16$ layers with a soliton after $m = 8$ layers. The solid line shows polarisation of a sharp soliton with onsite potential $U = 0.6\gamma_1$, the dashed line shows the same system with potential $U = 1.8\gamma_1$, the dashed-and-dotted line shows a smooth soliton of width $\xi = 8$ with potential $U = 0.6\gamma_1$, and the dotted line shows the same system again with potential $U = 1.8\gamma_1$. There red section of the dashed-and-dotted line covers the vicinity of an avoided crossing, where polarisation for the soliton state is not clearly defined.

Figure 4.11 shows the polarisation p_y of the soliton state at $k = k_c$, $U = 0.6\gamma_1$ for an RG system of $N = 16$ layers, with sharp solitons (plotted with circles) and smooth solitons of width $\xi = 8$ (plotted with crosses) at different positions throughout the system. In both cases the polarisation is shown to be much smaller when the soliton is centered at either end of the system, and is close to unity when in the middle of the RG system. Because the sharp soliton has no width, it has negligible interactions with the edges of the system until very close to the edges, so the polarisation curve is flat for $m = 4$ to $m = 12$, and falls sharply beyond those positions. The smooth soliton has a width of $\xi = 8$, so when its centre is moved closer to the edges of the system its width will cause an interaction sooner than in the sharp soliton case. This is why the polarisation of the system with a smooth soliton rapidly decreases for $m < 6$ or $m > 10$. When the soliton centre is located at the end of the chain ($m = 1$ or 15) it acts similarly to a defect, but the smooth soliton still has influence over a larger area, so this disruption lowers the polarisation more than in the case of a system with a sharp soliton. When the soliton is in the middle of the system, the smooth soliton has greater polarisation because it is closer to the continuum limit than the system with a sharp soliton.

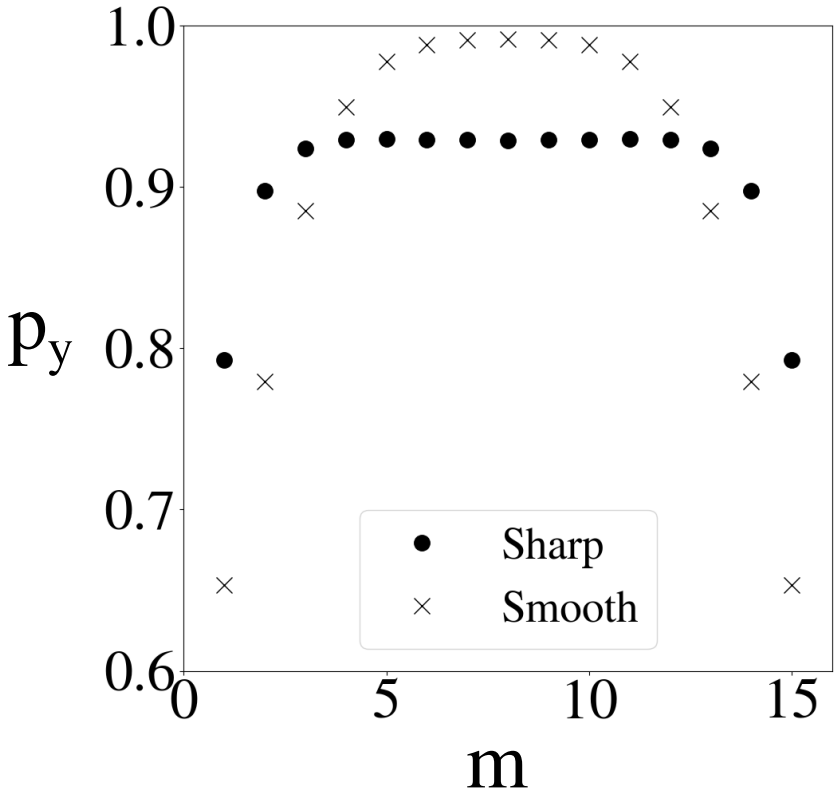

Figure 4.11: Polarisation p_y of the soliton state at $k = k_c$, $U = 0.6\gamma_1$ for RG systems of $N = 16$ layers as a function of the soliton position, where m gives the number of layers preceeding the soliton centre. The circles show results for sharp solitons, and the crosses show results for smooth solitons of width $\xi = 8$.

4.5 Disorder

We investigate the robustness of the soliton state in the presence of two types of disorder - random layer energies, and random interlayer coupling energies. Disorder is applied at a given disorder strength δ by generating random numbers δ_n within a uniform distribution $[-\delta, \delta]$. In the case of random layer energies, these values are applied to the diagonal matrix elements $H_{A_n,A_n} = H_{B_n,B_n} = \delta_n$ for layer index $n = 1, 2, 3, \ldots, N$. Random interlayer coupling energies are applied to the matrix elements between layer matrix blocks, i.e. $H_{B_1,A_2} = H_{A_2,B_1} = \gamma_1 + \delta_1$, $H_{B_2,A_3} = H_{A_3,B_2} = \gamma_1 + \delta_2$, etc., $n = 1, 2, 3 \ldots, N-1$.

Figure 4.12 shows the energy of the soliton state E_s at $k = k_c$ for an RG system of $N = 16$ layers with a sharp soliton in the centre of the system as a function of disorder strength δ, with 4.12a) showing random layer energies and 4.12b) showing random interlayer coupling energies. In both graphs the lower x axis shows the disorder strength in units of meV, and the upper x axis displays these values in units of γ_1. The onsite potential is fixed at $u = 0.6\gamma_1$. Each data point is an average over twenty different realisations of disorder, hence the increasing size of error bars with disorder strength as the standard deviation increases while the number of realisations remains constant. The mean value of the soliton energy E_s slightly decreases with disorder strength δ for both onsite and interlayer disorder, but the results for interlayer disorder decrease a little more than for onsite disorder. The standard error grows more rapidly for interlayer disorder.

Figure 4.13 shows the energy of the soliton state E_s at $k = k_c$ for an RG system of $N = 16$ layers with a smooth soliton of width $\xi = 8$ in the centre of the system as a function of disorder strength δ, with 4.13a) showing random layer energies and 4.13b) showing random interlayer coupling energies. In both graphs the lower x axis shows the disorder strength in units of meV, and the upper x axis displays these values in units of γ_1. The onsite potential is fixed at $u = 0.6\gamma_1$. As in figure 4.12 the mean value of the soliton energy E_s slightly decreases with disorder strength δ for both onsite and interlayer disorder, and again the results for interlayer disorder decrease more than for onsite disorder. Figure 4.13a) shows that both the decrease in energy and the size of the error bars are far smaller for onsite disorder with a

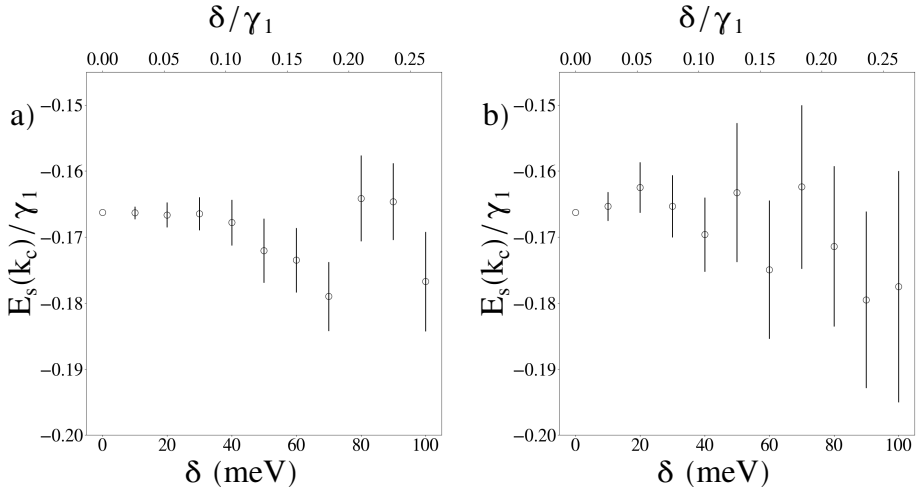

Figure 4.12: disorder averaged soliton energy at $k = k_c$ for a sharp soliton in the centre. $N = 16$, $m = n = 8$. a) shows disorder applied to the onsite potentials, b) shows disorder applied to the interlayer hopping energies. Disorder given in units of γ_1 instead of meV. Onsite energy is $U = 0.6\gamma_1$

smooth soliton than they were with a sharp soliton (in figure 4.12a)).

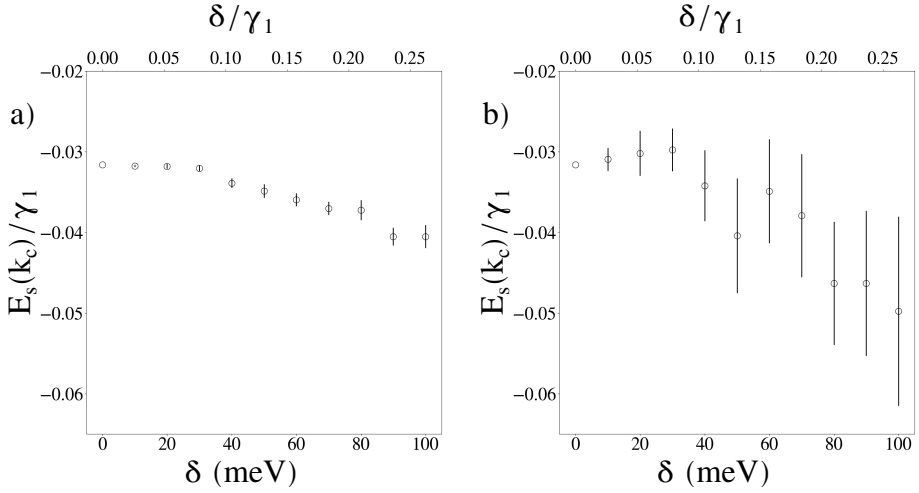

Figure 4.13: disorder averaged soliton energy at $k = k_c$ for a smooth soliton in the centre. $N = 16$, $m = n = 8$, $\xi = 8$. a) shows disorder applied to the onsite potentials, b) shows disorder applied to the interlayer hopping energies. Disorder given in units of γ_1 instead of meV. Onsite energy is $U = 0.6\gamma_1$

Figure 4.14 shows the disorder-averaged density of states for both onsite and interlayer disorder applied to systems with both smooth and sharp solitons. We consider an RG system of $N = 16$ layers, with an onsite potential of $U = 0.6\gamma_1$. The soliton is located in the middle of the system, $m = n = 8$, and in the case of smooth solitons has a width of $\xi = 8$. The first two columns show the dispersion relation and density of states of the non-disordered systems. The third and fourth columns

show the disorder-averaged density of states for disorder strengths $\delta = 0.1\gamma_1$ and $\delta = 0.2\gamma_1$, respectively. These are calculated by averaging the density of states of twenty different realisations of disorder. These figures show that interlayer onsite energy disorder (the first and third row) acts to remove sharp features of the density of states, while the presence of interlayer disorder (the second and fourth row) does not remove the peaks in the density of states. However, the peaks in these density of states plots are caused by the flat bands, which are not directly related to the soliton state itself. The flat bands are a result of the edges of the system. The soliton state is the one that crosses from the conduction band to the valence bands, leading to a non-zero density of states, and this feature is still seen in the presence of disorder.

We also considered correlated disorder, where each disorder parameter is smoothed by a gaussian curve of width η,

$$\delta_{\epsilon_{A,j}} = \frac{\sum_m w_m \exp\left(-|j-m|^2/\eta^2\right)}{\sqrt{\sum_m \exp\left(-|j-m|^2/\eta^2\right)}}. \tag{4.5.1}$$

Here η is the correlation length in units of the interlayer spacing. The summation is over all disorder parameters ($m = 1, 2, \ldots, N$ for onsite disorder, or $m = 1, 2, \ldots, N-1$ for interlayer disorder). The w_m are the list of "sharp" disorder values, generated from the uniform distribution $-W \leq w_m \leq W$ for disorder strength W. Charge neutrality is maintained within each layer so that $\delta_{\epsilon_{B,j}} = -\delta_{\epsilon_{A,j}}$ for all layers j. The square root factor is used to normalise equation (4.5.1) so that smooth disorder interpolates between sharp disorder (as discussed previously) for $\eta \ll 1$ and sample-to-sample parameter variations for $\eta \gg N$. In the case of the latter, for a given realisation of disorder, the tight-binding parameters are changed by the same amount over the whole system. By choosing Gaussian widths of $1 < \eta < N$, "smooth" disorder can be considered. In this case, equation (4.5.1) takes the original list of "sharp" disorder parameters, and modifies the values so the change in disorder from site to site is not as dramatic. Figure 4.15 shows the energy of the soliton state E_s at $k = k_c$ as a function of disorder strength δ for all four types of disorder - sharp and smooth, onsite and interlayer. Figures 4.15a) and b) show results for and RG system of $N = 16$ layers with a sharp soliton in the centre, $m = n = 8$, with onsite energy value $U = 0.6\gamma_1$. The "sharp onsite" results in 4.15a) are shown in the cor-

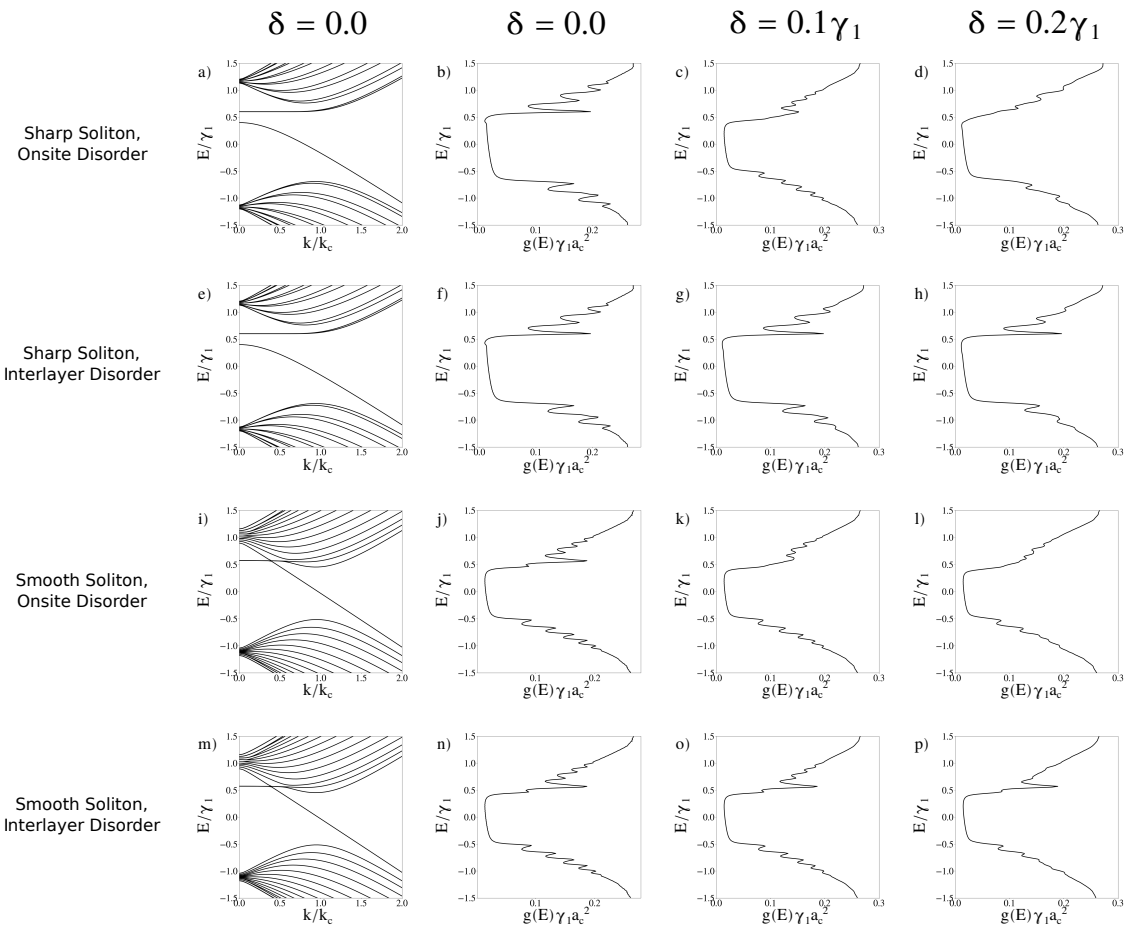

Figure 4.14: Disorder-averaged density of states for a soliton in the centre. $N = 16$, $m = n = 8$. The first two rows show results for a system with a sharp soliton, with onsite and interlayer disorder, respectively. The third and fourth rows show results for a system with a smooth solion of width $\xi = 8$, with onsite and interlayer disorder, respectively. The first column shows the dispersion relation with no disorder. The second column shows the density of states with no disorder. The third column and fourth column show the disorder-averaged density of states over twenty realisations of disorder, with disorder strengths $\delta = 0.1\gamma_1$ and $\delta = 0.2\gamma_1$, respectively.

rect position, while the other results are shifted by multiples of $0.05\gamma_1$. Each point is averaged over twenty realisations of disorder. 4.15b) shows the standard error σ_s for each set of realisations used in a). Figures 4.15c) and d) show the same results but with a system containing a smooth soliton of width $\xi = 8$. The movement of the points in 4.15a) and c) show that interlayer disorder is more disruptive that onsite disorder, for both smooth and sharp solitons and disorder. Figure 4.15b) and d) show that the standard error increases more rapidly for smooth disorder than sharp, whether onsite or interlayer disorder is applied to either smooth or sharp soliton systems.

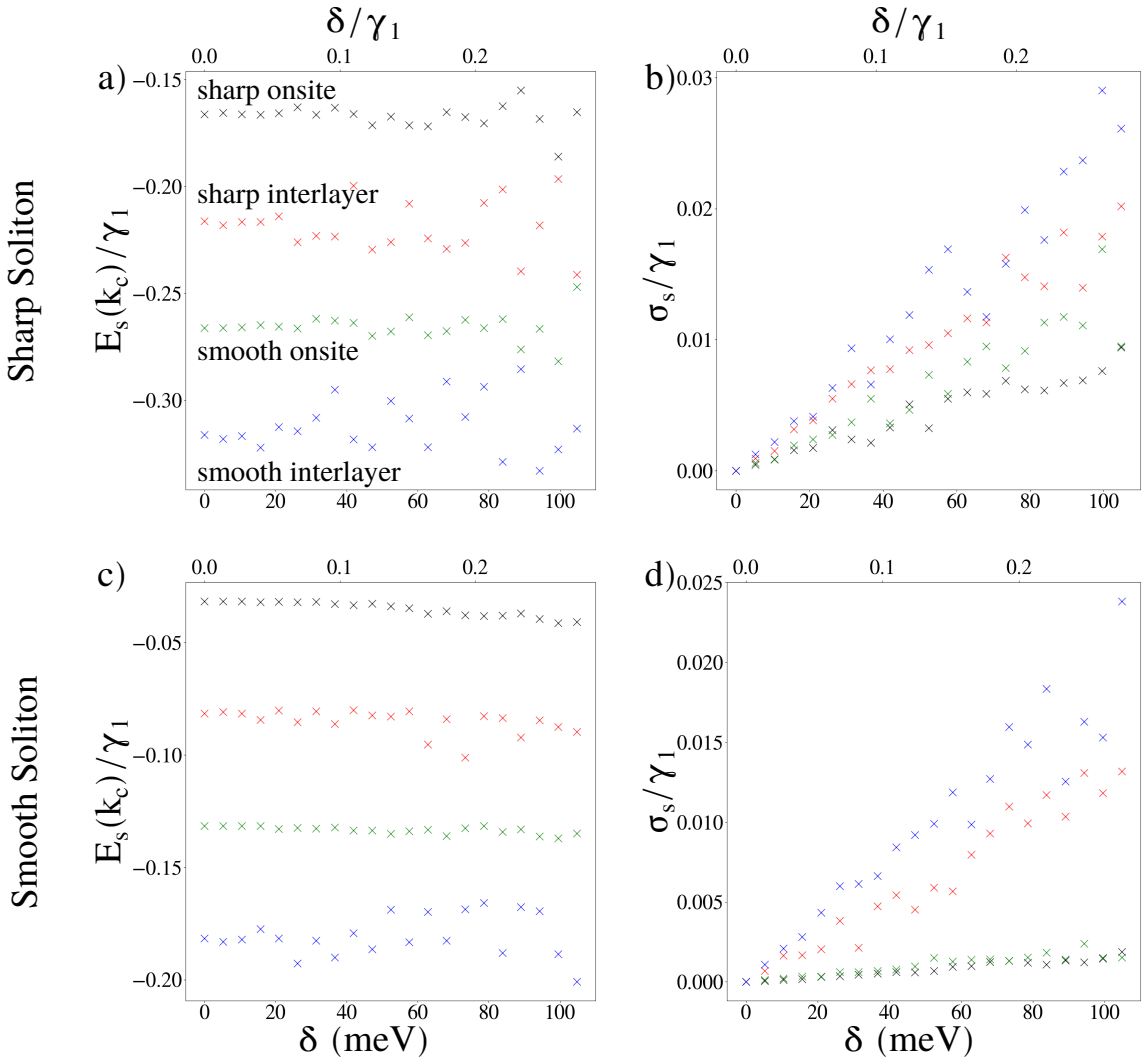

Figure 4.15: Energy of the soliton state E_s at $k = k_c$ (figures a,c) and the standard errors σ (figures b, d) as a function of disorder strength δ for an RG system of $N = 16$ layers with a soliton in the centre. The onsite potential is fixed to $U = 0.6\gamma_1$. Figures a) and b) show results with a sharp soliton, while figures c) and d) show results for a smooth soliton of width $\xi = 8$, in both cases the solitons are in the centre of the system. The top row shows results for a sharp soliton and the bottom row shows results for a smooth soliton. Each data point is calculated using twenty realisations of disorder. Black markers show onsite disorder, red for interlayer disorder, green for smooth (gaussian) onsite disorder of width $\eta = 0.1N$, and blue for smooth interlayer disorder of width $\eta = 0.1N$. In figures a) and c) the results are offset by multiples of $0.05\gamma_1$.

4.6 Conclusion

In this chapter we have used the minimal tight-binding model to investigate the electronic properties of rhombohedrally-stacked systems, where each unit cell contains a pair of atoms with opposing onsite potential sign. By reversing the texture of the onsite potentials, we were able to describe an electronic state that can be isolated within the bulk band gap - this has been identified as the "soliton state".

For onsite magnitudes $U \leq \gamma_1/2$, the soliton state hybridises with the surface states, with the three states triply degenerate at $k = 0$, $U = \gamma_1/2$. For larger values of U, the soliton state is fully isolated. We also considered "smooth" solitons, where the texture of onsite potentials was changed over a length scale larger than the interlayer distance. In systems containing these solitons, the soliton state begins in the conduction band for $k = 0$, and crosses the band gap as k increases.

The soliton state is generally dispersive, leading to a smooth nonzero density of states whereas surface states give flat bands producing peaks in the density of states. The surface states, and corresponding peaks in the density of states, are quite robust in the presence of interlayer disorder, which we attribute to the self-averaging effect discussed in Chapter 3. However, the energy of the soliton state is generally more robust to onsite energy disorder, particularly for smooth solitons, which we attribute to the chirality of the CDW model.

These results do not necessarily apply to graphene systems, but instead those systems that contain two different atoms per unit cell, and have rhombohedral stacking. An example material is hexagonal boron-nitride, which can be fabricated with rhombohedral stacking [27, 29–31, 86].

Chapter 5

Conclusion

This thesis models the electronic properties of rhombohedrally-stacked layers of thin graphite films, focusing on the influence of stacking faults. Chapters 3 and 4 describe the original research work in the thesis. Although rhombohedrally-stacked graphite (RG) is related, through dimensional reduction, to the SSH model, we show in Chapter 3 that it is not possible to realise stacking faults in RG that are analogous to single solitons in the SSH model because a stacking fault cannot change the order of intra- and interlayer hopping either side of the fault. Instead, the fault is effectively a coupled soliton-antisoliton pair. Such faults support two localised states which, along with surface states, are generally dispersionless leading to sharp peaks in the density of states (DOS) at low energy. In the minimal model, the Hamiltonians for RG in the presence of stacking faults possess sublattice chiral symmetry and the sharp peaks in the DOS are shown to be robust in the presence of interlayer disorder which preserves chiral symmetry. We incorporate alternating onsite energies which break chiral symmetry and create a band gap at low energy. Nevertheless, the states localised on stacking faults and surfaces are still dispersionless and the sharp peaks remain either side of the gap in the DOS. Surprisingly, we find that such peaks are still robust in the presence of chiral-preserving disorder and we attribute this to a self-averaging effect.

In Chapter 4 we consider whether it is possible for a stacking fault to support a single isolated, localised band. To achieve this, we model the properties of RG with alternating onsite energies and we consider a stacking fault in the texture of onsite energies. This is analogous to the Rice-Mele model and, at certain wave vectors,

to the CDW model which is a one-dimensional $\mathbb{Z}_2$ topological insulator. We find a single soliton state which is generally dispersive, leading to a smooth nonzero density of states whereas surface states give flat bands producing peaks in the density of states. Depending on parameter values, the soliton and surface states can strongly hybridise. The surface states, and corresponding peaks in the density of states, are quite robust in the presence of interlayer disorder, which we attribute to the self-averaging effect of Chapter 3. However, the energy of the soliton state is generally more robust to onsite energy disorder, particularly for smooth solitons, which we attribute to the chirality of the CDW model.

Appendix A

Periodic Boundary Conditions

To investigate a very large system without the interference of edge effects we use Born-von Karman periodic boundary conditions in both primitive lattice directions $\Phi(\boldsymbol{r} + N_l \boldsymbol{a}_l) = \Phi(\boldsymbol{r})$ where $l = 1, 2$ in 2D, N_l are integers, $N = N_1 N_2$ is the number of primitive unit cells, $N \gg 1$. Write $\boldsymbol{q} = s_1 \boldsymbol{b}_1 + s_2 \boldsymbol{b}_2$ where s_1, s_2 are to be determined. This means that $\boldsymbol{q} \cdot \boldsymbol{a}_l = 2\pi s_l$. Combine Bloch's theorem (2.1.5) with the restrictions given by the periodic boundary conditions to find the permitted values of wave vectors $\boldsymbol{q}$:

$$\begin{aligned} \Phi(\boldsymbol{r} + N_l \boldsymbol{a}_l) &= e^{i\boldsymbol{q}\cdot\boldsymbol{r}} e^{i\boldsymbol{q}\cdot N_l \boldsymbol{a}_l} u(\boldsymbol{r} + N_l \boldsymbol{a}_l), \\ &= e^{i\boldsymbol{q}\cdot N_l \boldsymbol{a}_l} e^{i\boldsymbol{q}\cdot\boldsymbol{r}} u(\boldsymbol{r}), \\ &= e^{i\boldsymbol{q}\cdot N_l \boldsymbol{a}_l} \Phi(\boldsymbol{r}). \end{aligned} \tag{A.0.1}$$

We use the boundary condition $\Phi(\boldsymbol{r} + N_l \boldsymbol{a}_l) = \Phi(\boldsymbol{r})$ to get $\Phi(\boldsymbol{r}) = e^{i\boldsymbol{q}\cdot N_l \boldsymbol{a}_l} \Phi(\boldsymbol{r})$, then make use of $\boldsymbol{q} \cdot \boldsymbol{a}_l = 2\pi s_l$

$$\begin{aligned} e^{i\boldsymbol{q}\cdot N_l \boldsymbol{a}_l} &= e^{i2\pi s_l N_l} = 1 \equiv e^{2\pi i m_l}, \\ &\Rightarrow s_l = \frac{m_l}{N_l}, \\ &\Rightarrow \boldsymbol{q} = \frac{m_1}{N_1}\boldsymbol{b}_1 + \frac{m_2}{N_2}\boldsymbol{b}_2, \end{aligned} \tag{A.0.2}$$

where $m_1, m_2 \in \mathbb{Z}$.

Appendix B

Two Different Types of Tight-Binding Model

In this appendix we will discuss the two tight-binding Hamiltonians: the basis I or 'periodic' Hamiltonian, and the basis II or 'canonical' Hamiltonian. We will also show how the models are related, and why one would be chosen instead of the other.

To form the canonical Hamiltonian, the Fourier transforms must be dependent on the atomic positions of the atoms within the unit cell. In the two band models we are considering the atomic positions are vectors $\boldsymbol{R}_A$ and $\boldsymbol{R}_B$, and the Fourier transforms are

$$\begin{aligned} |\boldsymbol{k}, A\rangle &= \frac{1}{\sqrt{N}} \sum_{\boldsymbol{R}_A} |\boldsymbol{R}_A, A\rangle \, e^{i\boldsymbol{k}\cdot\boldsymbol{R}_A}, \\ |\boldsymbol{R}_A, A\rangle &= \frac{1}{\sqrt{N}} \sum_{\boldsymbol{k}} |\boldsymbol{k}, A\rangle \, e^{-i\boldsymbol{k}\cdot\boldsymbol{R}_A}, \\ |\boldsymbol{k}, B\rangle &= \frac{1}{\sqrt{N}} \sum_{\boldsymbol{R}_B} |\boldsymbol{R}_B, B\rangle \, e^{i\boldsymbol{k}\cdot\boldsymbol{R}_B}, \\ |\boldsymbol{R}_B, B\rangle &= \frac{1}{\sqrt{N}} \sum_{\boldsymbol{k}} |\boldsymbol{k}, B\rangle \, e^{-i\boldsymbol{k}\cdot\boldsymbol{R}_B}. \end{aligned} \tag{B.0.1}$$

These are the Fourier transforms used in section 2.2. In the case of the SSH model, with $\boldsymbol{R}_{m,A} = ma$ and $\boldsymbol{R}_{m,B} = (m + 1/2)\, a$, the Bloch Hamiltonian will be

$$H_{\mathrm{c}}(k) = \begin{pmatrix} 0 & ve^{ika/2} + we^{-ika/2} \\ ve^{-ika/2} + we^{ika/2} & 0 \end{pmatrix}. \tag{B.0.2}$$

The problem with this type of Hamiltonian is that it is not periodic about the first Brillouin zone; $H_{AB}(k + 2\pi/a) \neq H_{AB}(k)$. The trajectory of the vector $\boldsymbol{d}$ will not form a complete loop as k spans the first Brillouin zone, so a winding number cannot be defined for this Hamiltonian.

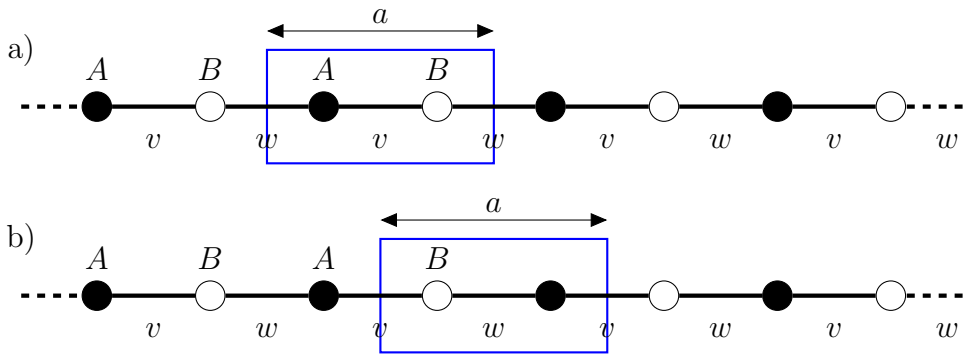

Figure B.1: Two possible choices of unit cell for a section of an infinite SSH chain. Atoms on sublattices A and B are shown with filled and empty circles, respectively. In a) the intracell hopping parameter is v and the intercell hopping paramter is w,whereas in b) the intracell hopping parameter becomes w and the intercell hopping parameter is v. The lattice vector has length a and individual atoms are spaced $a/2$ apart.

The periodic Hamiltonian, as its name suggests, solves this problem. To form this Hamiltonian the Fourier transforms must not depend on the atomic positions $\boldsymbol{R}_A$ and $\boldsymbol{R}_B$, and instead be dependent only on the lattice vector $\boldsymbol{R}$. The new Fourier transforms are

$$\begin{aligned}
\widetilde{|\boldsymbol{k}, A\rangle} &= \frac{1}{\sqrt{N}} \sum_{\boldsymbol{R}} |\boldsymbol{R} + \boldsymbol{\tau}_A, A\rangle \, e^{i\boldsymbol{k}\cdot\boldsymbol{R}}, \\
|\boldsymbol{R} + \boldsymbol{\tau}_A, A\rangle &= \frac{1}{\sqrt{N}} \sum_{\boldsymbol{k}} \widetilde{|\boldsymbol{k}, A\rangle} e^{-i\boldsymbol{k}\cdot\boldsymbol{R}}, \\
\widetilde{|\boldsymbol{k}, B\rangle} &= \frac{1}{\sqrt{N}} \sum_{\boldsymbol{R}} |\boldsymbol{R} + \boldsymbol{\tau}_B, B\rangle \, e^{i\boldsymbol{k}\cdot\boldsymbol{R}}, \\
|\boldsymbol{R} + \boldsymbol{\tau}_B, B\rangle &= \frac{1}{\sqrt{N}} \sum_{\boldsymbol{k}} \widetilde{|\boldsymbol{k}, B\rangle} e^{-i\boldsymbol{k}\cdot\boldsymbol{R}}.
\end{aligned} \tag{B.0.3}$$

Using these Fourier transforms for the SSH model, with $\boldsymbol{R} = \boldsymbol{R}_A$, $\boldsymbol{\tau}_A = 0$, and $\boldsymbol{\tau}_B = a/2$ (as shown in figure B.1a)), the Bloch Hamiltonian will be

$$H_{\mathrm{p}}^{\mathrm{a}}(k) = \begin{pmatrix} 0 & v + we^{-ika} \\ v + we^{ika} & 0 \end{pmatrix}, \tag{B.0.4}$$

which is now periodic about the first Brillouin zone. This Hamiltonian depends on the choice of unit cell, it was formed using $\boldsymbol{R} = \boldsymbol{R}_A$, but swapping to $\boldsymbol{R} = \boldsymbol{R}_B$, $\boldsymbol{\tau}_B = 0$, $\boldsymbol{\tau}_A = a/2$ (figure B.1b))would instead give a different periodic Hamiltonian:

$$H_{\mathrm{p}}^{\mathrm{b}}(k) = \begin{pmatrix} 0 & ve^{ika} + w \\ ve^{-ika} + w & 0 \end{pmatrix}. \tag{B.0.5}$$

Importantly, the choice of unit cell swaps the role of hopping parameters v and w, which are critical in the definition of the winding number. In the first case (unit cell a)) the trajectory of the vector $\boldsymbol{d}$ will be a circle of radius w, centred on $(v, 0)$, whereas in the second (unit cell b)) the trajectory is instead a circle of radius v centred on $(w, 0)$.

When using the canonical representation, we could also choose that the A and B atoms are not separated in space at all. Setting $\boldsymbol{R}_{m,A} = \boldsymbol{R}_{m,B} = ma$ and using the first set of Fourier transforms gives the Hamiltonian

$$H_{\mathrm{c}}^{a}(k) = \begin{pmatrix} 0 & v + we^{-ika} \\ v + we^{ika} & 0 \end{pmatrix}, \tag{B.0.6}$$

which is exactly the same as the periodic Hamiltonian B.0.4 formed using unit cell a). If we instead set $\boldsymbol{R}_A = \boldsymbol{R}$ and $\boldsymbol{R}_B = \boldsymbol{R}_A + a$, the canonical Hamiltonian becomes

$$H_{\mathrm{c}}^{b}(k) = \begin{pmatrix} 0 & ve^{ika} + w \\ ve^{-ika} + w & 0 \end{pmatrix}, \tag{B.0.7}$$

which is the same as the periodic Hamiltonian B.0.5 formed using unit cell b). Note that the canonical and periodic Hamiltonians are related by a unitary transform $U(k, s)$

$$U(k, s) = \begin{pmatrix} e^{iks/2} & 0 \\ 0 & e^{iks/2} \end{pmatrix}, \tag{B.0.8}$$

$$H_c^{\alpha}(k) = U^{\dagger} H_p^{\alpha}(k) U; \quad H_p^{\alpha}(k) = U H_c^{\alpha}(k) U^{\dagger}, \quad \alpha = a, b, \tag{B.0.9}$$

where s is the separation between the A and B atomcs within the same unit cell. For a discussion of more general two-band Hamiltonians see the catalogue [69].

Appendix C

Expansion Near the Dirac Point

The function $f(\boldsymbol{q})$ is

$$f(\boldsymbol{q}) = e^{iq_y a/\sqrt{3}} + 2e^{-iq_y a/2\sqrt{3}} \cos(q_x a/2). \tag{C.0.1}$$

Investigate the behaviour near the K points using the substitution $\boldsymbol{q} = \boldsymbol{K} + \boldsymbol{k}$ and the $\boldsymbol{K}$ point $\boldsymbol{K} = (\xi 4\pi/3a, 0)$

$$f(\boldsymbol{K} + \boldsymbol{k}) = e^{ik_y a/\sqrt{3}} + 2e^{-ik_y a/2\sqrt{3}} \cos(2\pi/3 + k_x a/2). \tag{C.0.2}$$

Taylor expand the exponentials and use the cosine double angle to get

$$f(\boldsymbol{K} + \boldsymbol{k}) = \left(1 + \frac{ik_y a}{\sqrt{3}}\right) + 2\left(1 - \frac{ik_y a}{2\sqrt{3}}\right)\left[\cos(2\pi/3)\cos(k_x a/2) - \sin(2\pi/3)\sin(k_x a/2)\right] \tag{C.0.3}$$

$$f(\boldsymbol{K} + \boldsymbol{k}) = \left(1 + \frac{ik_y a}{\sqrt{3}}\right) + 2\left(1 - \frac{ik_y a}{2\sqrt{3}}\right)\left[-\frac{1}{2}\cos(k_x a/2) - \frac{\sqrt{3}}{2}\sin(k_x a/2)\right] \tag{C.0.4}$$

expand for small angles

$$f(\boldsymbol{K} + \boldsymbol{k}) = \left(1 + \frac{ik_y a}{\sqrt{3}}\right) + 2\left(1 - \frac{ik_y a}{2\sqrt{3}}\right)\left[-\frac{1}{2} - \frac{\sqrt{3}}{2}\left(\frac{k_x a}{2}\right)\right] \tag{C.0.5}$$

$$f(\boldsymbol{K} + \boldsymbol{k}) = \left(1 + \frac{ik_y a}{\sqrt{3}}\right) - \left(1 - \frac{ik_y a}{2\sqrt{3}}\right) - \frac{\sqrt{3}k_x a}{2}\left(1 - \frac{ik_y a}{2\sqrt{3}}\right) \tag{C.0.6}$$

$$f\left(\boldsymbol{K}+\boldsymbol{k}\right)=\frac{3ik_{y}a}{2\sqrt{3}}-\frac{\sqrt{3}k_{x}a}{2} \tag{C.0.7}$$

where the term in $k_x k_y$ was deemed negligibly small. This leaves

$$\begin{aligned} f\left(\boldsymbol{K}+\boldsymbol{k}\right) &= \frac{\sqrt{3}ik_{y}a}{2}-\frac{\sqrt{3}k_{x}a}{2} \\ &= -\frac{\sqrt{3}a}{2}\left(k_{x}-ik_{y}\right). \end{aligned} \tag{C.0.8}$$

Appendix D

Low Energy Model Example: Bilayer Graphene

We will apply the steps described in the previous section to bilayer graphene. We start with the bilayer graphene Hamiltonian in the minimal model in the basis of the atomic sites; A_1, B_1, A_2, B_2,

$$H = \begin{pmatrix} \epsilon_{A1} & v\pi^\dagger & 0 & 0 \\ v\pi & \epsilon_{B1} & \gamma_1 & 0 \\ 0 & \gamma_1 & \epsilon_{A2} & v\pi^\dagger \\ 0 & 0 & v\pi & \epsilon_{B2} \end{pmatrix}. \tag{D.0.1}$$

We manually identify the high- and low-energy states. For a bilayer system the low-energy states are the edges (A_1 and B_2) and the high-energy states are the dimer sites in between (B_1 and A_2). This means the new basis will be A_1, B_2, B_1, A_2.

$$H = \begin{pmatrix} \epsilon_{A1} & 0 & v\pi^\dagger & 0 \\ 0 & \epsilon_{B2} & 0 & v\pi \\ v\pi & 0 & \epsilon_{B1} & \gamma_1 \\ 0 & v\pi^\dagger & \gamma_1 & \epsilon_{A2} \end{pmatrix}. \tag{D.0.2}$$

To perform the low-energy expansion, we assume that the intralayer hopping γ_1 is much larger than the other energy terms, and introduce a temporary term z that is attached to each small energy term, and will be used to monitor which terms become

vanishingly small as the method progresses. We set $xz = v\pi/\gamma_1$ and $\mu_i z = \epsilon_i/\gamma_1$, and divide the Hamiltonian by γ_1.

$$H = \begin{pmatrix} \mu_{A1}z & 0 & x^\dagger z & 0 \\ 0 & \mu_{B2}z & 0 & xz \\ xz & 0 & \mu_{B1}z & 1 \\ 0 & x^\dagger z & 1 & \mu_{A2}z \end{pmatrix}. \tag{D.0.3}$$

Then the matrix blocks outlined in (2.4.18) are

$$\begin{aligned} h_\theta = \begin{pmatrix} \mu_{A1}z & 0 \\ 0 & \mu_{B2}z \end{pmatrix}, \quad h_\chi = \begin{pmatrix} \mu_{B1}z & 1 \\ 1 & \mu_{A2}z \end{pmatrix}, \\ u = \begin{pmatrix} x^\dagger z & 0 \\ 0 & xz \end{pmatrix}, \quad u^\dagger = \begin{pmatrix} xz & 0 \\ 0 & x^\dagger z \end{pmatrix}. \end{aligned} \tag{D.0.4}$$

The effective Hamiltonian is found using equations (2.4.26) and (2.4.27). First, find $S^{-1/2}$ using the binomial expansion

$$S^{-1/2} \approx 1 - \frac{1}{2} u h_\chi^{-2} u^\dagger + \ldots, \tag{D.0.5}$$

with the number of terms used corresponding to the number of layers in the system (two terms for bilayer). We will also invert h_χ using the binomial theorem.

$$\begin{aligned} h_\chi &= \sigma_x + \frac{1}{2}(\sigma_0 + \sigma_z)\mu_{A2}z + \frac{1}{2}(\sigma_0 - \sigma_z)\mu_{B1}z \\ h_\chi^{-1} &= \sigma_x [\sigma_0 + \delta]^{-1} \\ \delta &= \frac{1}{2}\sigma_x(\sigma_0 + \sigma_z)\mu_{A2}z + \frac{1}{2}\sigma_x(\sigma_0 - \sigma_z)\mu_{B1}z \\ h_\chi^{-1} &\approx \sigma_x \left[\sigma_0 - \delta + \delta^2 - \mathcal{O}\left(z^3\right)\right] \end{aligned} \tag{D.0.6}$$

Keeping only the linear term in z gives

$$h_\chi^{-1} \approx \begin{pmatrix} -\mu_{B1}z & 1 \\ 1 & -\mu_{A2}z \end{pmatrix}. \tag{D.0.7}$$

Find the term $uh_\chi^{-2}u^\dagger$ needed for the S matrix.

$$uh_\chi^{-2}u^\dagger \approx \begin{pmatrix} |x|^2z^2 & 0 \\ 0 & |x|^2z^2 \end{pmatrix}, \tag{D.0.8}$$

where we have neglected terms with powers of z greater than 2. Similarly, $uh_\chi^{-1}u^\dagger$ is needed for H^{eff}

$$uh_\chi^{-1}u^\dagger \approx \begin{pmatrix} 0 & \left(x^\dagger\right)^2 z^2 \\ x^2z^2 & 0 \end{pmatrix}. \tag{D.0.9}$$

The term $\left(h_\theta - uh_\chi^{-1}u^\dagger\right)$ will be

$$h_\theta - uh_\chi^{-1}u^\dagger = \begin{pmatrix} \mu_{A1}z & -\left(x^\dagger\right)^2 z^2 \\ -x^2z^2 & \mu_{B2}z \end{pmatrix}. \tag{D.0.10}$$

The effective Hamiltonian H^{eff} is then

$$\begin{aligned} H^{\text{eff}} &= \begin{pmatrix} 1-|x|^2z^2/2 & 0 \\ 0 & 1-|x|^2z^2/2 \end{pmatrix} \begin{pmatrix} \mu_{A1}z & -\left(x^\dagger\right)^2 z^2 \\ -x^2z^2 & \mu_{B2}z \end{pmatrix} \begin{pmatrix} 1-|x|^2z^2/2 & 0 \\ 0 & 1-|x|^2z^2/2 \end{pmatrix} \\ &= \begin{pmatrix} \mu_{A1}z & -\left(x^\dagger\right)^2 z^2 \\ -x^2z^2 & \mu_{B2}z \end{pmatrix} \end{aligned} \tag{D.0.11}$$

We reverse the substitution and mutliply the effective Hamiltonian by γ_1 to get the final result

$$H^{\text{eff}} = \begin{pmatrix} \epsilon_{A1} & -v^2\left(\pi^\dagger\right)^2/\gamma_1 \\ -v^2\pi^2/\gamma_1 & \epsilon_{B2} \end{pmatrix}. \tag{D.0.12}$$

This effective Hamiltonian describes massive chiral electrons. It is similar to the monolayer graphene Hamiltonian (2.4.13), but with the off-diagonal monomentum terms being quadratic instead of linear.

Appendix E

$\mathbb{Z}_2$ Topological Index

The basic charge-density-wave model used in section 2.7 does not contain enough information to properly demonstrate the phases described by the $\mathbb{Z}_2$ topological index. In this appendix we will include next-nearest-neighbour hopping t' so that the vector $\boldsymbol{d}$ will better demonstrate the topological index. Start with the Hamiltonian in the basis of two neighbouring unit cells

$$H = \begin{pmatrix} \Delta & t & t' & 0 \\ t & -\Delta & t & -t' \\ t' & t & \Delta & t \\ 0 & -t' & t & -\Delta \end{pmatrix}, \tag{E.0.1}$$

where Δ is the onsite potential, t is the hopping parameter, and t' is the new next-nearest-neighbour hopping parameter. In order to preserve chiral symmetry the next-nearest-neighbour hopping is positive between sites on sublattice A and negative between sites on sublattice B. The Hamiltonian can then be written in the form $H = \boldsymbol{\sigma} \cdot \boldsymbol{d}(k)$, where the components of $\boldsymbol{d}(k)$ are

$$\begin{aligned} d_0(k) &= 0, \\ d_x(k) &= 2t\cos(ka/2), \\ d_y(k) &= 0, \\ d_z(k) &= \Delta + 2t'\cos(ka), \end{aligned} \tag{E.0.2}$$

where a is the lattice constant. Using the components of $\boldsymbol{d}(k)$ we can plot the eigenvalues and its trajectory in the $d_x d_z$ plane, which are shown in figure E.1. The eigenvalues are given by

$$E_{\pm}(k) = \pm\sqrt{d_x^2 + d_z^2} = \pm\sqrt{(2t\cos(ka/2))^2 + (\Delta + 2t'\cos(ka))^2}. \tag{E.0.3}$$

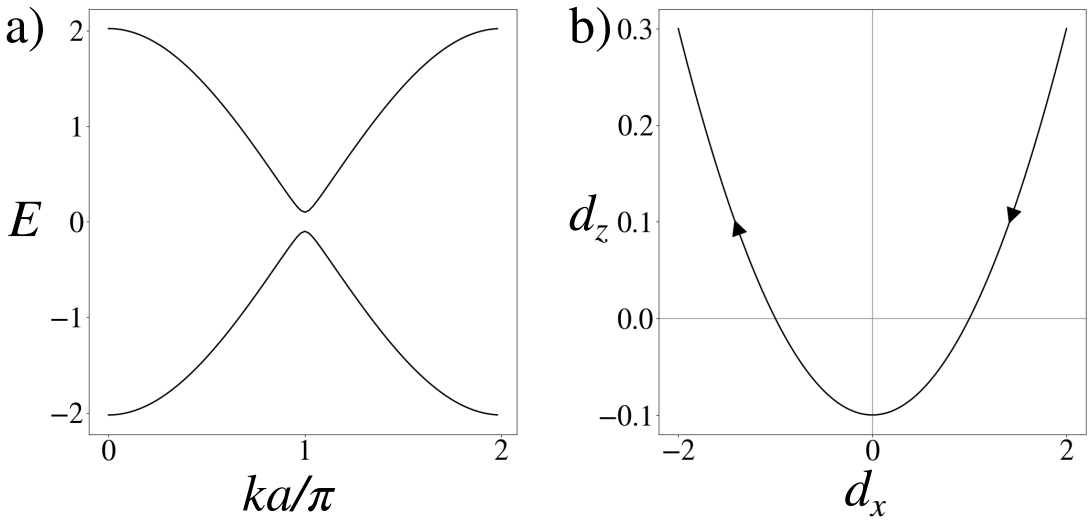

Figure E.1: a) Dispersion relation and b) trajectory of the CDW model with next-nearest-neighbour hopping. Arrows show the direction of the trajectory as k spans the first Brillouin zone $0 \leq k < 2\pi/a$. The parameters chosen are $t = 1$, $t' = 0.1$, $\Delta = 0.1$.

Figure E.1 shows that the trajectory of $\boldsymbol{d}(k)$ crosses the negative d_x axis once during its path, so the topological index for these parameters will be $\mu_2 = 1$.

Bibliography

[1] J. H. Muten, A. J. Copeland, and E. McCann. "Exchange interaction, disorder, and stacking faults in rhombohedral graphene multilayers". In: *Phys. Rev. B* 104 (3 July 2021), p. 035404.

[2] J. H. Muten, L. H. Frankland, and E. McCann. "Solitons in binary compounds with stacked two-dimensional honeycomb lattices". In: (2023). arXiv: 2312.16949 [cond-mat.mes-hall]. (accepted Phys. Rev. B).

[3] A. H. Castro Neto et al. "The electronic properties of graphene". In: *Rev. Mod. Phys.* 81 (1 Jan. 2009), pp. 109–162.

[4] K. S. Novoselov et al. "Electric Field Effect in Atomically Thin Carbon Films". In: *Science* 306.5696 (2004), pp. 666–669. eprint: https://www.science.org/doi/pdf/10.1126/science.1102896.

[5] P. R. Wallace. "The Band Theory of Graphite". In: *Phys. Rev.* 71 (9 May 1947), pp. 622–634.

[6] J. W. McClure. "Diamagnetism of Graphite". In: *Phys. Rev.* 104 (3 Nov. 1956), pp. 666–671.

[7] J. González, F. Guinea, and M. A. H. Vozmediano. "Continuum approximation to fullerene molecules". In: *Phys. Rev. Lett.* 69 (1 July 1992), pp. 172–175.

[8] H. Ajiki and T. Ando. "Electronic States of Carbon Nanotubes". In: *Journal of the Physical Society of Japan* 62.4 (1993), pp. 1255–1266. eprint: https://doi.org/10.1143/JPSJ.62.1255.

[9] M. S. Dresselhaus and G. Dresselhaus. "Intercalation compounds of graphite". In: *Advances in Physics* 51.1 (2002), pp. 1–186. eprint: https://doi.org/10.1080/00018730110113644.

[10] D. Perucci et al. “Evidence for Flat Bands near the Fermi Level in Epitaxial Rhombohedral Multilayer Graphene”. In: *ACS Nano* 9 (5 May 2015), pp. 5432–5439.

[11] Y. Henni et al. “Rhombohedral multilayer graphene: A magneto-Raman scattering study”. In: *Nano Lett.* 16.6 (2016), pp. 3710–3716.

[12] H. Henck et al. “Flat electronic bands in long sequences of rhombohedral-stacked graphene”. In: *Phys. Rev. B* 97.24 (2018), pp. 1–6.

[13] T. Latychevskaia et al. “Stacking transition in rhombohedral graphite”. In: *Frontiers of Physics* 14 (1 2018).

[14] Y. Yang et al. “Stacking Order in Graphite Films Controlled by van der Waals Technology”. In: *Nano Letters* 19.12 (Dec. 2019), pp. 8526–8532.

[15] F. R. Geisenhof et al. “Anisotropic Strain-Induced Soliton Movement Changes Stacking Order and Band Structure of Graphene Multilayers: Implications for Charge Transport”. In: *ACS Applied Nano Materials* 2.9 (2019), pp. 6067–6075. eprint: `https://doi.org/10.1021/acsanm.9b01603`.

[16] Y. Lee et al. “Gate Tunable Magnetism and Giant Magnetoresistance in ABC-stacked Few-Layer Graphene”. In: (2019). arXiv: `1911.04450 [cond-mat.mes-hall]`.

[17] C. Bouhafs et al. “Synthesis of large-area rhombohedral few-layer graphene by chemical vapor deposition on copper”. In: *Carbon* 177 (2021), pp. 282–290.

[18] A. Kerelsky et al. “Moiréless correlations in ABCA graphene”. In: *Proceedings of the National Academy of Sciences* 118.4 (2021), e2017366118. eprint: `https://www.pnas.org/doi/pdf/10.1073/pnas.2017366118`.

[19] Y. Shi et al. “Electronic phase separation in multilayer rhombohedral graphite”. In: *Nature* 584 (7820 Aug. 2020), pp. 210–214.

[20] C. Lee et al. “Measurement of the Elastic Properties and Intrinsic Strength of Monolayer Graphene”. In: *Science* 321.5887 (2008), pp. 385–388.

[21] C. Lee et al. “Measurement of the Elastic Properties and Intrinsic Strength of Monolayer Graphene”. In: *Science* 321.5887 (2008), pp. 385–388.

[22] K. I. Bolotin et al. “Temperature-Dependent Transport in Suspended Graphene”. In: *Phys. Rev. Lett.* 101 (9 Aug. 2008), p. 096802.

[23] X. Du et al. “Approaching ballistic transport in suspended graphene”. In: *Nature Nanotechnology* 3 (8 Aug. 2008), pp. 491–495.

[24] A. S. Mayorov et al. “Micrometer-Scale Ballistic Transport in Encapsulated Graphene at Room Temperature”. In: *Nano Letters* 11.6 (2011). PMID: 21574627, pp. 2396–2399. eprint: https://doi.org/10.1021/nl200758b.

[25] A. A. Balandin et al. “Superior Thermal Conductivity of Single-Layer Graphene”. In: *Nano Letters* 8.3 (2008). PMID: 18284217, pp. 902–907. eprint: https://doi.org/10.1021/nl0731872.

[26] A. E. Naclerio and P. R. Kidambi. “A Review of Scalable Hexagonal Boron Nitride (h-BN) Synthesis for Present and Future Applications”. In: *Advanced Materials* 35.6 (2023), p. 2207374. eprint: https://onlinelibrary.wiley.com/doi/pdf/10.1002/adma.202207374.

[27] G. Will, G. Nover, and J. von der Gönna. “New Experimental Results on the Phase Diagram of Boron Nitride”. In: *Journal of Solid State Chemistry* 154.1 (2000), pp. 280–285.

[28] Y Le Godec et al. “Compression and thermal expansion of rhombohedral boron nitride at high pressures and temperatures”. In: *Journal of Physics and Chemistry of Solids* 61.12 (2000), pp. 1935–1938.

[29] M. Chubarov et al. “Growth of High Quality Epitaxial Rhombohedral Boron Nitride”. In: *Crystal Growth & Design* 12.6 (2012), pp. 3215–3220. eprint: https://doi.org/10.1021/cg300364y.

[30] M. Moret et al. “Rhombohedral and turbostratic boron nitride: X-ray diffraction and photoluminescence signatures”. In: *Applied Physics Letters* 119.26 (Dec. 2021), p. 262102. eprint: https://pubs.aip.org/aip/apl/article-pdf/doi/10.1063/5.0076424/13885971/262102_1_online.pdf.

[31] W. Olovsson and M. Magnuson. “Rhombohedral and Turbostratic Boron Nitride Polytypes Investigated by X-ray Absorption Spectroscopy”. In: *The Journal of Physical Chemistry C* 126.49 (2022), pp. 21101–21108. eprint: https://doi.org/10.1021/acs.jpcc.2c06895.

[32] S.-f. Wang and X.-j. Wu. "First-Principles Study on Electronic and Optical Properties of Graphene-Like Boron Phosphide Sheets". In: *Chinese Journal of Chemical Physics* 28.5 (Oct. 2015), pp. 588–594. eprint: https://pubs.aip.org/cps/cjcp/article-pdf/28/5/588/14664724/588_1_online.pdf.

[33] Y. Wang et al. "Tight-binding model for electronic structure of hexagonal boron phosphide monolayer and bilayer". In: *Journal of Physics: Condensed Matter* 31.28 (Apr. 2019), p. 285501.

[34] O. Munive Hernández et al. "Hexagonal boron phosphide monolayer exfoliation induced by arsenic incorporation in the BP (111) surface: A DFT study". In: *Applied Surface Science* 538 (2021), p. 148163.

[35] S. S. Lin. "Light-Emitting Two-Dimensional Ultrathin Silicon Carbide". In: *The Journal of Physical Chemistry C* 116.6 (2012), pp. 3951–3955. eprint: https://doi.org/10.1021/jp210536m.

[36] P. Miró, M. Audiffred, and T. Heine. "An atlas of two-dimensional materials". In: *Chem. Soc. Rev.* 43 (18 2014), pp. 6537–6554.

[37] S. Chabi et al. "From graphene to silicon carbide: ultrathin silicon carbide flakes". In: *Nanotechnology* 27.7 (Jan. 2016), p. 075602.

[38] Z. Y. Al Balushi et al. "Two-dimensional gallium nitride realized via graphene encapsulation". In: *Nature Materials* 15.11 (), pp. 1166–1171.

[39] Z. Qin et al. "Orbitally driven low thermal conductivity of monolayer gallium nitride (GaN) with planar honeycomb structure: a comparative study". In: *Nanoscale* 9 (12 2017), pp. 4295–4309.

[40] H. Şahin et al. "Monolayer honeycomb structures of group-IV elements and III-V binary compounds: First-principles calculations". In: *Phys. Rev. B* 80 (15 Oct. 2009), p. 155453.

[41] H. L. Zhuang, A. K. Singh, and R. G. Hennig. "Computational discovery of single-layer III-V materials". In: *Phys. Rev. B* 87 (16 Apr. 2013), p. 165415.

[42] C. Tusche, H. L. Meyerheim, and J. Kirschner. "Observation of Depolarized ZnO(0001) Monolayers: Formation of Unreconstructed Planar Sheets". In: *Phys. Rev. Lett.* 99 (2 July 2007), p. 026102.

[43] M. Topsakal et al. “First-principles study of zinc oxide honeycomb structures”. In: *Phys. Rev. B* 80 (23 Dec. 2009), p. 235119.

[44] G. Weirum et al. “Growth and Surface Structure of Zinc Oxide Layers on a Pd(111) Surface”. In: *The Journal of Physical Chemistry C* 114.36 (2010), pp. 15432–15439. eprint: https://doi.org/10.1021/jp104620n.

[45] X. Deng et al. “Growth of Single- and Bilayer ZnO on Au(111) and Interaction with Copper”. In: *The Journal of Physical Chemistry C* 117.21 (2013), pp. 11211–11218. eprint: https://doi.org/10.1021/jp402008w.

[46] H. T. Quang et al. “In Situ Observations of Free-Standing Graphene-like Mono- and Bilayer ZnO Membranes”. In: *ACS Nano* 9.11 (2015). PMID: 26446371, pp. 11408–11413. eprint: https://doi.org/10.1021/acsnano.5b05481.

[47] K. F. Mak et al. “Atomically Thin MoS_2: A New Direct-Gap Semiconductor”. In: *Phys. Rev. Lett.* 105 (13 Sept. 2010), p. 136805.

[48] A. Splendiani et al. “Emerging Photoluminescence in Monolayer MoS2”. In: *Nano Letters* 10.4 (2010). PMID: 20229981, pp. 1271–1275. eprint: https://doi.org/10.1021/nl903868w.

[49] T. Korn et al. “Low-temperature photocarrier dynamics in monolayer MoS2”. In: *Applied Physics Letters* 99.10 (Sept. 2011), p. 102109. eprint: https://pubs.aip.org/aip/apl/article-pdf/doi/10.1063/1.3636402/13708934/102109_1_online.pdf.

[50] D. Xiao et al. “Coupled Spin and Valley Physics in Monolayers of MoS_2 and Other Group-VI Dichalcogenides”. In: *Phys. Rev. Lett.* 108 (19 May 2012), p. 196802.

[51] A. Kormányos et al. “k·p theory for two-dimensional transition metal dichalcogenide semiconductors”. In: *2D Materials* 2.2 (Apr. 2015), p. 022001.

[52] U. S. Shenoy et al. “Electronic structure and properties of layered gallium telluride”. In: *Chemical Physics Letters* 651 (2016), pp. 148–154.

[53] Y. Yu et al. “Phase-Engineered Synthesis of Ultrathin Hexagonal and Monoclinic GaTe Flakes and Phase Transition Study”. In: *Advanced Functional Materials* 29.23 (2019), p. 1901012. eprint: https://onlinelibrary.wiley.com/doi/pdf/10.1002/adfm.201901012.

[54] M. Liu et al. “Controlled Growth of Large-Sized and Phase-Selectivity 2D GaTe Crystals”. In: *Small* 17.21 (2021), p. 2007909. eprint: https://onlinelibrary.wiley.com/doi/pdf/10.1002/smll.202007909.

[55] J. Palepu et al. “Effects of artificial stacking configurations and biaxial strain on the structural, electronic and transport properties of bilayer GaSe- A first principle study”. In: *Materials Science in Semiconductor Processing* 137 (2022), p. 106236.

[56] K. Lai and J. Dai. “Stacking effect on the electronic structures of hexagonal GaTe”. In: *Journal of Physics D: Applied Physics* 56.27 (Apr. 2023), p. 275301.

[57] N. Ashcroft and N. Mermin. *Solid State Physics*. Belmont: Brooks/Cole, 1976.

[58] R Saito, G Dresselhaus, and M. S. Dresselhaus. *Physical Properties of Carbon Nanotubes*. Imperial College Press, 1998. eprint: https://www.worldscientific.com/doi/pdf/10.1142/p080.

[59] E McCann. *Graphene Nanoelectronics: Metrology, Synthesis, Properties and Applications*. Ed. by H Raza. Berlin: Springer, pp. 237–75.

[60] A. B. Kuzmenko et al. “Determination of the gate-tunable band gap and tight-binding parameters in bilayer graphene using infrared spectroscopy”. In: *Phys. Rev. B* 80 (16 Oct. 2009), p. 165406.

[61] J. W. McClure. “Band Structure of Graphite and de Haas-van Alphen Effect”. In: *Phys. Rev.* 108 (3 Nov. 1957), pp. 612–618.

[62] J. C. Slonczewski and P. R. Weiss. “Band Structure of Graphite”. In: *Phys. Rev.* 109 (2 Jan. 1958), pp. 272–279.

[63] J. W. McClure. “Theory of Diamagnetism of Graphite”. In: *Phys. Rev.* 119 (2 July 1960), pp. 606–613.

[64] I. Snyman and C. W. J. Beenakker. “Ballistic transmission through a graphene bilayer”. In: *Phys. Rev. B* 75 (4 Jan. 2007), p. 045322.

[65] E. McCann and M. Koshino. “The electronic properties of bilayer graphene”. In: *Reports on Progress in Physics* 76 (Apr. 2013), p. 056503.

[66] W. P. Su, J. R. Schrieffer, and A. J. Heeger. “Solitons in Polyacetylene”. In: *Phys. Rev. Lett.* 42 (25 June 1979), pp. 1698–1701.

[67] J. K. Asbóth, L. Oroszlány, and A. Pályi. “A Short Course on Topological Insulators: Band-structure topology and edge states in one and two dimensions”. In: (2015). arXiv: 1509.02295.

[68] J Cayssol and J. N. Fuchs. “Topological and geometrical aspects of band theory”. In: *Journal of Physics: Materials* 4.3 (Apr. 2021), p. 034007.

[69] E. McCann. “Catalog of noninteracting tight-binding models with two energy bands in one dimension”. In: *Physical Review B* 107.24 (June 2023).

[70] R. E. Peierls. *Quantum Theory of Solids*. Oxford University Press, 1955.

[71] S. Ryu et al. “Topological insulators and superconductors: tenfold way and dimensional hierarchy”. In: *New Journal of Physics* 12.6 (June 2010), p. 065010.

[72] R. E. J. Allen et al. “Nonsymmorphic chiral symmetry and solitons in the Rice-Mele model”. In: *Phys. Rev. B* 106 (16 Oct. 2022), p. 165409.

[73] R. Jackiw and C. Rebbi. “Solitons with fermion number $\frac{1}{2}$”. In: *Phys. Rev. D* 13 (12 June 1976), pp. 3398–3409.

[74] L. Li, Z. Xu, and S. Chen. “Topological phases of generalized Su-Schrieffer-Heeger models”. In: *Phys. Rev. B* 89 (8 Feb. 2014), p. 085111.

[75] I. Mondragon-Shem et al. “Topological Criticality in the Chiral-Symmetric AIII Class at Strong Disorder”. In: *Phys. Rev. Lett.* 113 (4 July 2014), p. 046802.

[76] B. Pérez-González et al. “Interplay between long-range hopping and disorder in topological systems”. In: *Phys. Rev. B* 99 (3 Jan. 2019), p. 035146.

[77] M. Scollon and M. P. Kennett. “Persistence of chirality in the Su-Schrieffer-Heeger model in the presence of on-site disorder”. In: *Phys. Rev. B* 101 (14 Apr. 2020), p. 144204.

[78] F. Munoz et al. “Topological properties of a bipartite lattice of domain wall states”. In: *Scientific Reports* 8 (1 Nov. 2018), p. 17330.

[79] K. Shiozaki, M. Sato, and K. Gomi. "Z_2 topology in nonsymmorphic crystalline insulators: Möbius twist in surface states". In: *Phys. Rev. B* 91 (15 Apr. 2015), p. 155120.

[80] M. J. Rice and E. J. Mele. "Elementary Excitations of a Linearly Conjugated Diatomic Polymer". In: *Phys. Rev. Lett.* 49 (19 Nov. 1982), pp. 1455–1459.

[81] T. T. Heikkilä and G. E. Volovik. "Dimensional crossover in topological matter: Evolution of the multiple Dirac point in the layered system to the flat band on the surface". In: *JETP Letters* 93.2 (Mar. 2011), pp. 59–65.

[82] R. Xiao et al. "Density functional investigation of rhombohedral stacks of graphene: Topological surface states, nonlinear dielectric response, and bulk limit". In: *Phys. Rev. B* 84 (16 Oct. 2011), p. 165404.

[83] M. Taut, K. Koepernik, and M. Richter. "Electronic structure of stacking faults in rhombohedral graphite". In: *Phys. Rev. B* 90 (8 Aug. 2014), p. 085312.

[84] S. Slizovskiy et al. "Films of rhombohedral graphite as two-dimensional topological semimetals". In: *Communications Physics* 2.1 (Dec. 2019), p. 164.

[85] A. García-Ruiz et al. "Spectroscopic Signatures of Electronic Excitations in Raman Scattering in Thin Films of Rhombohedral Graphite". In: *Nano Letters* 19.9 (2019). PMID: 31361497, pp. 6152–6156. eprint: `https://doi.org/10.1021/acs.nanolett.9b02196`.

[86] Y Le Godec et al. "Compression and thermal expansion of rhombohedral boron nitride at high pressures and temperatures". In: *Journal of Physics and Chemistry of Solids* 61.12 (2000), pp. 1935–1938.